# Aspects of Stepped-Frequency Processing
# for Low-Frequency SAR Systems

*by*

**Richard Thomas Lord**

BSc (Eng) UCT (1994)

A thesis submitted to the Department of Electrical Engineering,
University of Cape Town, in fulfilment of the requirements
for the degree of

**Doctor of Philosophy**

*at the*

**UNIVERSITY OF CAPE TOWN**

February 2000

# Declaration

I declare that this thesis is my own, unaided work. It is being submitted for the degree of Doctor of Philosophy in the University of Cape Town. It has not been submitted before for any degree or examination in any other university.

Signature of Author . . . . . . . . . . . . . . . . . . . . . . . . . . . . . . . . . . . . . . . . . . . . . . . . . . . . . . . . . . . . . .

Department of Electrical Engineering
Cape Town, February 2000

# Abstract

Ultra-wideband synthetic aperture radar (SAR) systems operating in the VHF/UHF region are becoming increasingly popular because of their growing number of applications in the areas of foliage penetration radar (FOPEN) and ground-penetrating radar (GPR). The objective of this thesis is to investigate the following two aspects of low-frequency (VHF/UHF-band) SAR processing:

1. The use of stepped-frequency waveforms to increase the total radar bandwidth, thereby increasing the range resolution, and

2. Radio frequency interference (RFI) suppression.

A stepped-frequency system owes its wide bandwidth to the transmission of a group of narrow-bandwidth pulses, which are then combined using a signal processing technique to achieve the wide bandwidth. Apart from providing an economically viable path for the upgrading of an existing single frequency system, stepped-frequency waveforms also offer opportunities for RFI suppression.

This thesis describes three methods to process stepped-frequency waveforms, namely an IFFT method, a time-domain method and a frequency-domain method. Both the IFFT method and the time-domain method have been found to be unsuitable for SAR processing applications. The IFFT method produces multiple "ghost targets" in the high resolution range profile due to the spill-over effect of energy into consecutive coarse range bins, and the time-domain technique is computationally inefficient on account of the upsampling requirement of the narrow-bandwidth pulses prior to the frequency shift. The frequency-domain technique, however, efficiently uses all the information in the narrowband pulses to obtain high-resolution range profiles which do not contain any "ghost targets", and is therefore well suited for SAR processing applications. This technique involves the reconstruction of a wider portion of the target's reflectivity spectrum

by combining the individual spectra of the transmitted narrow-bandwidth pulses in the frequency domain. It is shown here how this method may be used to avoid spectral regions that are heavily contaminated with RFI, thereby alleviating the problem of receiver saturation due to RFI. Stepped-frequency waveforms also enable the A/D converter to sample the received narrow-bandwidth waveform with a larger number of bits, which increases the receiver dynamic range, thereby further alleviating the problem of receiver saturation during the presence of RFI.

In addition to using stepped-frequency waveforms for RFI suppression, a number of other techniques have been investigated to suppress RFI. Of these, the notch filter and the LMS adaptive filter have been implemented and applied on real P-band data obtained from the E-SAR system of the German Aerospace Center (DLR), Oberpfaffenhofen, and on real VHF-band data obtained from the South African SAR (SASAR) system. Both methods significantly suppressed the RFI in the real images investigated.

It was found that the number of range lines upon which the LMS adaptive filter could operate without adaptively changing the filter tap weights was often well above 100. This facilitated the re-writing of the LMS adaptive filter in terms of an equivalent transfer function, which was then integrated with the range-compression stage of the range-Doppler SAR processing algorithm. Since the range-compression and the interference suppression could then be performed simultaneously, large computational savings were achieved.

A technique was derived for suppressing the sidelobes which arise as a result of the interference suppression of the LMS adaptive filter. This method was also integrated with the range-compression stage of the range-Doppler processor, leading to a very efficient implementation of the entire RFI suppression routine.

# Acknowledgements

# Contents

# List of Figures

# List of Tables

# List of Symbols

| | | |
|---|---|---|
| $A$ | — | Amplitude [m] |
| $B$ | — | Bandwidth [Hz] |
| $B_d$ | — | Doppler bandwidth [Hz] |
| $B_t$ | — | Total radar bandwidth [Hz] |
| $B_{tx}$ | — | Transmitted RF bandwidth [Hz] |
| $c$ | — | Speed of light [m/s] |
| $d$ | — | Primary input of LMS adaptive filter |
| $\mathbf{D}$ | — | Input signal vector |
| $e$ | — | Error signal of LMS adaptive filter |
| $f$ | — | Frequency [Hz] |
| $f_{ad}$ | — | Radar A/D sampling frequency [Hz] |
| $f_c$ | — | Radar centre transmit frequency [Hz] |
| $f_c'$ | — | Centre frequency of reconstructed spectrum [Hz] |
| $f_i$ | — | Centre frequency of pulse $i$ [Hz] |
| $\delta f_i$ | — | Frequency shift associated with pulse $i$ [Hz] |
| $f_{\mathrm{prf}}$ | — | Pulse repetition frequency [Hz] |
| $\Delta f$ | — | Frequency step size [Hz] |
| $H(f)$ | — | Compression filter |
| $H(\omega)$ | — | Equivalent transfer function of LMS adaptive filter |
| $K_a$ | — | Azimuth window broadening constant |
| $K_r$ | — | Range window broadening constant |
| $l$ | — | Real antenna length [m] |
| $L$ | — | Synthetic aperture length [m] |
| $m_i$ | — | Number of range samples associated with pulse $i$ |
| $M(\omega)$ | — | Matched filter |
| $n$ | — | Number of pulses in a burst of pulses |
| $n(t)$ | — | Noise signal |

| | | |
|---|---|---|
| $N$ | — | Number of filter weights |
| $P_{\text{av}}$ | — | Average transmitted power [W] |
| $P_{\text{peak}}$ | — | Peak transmitted power [W] |
| $r$ | — | Range [m] |
| $r_{\text{coarse}}$ | — | Coarse slant range resolution [m] |
| $r_{\text{max}}$ | — | Maximum unambiguous range [m] |
| $r_t$ | — | Range from radar to target [m] |
| $t$ | — | Time [s] |
| $\delta t_i$ | — | Time shift associated with pulse $i$ [s] |
| $T$ | — | Interpulse period [s] |
| $T_p$ | — | Pulse length [s] |
| $v$ | — | Ground speed [m/s] |
| $v(t)$ | — | Range-compressed signal |
| $v'(t)$ | — | High-resolution, range-compressed signal |
| $v_{bb}(t)$ | — | Baseband signal |
| $v_{rx}(t)$ | — | Received waveform |
| $v_{tx}(t)$ | — | Transmitted waveform |
| $v_t$ | — | Radial target velocity [m/s] |
| $w_s$ | — | Synthesised unambiguous range length [m] |
| $\mathbf{W}$ | — | Weight vector of LMS adaptive filter |
| $x$ | — | Reference input of LMS adaptive filter |
| $\mathbf{X}$ | — | Reference signal vector |
| $y$ | — | Output of LMS adaptive filter |
| $Z(f)$ | — | Target reflectivity spectrum |
| $\gamma$ | — | Chirp rate of linear FM waveform [Hz/s] |
| $\Delta$ | — | Delay associated with LMS adaptive filter [s] |
| $\zeta(t)$ | — | Target reflectivity function |
| $\eta$ | — | Quality index |
| $\theta_s$ | — | Squint angle [rad] |
| $\lambda$ | — | Wavelength [m] |
| $\lambda_{\text{max}}$ | — | Largest eigenvalue of input correlation matrix |
| $\mu$ | — | Convergence factor |
| $\rho_a$ | — | Azimuth resolution [m] |
| $\Delta\rho_a$ | — | Azimuth bin size [m] |
| $\rho_r$ | — | Slant range resolution [m] |
| $\Delta\rho_r$ | — | Slant range bin size [m] |

$\phi_i$ &mdash; Phase of pulse $i$ [rad]

$\Delta\phi$ &mdash; Phase difference [rad]

$\omega$ &mdash; Angular frequency [rad/s]

# Nomenclature

**A/D**—Analogue to Digital.

**ARPA**—Advanced Research Projects Agency (USA).

**Azimuth**—Angle in a horizontal plane, relative to a fixed reference, generally North or the longitudinal reference axis of an aircraft or satellite.

**Beamwidth**—The angular width of a slice through the mainlobe of the radiation pattern of an antenna in the horizontal, vertical or other plane.

**Burst**—Set of all frequencies required to produce a synthetic range profile.

**CARABAS**—Coherent All Radio Band Sensing (Swedish SAR).

**Chirp**—A pulse modulation method used for pulse compression, also called *linear frequency modulation*. The frequency of each pulse is increased or decreased at a constant rate throughout the length of the pulse.

**Coherence**—A continuity or consistency in the phases of successive radar pulses.

**Corner reflector**—A radar reflector that reflects nearly all of the radio frequency energy it intercepts back in the direction of the radar which is illuminating it.

**CSIR**—Council for Scientific and Industrial Research (South Africa).

**DC3**—Dakota aircraft (C47).

**Dilute**—If individual scatterers on a target can be resolved, the target features are said to be *dilute*.

**DLR**—Deutsches Zentrum für Luft- und Raumfahrt (German Aerospace Center).

**Doppler frequency**—A shift in the radio frequency of the return from a target or other object as a result of the object's radial motion relative to the radar.

**DPT**—Department of Posts and Telecommunications (South Africa).

**Encounter**—Set of all profiles obtained while a target is in sight, acquired over a number of scans.

**ERIM**—Environmental Research Institute of Michigan (USA).

**ESA**—European Space Agency.

**E-SAR**—Experimental SAR (DLR, Germany).

**E-to-S**—Earth-to-Space.

**FFT**—Fast Fourier Transform.

**FIR**—Finite Impulse Response.

**FM**—Frequency Modulation.

**FOA**—Försvarets Forskningsanstalt (Swedish Defence Research Establishment).

**FOPEN**—Foliage Penetration.

**G2**—Ground Processor Version 2 (UCT RRSG).

**GPR**—Ground-Penetrating Radar.

**IDL**—Interactive Data Language.

**IFFT**—Inverse Fast Fourier Transform.

**IRW**—Impulse Response Width.

**ISL**—Integrated Sidelobe Level.

**Isotropic**—Non-directional.

**JPL**—Jet Propulsion Laboratory (USA).

**L-band**—Nominal frequency range 1000–2000 MHz.

**LMS**—Least Mean Squared.

**MTI**—Moving Target Indication.

**Nadir**—The point directly below the radar platform.

**Narrowband**—Describes radar systems that transmit and receive waveforms with instantaneous bandwidths less than 1 percent of centre frequency (Taylor 1995).

**NAWC**—Naval Air Warfare Centre (USA).

**NCTR**—Non-Co-operative Target Recognition.

**PCR**—Pulse Compression Ratio.

**PRF**—Pulse Repetition Frequency.

**PRI**—Pulse Repetition Interval.

**Profile**—Contour of the target outline which is deduced from reflected signals in a radar system.

**PSL**—Peak Sidelobe Level.

**Radar**—Radio Detection and Ranging.

**Range**—The radial distance from a radar to a target.

**RFI**—Radio Frequency Interference.

**RRSG**—Radar Remote Sensing Group (UCT).

**SAAF**—South African Air Force.

**SAR**—Synthetic Aperture Radar. A signal-processing technique for improving the azimuth resolution beyond the beamwidth of the physical antenna actually used in the radar system. This is done by synthesising the equivalent of a very long sidelooking array antenna.

**SASAR**—South African Synthetic Aperture Radar.

**Scan**—Set of pulses received during illumination time.

**SLC**—Single Look Complex.

**SNR**—Signal to Noise Ratio.

**Specular**—Highly directional. The power returned from a specular reflector depends very much on the direction of illumination.

**SRP**—Synthetic Range Profile.

**STC**—Sensitivity Time Control.

**S-to-E**—Space-to-Earth.

**Swath**—The area on earth illuminated by the antenna signal.

**UCT**—University of Cape Town (South Africa).

**UHF**—Ultra High Frequency. Nominal frequency range 300–3000 MHz.

**UWB**—Ultra-Wideband. Describes radar systems that transmit and receive waveforms with instantaneous bandwidths greater than 25 percent of centre frequency (Taylor 1995).

**VHF**—Very High Frequency. Nominal frequency range 30–300 MHz.

**Wideband**—Describes radar systems that transmit and receive waveforms with instantaneous bandwidths between 1 percent and 25 percent of centre frequency (Taylor 1995).

# Chapter 1

# Introduction

## 1.1 Background

*Synthetic Aperture Radar* (SAR) is a technique for creating high resolution images of the earth's surface. Over the area of the surface being observed, these images represent the backscattered microwave energy, which depends on the properties of the surface, such as its slope, roughness, textural inhomogeneities and dielectric constant. The radar backscattering cross section also depends strongly on the existence of vegetation. These dependencies allow SAR imagery to be used in conjunction with models of the scattering mechanism to measure various characteristics of the earth's surface, such as topography.

An important characteristic of SAR is its day/night capability, which it possesses because it supplies its own illumination and receives the backscatter from it, as opposed to passive sensors which receive either the earth's radiation or the reflected illumination from the sun. Furthermore, a SAR sensor has all-weather capability, because microwaves propagate through clouds and rain with only limited attenuation. These features, together with its fine two-dimensional resolution capability, have made SAR a valuable remote sensing tool for both military and civilian users. Military SAR applications include intelligence gathering, battlefield reconnaissance and weapons guidance. Civilian applications include topographic mapping, geology and mining (Lynne and Taylor 1986), oil spill monitoring (Hovland, Johannessen and Digranes 1994), sea ice monitoring (Drinkwater, Kwok and Rignot 1990), oceanography (Wahl and Skoelv 1994), agricultural classification and assessment, land use monitoring and planetary or celestial investigations (Carrara, Goodman and Majewski 1995a).

## 1.2  Low-Frequency SAR

Increased interest has developed in ultra-wideband VHF/UHF SAR because of its applications in the areas of *foliage penetration* radar (FOPEN) and *ground-penetrating radar* (GPR) (Elachi, Roth and Schaber 1984), (Berlin, Tarabzouni, Al-Naser, Sheikho and Larson 1986), (Schaber, McCauley, Breed and Olhoeft 1986). Such applications include the detection of targets concealed by foliage and/or camouflage (Gustavsson, Flood, Frölind, Hellsten, Jonsson, Larsson, Stenström and Ulander 1998a), (Gustavsson, Ulander, Flood, Frölind, Hellsten, Jonsson, Larsson and Stenström 1998b), the detection of buried objects, the detection and location of buried pipes and cables, and archaeological and geological exploration, such as the location of underground riverbeds (Schaber, Olhoeft and McCauley 1990). The term *ultra-wideband* (UWB) describes radar systems that transmit and receive waveforms with instantaneous bandwidths greater than 25 percent of centre frequency (Taylor 1995). Conventional *narrowband* radar systems generally have fractional bandwidths less than 1 % of centre frequency, and *wideband* radar systems generally have fractional bandwidths from 1 % to 25 % of centre frequency.

Airborne SAR sensors which operate below L-band (1000–2000 MHz) include:

- The CARABAS-II ultra-wideband VHF SAR system of the Swedish Defence Research Establishment (FOA), which operates in the 20–90 MHz region (Larsson, Frölind, Gustavsson, Hellsten, Jonsson, Stenström and Ulander 1997), (Ulander and Frölind 1999).

- The P-band (450 MHz) sensor of the German DLR E-SAR (Buckreuss 1998).

- The NASA/JPL AIRSAR P-band system (http://airsar.jpl.nasa.gov/).

- The NASA/JPL dual-frequency airborne GeoSAR system, which operates at both P- and X-band (http://lightsar.jpl.nasa.gov/html/projects/geosar/geosar.html).

- The ARPA/ERIM/NAWC P-3 ultra-wideband SAR, which operates in the 215–900 MHz region (Carrara, Tummala and Goodman 1995b).

- The Russian iMARK VHF SAR sensor, which has a centre frequency of 120 MHz and is operated by the Moscow Scientific Research Institute of

Instrument Engineering and the All-Union Scientific Research Institute of Cosmoaerological Methods.

- The *South African SAR* (SASAR) VHF sensor which operates with a 12 MHz bandwidth centred around 141 MHz (Inggs 1996).

The initial design and conception of the SASAR system originated at the *University of Cape Town* (UCT) (Inggs 1996). Originally it was planned to be a fully polarimetric, multifrequency SAR system; however, due to budget constraints, only a single VHF sensor has currently been constructed. The system platform was originally intended to be a Boeing 707 aircraft, offered by the South African Air Force. However, since the Boeing proved to have limited availability, the system is now installed in a South African Airforce DC3/C47 aircraft. The motivation behind using a VHF sensor is the hope that it will offer unique opportunities for foliage and ground penetration.

The 12 MHz bandwidth of the SASAR system corresponds to a slant range resolution of about 12 m. It is still hoped to increase the resolution to about 1.5 m, which would require a total bandwidth of 100 MHz. For SAR systems operating in the VHF/UHF-band, this bandwidth would be a large fraction of the transmit centre frequency and would be more difficult to obtain than for systems operating at C- or X-band. The most difficult problem when implementing a large fractional bandwidth system is the design of a broad-band antenna. However, one possible method of achieving this bandwidth would be to use stepped-frequency waveforms.

## 1.3 Motivation for Using Stepped-Frequency Waveforms

### 1.3.1 Achieving higher total bandwidth

The total radar bandwidth of a stepped-frequency system is synthetically obtained by combining a burst of narrow-bandwidth returns through the application of a signal processing method. Stepped-frequency processing therefore offers the possibility of economically upgrading an existing single frequency SAR system to improve its bandwidth and therefore its range resolution, since only

minimal modifications to the existing radar system are required. Although this thesis is only concerned with the signal processing aspect of a stepped-frequency system and not with the system level design of such a system, the following two main steps for such an upgrade are noted:

1. The design of a broader band antenna, which is capable of transmitting and receiving the entire required frequency range. If the bandwidth increase is not too large, the existing antenna might even be sufficient in some cases.

2. The employment of a frequency synthesizer, which steps through the entire frequency range. It would not be necessary to modify the existing chirp waveform generator.

Since the instantaneous bandwidth received at the radar is only a fraction of the total synthesised bandwidth, there is also no need to upgrade the existing A/D converters. It is also easier to switch between modes of different resolutions, without paying the penalty of receiving increased amounts of *radio frequency interference* (RFI) due to having a wide-bandwidth receiver. These aspects make the design of a stepped-frequency SAR system economically attractive and viable.

## 1.3.2   Higher receiver dynamic range

Another advantage of having A/D converters which need only sample at a lower rate because of the lower instantaneous bandwidth is the ability to sample with a larger number of bits, because there is a trade-off between sampling frequency and number of sampling bits. Sampling with a larger number of bits increases the receiver dynamic range, which is an important consideration for low-frequency SAR, since the RFI encountered in the VHF/UHF-band (such as FM-radio or TV) is often many tens of dB stronger than the signal. Increasing the receiver dynamic range reduces the possibility of receiver saturation. Receiver saturation causes clipping of the received signal and signal suppression, which degrades the image quality and leads to the formation of higher harmonics, making the task of interference suppression algorithms more demanding. According to Ulander (Ulander 1998), the receiver dynamic range required for wide-beam and ultra-wideband SAR in the VHF-band (such as the CARABAS-II SAR system) is typically of the order of 80 dB. However, this dynamic range can be achieved

only by sacrificing bandwidth. State-of-the-art receiver technology can typically only achieve a bandwidth of about 10 MHz or less with a spurious-free dynamic range of 80 dB (Ulander 1998). Stepped-frequency SAR processing therefore offers a way to design wideband SAR systems which also have the required high receiver dynamic range at VHF/UHF frequencies.

### 1.3.3 Radio frequency interference suppression

Unfortunately, from the point of view of SAR implementations, the VHF/UHF portion of the spectrum is already in heavy use by other services, such as television, mobile communications, radio and cellular phones. Even in remote locations the interference power often exceeds receiver noise by many dB, becoming the limiting factor on system sensitivity and severely degrading the image quality. Therefore it is important to investigate possible means of suppressing the interference in the received signal.

When the bandwidth of an existing SAR system is increased, the situation degenerates further, since the radar becomes susceptible to receiver saturation over that whole band. Given the large number of narrowband interfering sources, interference vectors may sporadically combine constructively, increasing the instantaneous magnitude of the interference, and thereby increasing the likelihood of receiver saturation even more.

In order to alleviate the problem of receiver saturation, it is proposed in this thesis to use stepped-frequency waveforms to avoid regions in the frequency spectrum that contain the dominant interfering sources. This can be achieved by simply omitting the relevant frequency steps when sweeping through the frequency range. These frequency "holes" will, however, raise the sidelobes. A more sophisticated method would be to change adaptively the frequency step size, or even the transmit bandwidth, in order to notch out as little spectrum as possible. Ideally the transmitter should be switched off occasionally, in order to receive only interference or so-called "sniffer" pulses. This data could then be used to decide which regions in the spectrum should be avoided because of strong interference. Alternatively, a study of the local interference environment could be carried out in order to decide in advance which spectral regions to avoid. A more detailed description of the interference environment encountered in South Africa is given in Section 1.4.

## 1.4 RFI Suppression

### 1.4.1 Radio frequency allocation in South Africa

The information presented in this section has been obtained from a document produced by the *Department of Posts and Telecommunications* (DPT) in South Africa in 1996, with the assistance of Smith System Engineering and the CSIR, as part of Project SABRE (*South African Band Re-planning Exercise*) (DPT 1996). This document details the frequency allocation plan for the future use of the radio spectrum in South Africa between the frequencies 20 MHz and 3 GHz. The VHF/UHF spectrum in South Africa is already utilised by a wide range of systems and services, such as:

- Telephone services to rural areas and disadvantaged communities;

- Television and radio broadcasts;

- Mobile radio systems used by commercial organisations;

- Emergency communications by the police, fire and ambulance services, etc.;

- Cellular, cordless telephones and pagers;

- Satellites (for telecommunication and broadcasting);

- Alarm systems, remote control devices, etc.

Table 1.1 presents the radio spectrum allocation plan in South Africa between 30 MHz and 960 MHz. Only the main allocations are summarised, in order to present an overview of the spectrum allocation. More detailed information can be obtained from the SABRE document (DPT 1996).

### 1.4.2 RFI measured in Cape Town

In order to assess the amount of RFI that could be expected by the SASAR system in Cape Town, a simple quarter wavelength antenna was attached to a spectrum analyser with a bandwidth resolution of 10 kHz. The output of the spectrum analyser from 80–200 MHz is shown in Figure 1.1 (a). Clearly visible is

| Frequency Band (MHz) | Main Allocations |
| :---: | :--- |
| 30.01–74.8 | Mobile / Fixed / Amateur |
| 74.8–75.2 | Aeronautical Radionavigation |
| 75.2–87.5 | Mobile / Fixed |
| 87.5–108 | FM Sound Broadcasting |
| 108–137 | Aeronautical Radionavigation / Aeronautical Mobile |
| 137–138 | Mobile-Satellite / Meteorological-Satellite / Mobile / Space Operation / Space Research |
| 138–144 | Mobile / Fixed |
| 144–146 | Amateur / Amateur-Satellite |
| 146–148 | Mobile / Fixed |
| 148–149.9 | Mobile-Satellite (E-to-S) / Mobile / Fixed |
| 149.9–150.05 | Radionavigation-Satellite / Land Mobile-Satellite |
| 150.05–174 | Mobile / Fixed / Maritime Mobile |
| 174–238 | Band III TV Broadcast Channels 4 to 11 |
| 238–246 | Mobile / Fixed |
| 246–254 | Band III TV Broadcast Channel 13 |
| 254–328.6 | Mobile / Fixed |
| 328.6–335.4 | Aeronautical Radionavigation |
| 335.4–399.9 | Mobile / Fixed |
| 399.9–400.05 | Radionavigation-Satellite / Land Mobile-Satellite |
| 400.05–400.15 | Standard Frequency and Time Signal |
| 400.15–401 | Mobile-Satellite / Meteorological-Satellite / Meteorological Aids / Space Research |
| 401–406 | Meteorological Aids / Space Operation (S-to-E) |
| 406–406.1 | Mobile-Satellite (E-to-S) |
| 406.1–430 | Mobile / Fixed |
| 430–440 | Amateur / Radiolocation |
| 440–470 | Mobile / Fixed |
| 470–854 | TV Broadcasting Channels 21–68 |
| 854–862 | Fixed |
| 862–960 | Mobile / Fixed |

**Table 1.1:** *Radio spectrum allocation plan in South Africa: 30–960 MHz.*
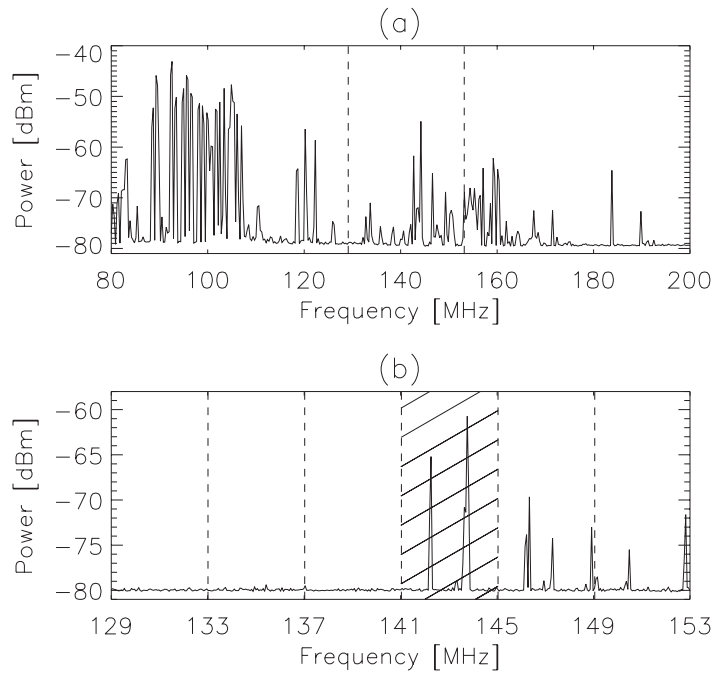
**Figure 1.1:** *Radio frequency interference measured in Cape Town: (a) 80–200 MHz; (b) 129–153 MHz.*
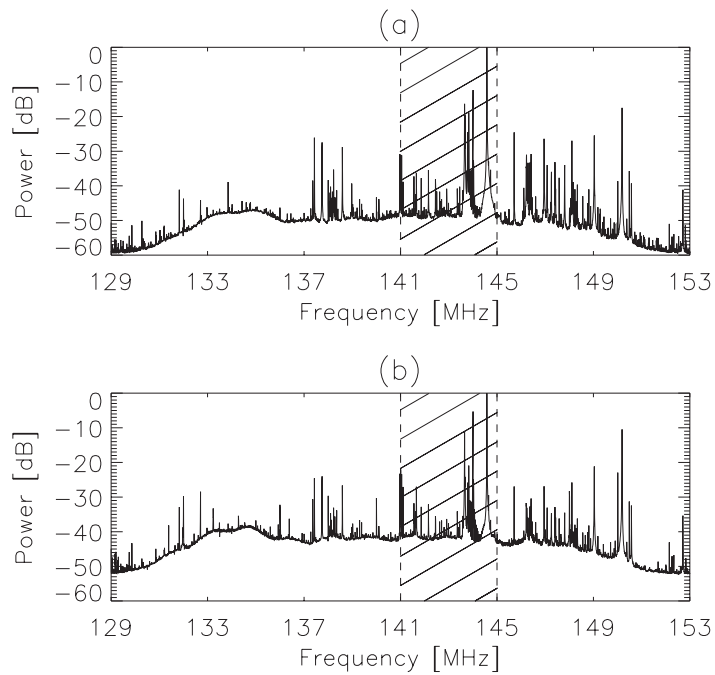


**Figure 1.2:** *Radio frequency interference measured with the SASAR system near the Southern Cape, South Africa: (a) H receive polarisation; (b) V receive polarisation.*

the FM sound broadcasting region from 87.5–108 MHz. There is also significant RFI just above 141 MHz, which is the centre frequency of the SASAR system. Figure 1.1 (b) shows the output of the spectrum analyser from 129–153 MHz, which represents a bandwidth of 24 MHz centred around 141 MHz. The vertical dashed lines divide this region into 6 hypothetical "frequency steps". The 4th frequency step (indicated by diagonal lines) contains the dominant interfering sources, which are nearly 10 dB stronger than those in the 5th frequency step. One could therefore alleviate the problem of insufficient receiver dynamic range by skipping the 4th frequency step.

### 1.4.3   RFI measured with the SASAR system

During a recent flight over the Southern Cape area in South Africa, the blanking switch of the SASAR system was deliberately switched on, so that no pulses were transmitted. This permitted the background interference to be recorded. Since the sampling rate of the SASAR system is 24 MHz, the recorded spectrum ranges from 129 MHz to 153 MHz, centred around 141 MHz.

Figure 1.2 shows the magnitude averaged range spectrum of 1000 range lines for both the H and V receive polarisation. The dominant interference for V receive polarisation is about 5 dB less than for H receive polarisation. Although the interference pattern is not quite the same as that shown in Figure 1.1 (b), the dominant interference is again situated in the 4th frequency step (as indicated by the diagonal lines). There is, however, still a lot of interference in the remaining spectrum. Other RFI suppression methods must be employed in order to suppress the remaining interference that could not be notched out.

### 1.4.4   Other RFI suppression methods

Since RFI covers virtually the whole VHF/UHF spectrum, the technique of omitting frequency steps to notch out interference can only be applied to a few very dominant interfering sources. The remaining interference has to be suppressed using other techniques. This is the subject of Chapter 4. More specifically, the notch filter and the *least mean squared* (LMS) adaptive filter are described and implemented on real noisy SASAR data to suppress RFI.
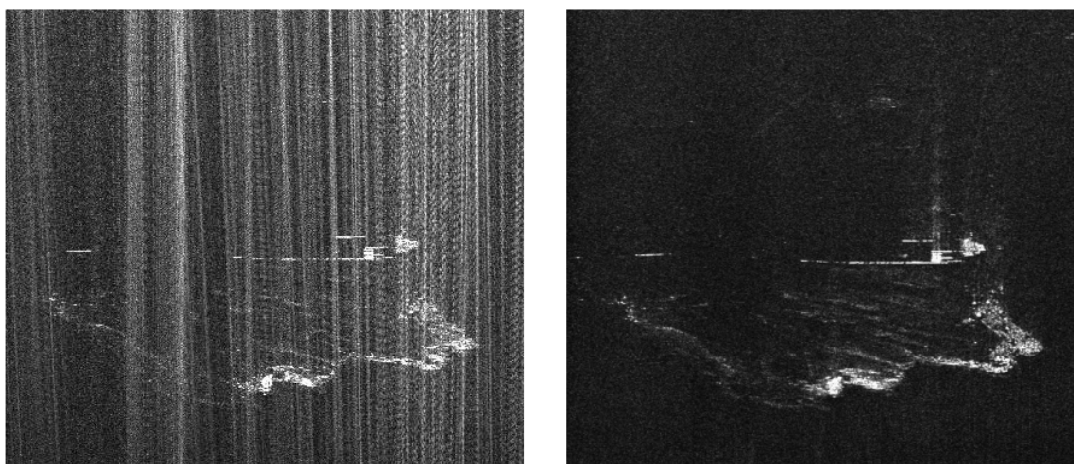
**Figure 1.3:** *SASAR image of Cape Agulhas before and after radio frequency interference suppression. The flight path is along the horizontal axis, with near range towards the bottom of the image.*
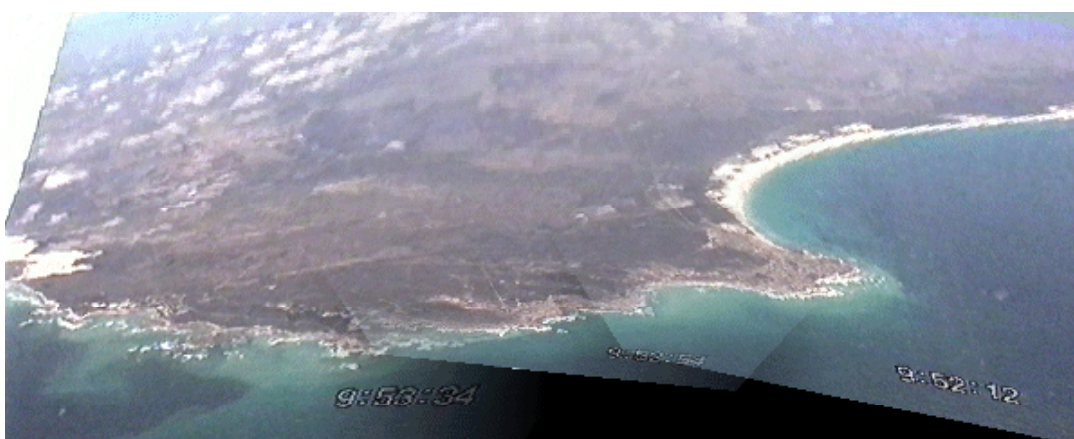


**Figure 1.4:** *Mosaic of video frames of the Cape Agulhas area recorded at the same time as the radar data.*

An example illustrating the importance of RFI suppression is shown in Figure 1.3, which shows a SASAR image of Cape Agulhas, the southern tip of Africa, before and after suppressing the RFI using an LMS adaptive filter. During the SASAR flight, a video image was recorded through a window of the aircraft. A mosaic of video frames of the corresponding area is shown in Figure 1.4. The example shown in Figure 1.3 highlights that even in this remote area the RFI is very significant, showing up as bright white streaks in the image. Suppression of the RFI has significantly improved the image quality, demonstrating the importance of suppressing RFI at VHF/UHF frequencies.

## 1.5 Thesis Objectives

This thesis investigates the following two aspects of low-frequency (VHF/UHF) SAR processing:

1. The use of stepped-frequency waveforms to synthesise higher total bandwidths and therefore higher range resolution, and

2. Radio frequency interference suppression.

Since RFI is a major problem for SAR systems operating in the VHF/UHF region, it is proposed to skip those frequency steps that would be heavily contaminated with interference. Alternatively, the frequency step size and/or the individual transmit bandwidths within a burst of pulses can be varied in order to notch out more specific interference regions of the spectrum. This process will reduce the likelihood of receiver saturation. The remaining interference can then be suppressed by applying appropriate RFI suppression techniques on the sampled data.

The objectives of this thesis can be summarised as follows:

- Review and describe available stepped-frequency processing techniques.

- Implement available stepped-frequency processing techniques on simulated data and on real stepped-frequency data obtained from an L-band search radar which took downrange profiles of aircraft targets. Investigate the suitability of this processing technique for SAR processing applications.

- Develop an alternative method of processing stepped-frequency data, which is more suitable for SAR processing applications.

- Implement this method on simulated data, showing how this technique may be used to avoid spectral regions which are heavily contaminated with RFI.

- Review available RFI suppression techniques and implement a suitable method to suppress RFI.

- Apply this method on simulated data, on real P-band data generated by the experimental airborne SAR system E-SAR of the DLR, and on real VHF-band data generated by the South African SAR (SASAR) system.

- Investigate means to implement the RFI suppression algorithm more efficiently and to combat unwanted sidelobes that might arise due to the suppression algorithm.

## 1.6    Thesis Development

Chapter 2 reviews relevant SAR theory and describes the concept of range resolution. It is shown how stepped-frequency waveforms may be used as a means of synthetically increasing the total radar bandwidth, thereby increasing the range resolution. Stepped-frequency waveforms also provide opportunities for RFI suppression by avoiding spectral regions that contain strong interferers, and they also help to increase the receiver dynamic range, because the task of the A/D converters is less demanding since they only have to sample the narrowband pulses.

After motivating the use of stepped-frequency waveforms, three methods of processing stepped-frequency waveforms are described, namely:

- An IFFT method;

- A time-domain method;

- A frequency-domain method.

The IFFT method is successfully used to obtain high resolution synthetic downrange profiles of targets such as aircraft. Simulation results are shown, as well

as results processed from real stepped-frequency data obtained from an L-band search radar taking downrange profiles of aircraft targets. Although successful results have been obtained, this technique has the drawback that target energy spills over into consecutive coarse range bins, leading to multiple instances of the target (also called "ghost targets") in neighbouring coarse range bins. This drawback makes this method unsuitable for SAR processing purposes.

The time-domain technique involves the reconstruction of a wideband chirp waveform from an ensemble of narrowband chirp waveforms stepped in frequency. It is implemented on simulated data and on real E-SAR data. This technique is, however, inefficient, mainly due to the upsampling requirement of the narrow-bandwidth signals.

The inefficiencies of the time-domain technique have, in part, led to the development of a more efficient frequency-domain technique. This technique involves the reconstruction of a wider portion of the target's reflectivity spectrum by combining the individual spectra of the transmitted narrow-bandwidth pulses in the frequency domain.

Chapter 3 describes the frequency-domain approach of processing stepped-frequency data in more detail. The technique is verified and illustrated by implementing it on simulated data. It is shown how this technique may be used to avoid specific spectral regions contaminated with RFI. The remainder of the interference can then be suppressed by a suitable RFI suppression technique.

Chapter 4 describes and discusses several RFI suppression methods. These include spectral estimation and coherent subtraction algorithms and various filter approaches. The notch filter and the LMS adaptive filter are implemented on P-band data obtained from the DLR, as well as on VHF-band data obtained from the locally-built SASAR system.

A quality index is defined to monitor the performance of the LMS adaptive filter. This index is employed to validate the use of the same set of filter tap weights for many successive range lines. It is explained how the equivalent transfer function of the LMS adaptive filter may be obtained and combined with the matched filter transfer function of the range compression stage of the range-Doppler SAR processing algorithm. Since the equivalent transfer function of the RFI suppression stage is often effective for hundreds of range lines, significant computational savings can be achieved.

There is discussion of a technique that has been developed to reduce the side-lobes that appear as an unwanted by-product when the LMS adaptive filter is used to suppress RFI. The sidelobe reduction procedure can be written in terms of the equivalent transfer function of the LMS adaptive filter. Thus, a combined transfer function can be obtained which implements RFI suppression, sidelobe reduction and range compression simultaneously, thereby leading to a very efficient implementation.

Chapter 5 summarises the work and gives recommendations for future research.

## 1.7    Statement of Originality

The candidate's original contributions in this thesis are summarised as follows:

Chapter 2 (Obtaining High Resolution from Narrowband Stepped-Frequency Pulses) — This chapter describes three methods of processing stepped-frequency data, namely an IFFT method, a time-domain method and a frequency-domain method.

The IFFT method is described and implemented on simulated data and on real data. Both the simulation results and the results from an L-band search radar taking downrange profiles of aircraft targets have been used to show that this method is not suitable for SAR processing applications. The description of the limitations of the IFFT approach for SAR processing applications has not been documented in the literature. Furthermore, the coding and the implementation of the IFFT method on stepped-frequency data are the candidate's own work.

The time-domain technique for processing stepped-frequency data was developed entirely by the candidate. However, this approach, which involves the reconstruction of a wideband chirp waveform from an ensemble of narrowband chirp waveforms stepped in frequency, is shown to be inefficient, mainly because the narrow-bandwidth signals need to be upsampled.

The frequency-domain approach involves the reconstruction of a wider portion of the target's reflectivity spectrum by combining the individual spectra of the transmitted narrow-bandwidth pulses in the frequency domain. The concept and mathematical modelling of reconstructing a target's reflectivity spectrum was suggested to the candidate by Andrew Wilkinson (Wilkinson 1996). A similar

technique, based on the same principle, has been developed independently by the CARABAS group (Ulander and Frölind 1999). To the best of the candidate's knowledge, however, the concept of describing this technique in terms of the target reflectivity profile is novel.

Chapter 3 (Reconstruction of Target Reflectivity Spectrum) — This chapter describes the frequency-domain approach of processing stepped-frequency data in more detail. The technique is verified and illustrated by implementing it on simulated data. The concept of skipping frequencies which would otherwise be corrupted by RFI has not been documented in the literature. It is shown that both the frequency step sizes and the individual transmit bandwidths within a burst of pulses can be varied. This offers more flexibility in notching out specific regions of the spectrum which contain dominant interferers. The candidate is indebted to Andrew Wilkinson (RRSG, UCT) for the mathematical modelling and description of this technique (Wilkinson 1996). Only the coding and implementation of this method on simulated data are the candidate's own work.

Chapter 4 (RFI Suppression for VHF/UHF SAR) — The candidate has been involved extensively with the RFI suppression aspect of the SASAR system. Apart from assessing the suitability of the notch filter and the *least-mean-squared* (LMS) adaptive filter to suppress RFI in P-band and VHF-band images, original contributions of this chapter include modifications to these filters in order to enhance their performance. These modifications involve the use of a median filter to obtain an approximation of the signal spectrum envelope, which is then used by the notch filter to identify and remove interference spikes. Furthermore, the notch filter has been efficiently integrated with the range-compression stage of the range-Doppler SAR processor.

Modifications to the LMS adaptive filter include sweeping the filter through each range line from both ends and then averaging the two outputs, sweeping the filter through each range line twice to allow better convergence of the weight vector, and zero-padding each range line to reduce edge effects. The issue of finding optimal filter parameters is discussed, as well as the issue of whether the same filter tap weights may be used over many successive range lines.

More novel work concerning the LMS adaptive filter includes re-writing it in terms of an equivalent transfer function, which facilitates efficient integration with the range-Doppler algorithm. Furthermore, a novel technique is described

to reduce range sidelobes, which arise as an unwanted by-product of the RFI suppression stage. It is shown that the interference suppression and the side-lobe reduction can be integrated with the range-compression stage of the range-Doppler algorithm, thereby resulting in a very efficient implementation. The development, coding, simulation and testing of both the notch filter and the LMS adaptive filter is the candidate's own work.

# Chapter 2

# Obtaining High Resolution from Narrowband Stepped-Frequency Pulses

## 2.1 Introduction

This chapter introduces the concept of side-looking strip-map SAR in Section 2.2 and briefly describes the steps involved to form a two-dimensional SAR image. An important characteristic of a SAR image is its resolution, which is defined in terms of the minimum distance at which two closely spaced scatterers of equal strength may be resolved. The concept of *range* resolution, which is the resolution in the cross track dimension, is described in Section 2.3. It is shown that the range resolution of a SAR system is directly dependent on the transmitted bandwidth, which may be synthetically increased by utilising stepped-frequency waveforms. Section 2.4 describes some of the implications of using stepped-frequency waveforms, such as the increase of the *pulse repetition frequency* (PRF), velocity compensation and motion compensation.

In order to obtain the high-resolution range profile from a burst of narrowband pulses stepped in frequency, some kind of signal processing has to be performed on the data. This chapter describes two methods of processing stepped-frequency waveforms so as to produce high-resolution range profiles known as *synthetic range profiles* (SRPs) (Wehner 1995), namely:

1. An IFFT method;

2. A time-domain method.

Both of these methods are shown to be either unsuitable or too inefficient for SAR processing applications. Chapter 3 describes a further method of processing stepped-frequency waveforms which does not suffer from the drawbacks of the two methods described in this chapter.

The IFFT method involves taking an inverse FFT of the sampled stepped-frequency data, and is described in detail by (Wehner 1995), (Scheer and Kurtz 1993) and (Currie and Brown 1987). A brief description of this method is given in Section 2.5, and Section 2.5.2 describes simulation results. Section 2.5.3 describes the results obtained from implementing this method on real stepped-frequency data obtained from an L-band search radar taking downrange profiles of aircraft targets. This work was part of a *non-cooperative target recognition* (NCTR) project carried out at the *University of Cape Town* (UCT) (Lengenfelder 1998a).

The simulation results and the experience gained from processing the aircraft data have shown that the IFFT method is unsuitable for processing SAR images, mainly because of the spill-over effect due to matched filtering, which causes multiple "ghost" images to appear in the final range profile. Original contributions contained in this section include an analysis of the practical experience gained from applying this method to real stepped-frequency aircraft data, and the illustration of the shortcomings of this method as it pertains to SAR processing applications. The coding and the implementation of the IFFT method on stepped-frequency data is the candidate's own work. Some of the material in this section has been published in the Proceedings of IGARSS'96 (Lord and Inggs 1996).

The time-domain technique for combining stepped-frequency waveforms to produce high-resolution synthetic range profiles does not suffer from the "ghost-target" drawback and is thus more suitable for SAR processing applications. It involves the reconstruction of a wideband chirp waveform from the ensemble of narrowband chirp waveforms stepped in frequency and is described in Section 2.6. All the signal processing operations are performed in the time-domain. It is shown that this method is inefficient mainly on account of the upsampling requirement of the narrow-bandwidth signals. However, it is nevertheless included in this thesis because it does present a novel and feasible method for combining stepped-frequency waveforms to process SAR images and because it is perhaps useful for time-domain SAR processors. Results obtained from processing simulated data and real E-SAR data are presented and discussed. Some of the work

described in this section has been published in the Proceedings of IGARSS'97 (Lord and Inggs 1997b) and in the Proceedings of COMSIG'97 (Lord and Inggs 1997a).

The methods described in this chapter adopt the start-stop approximation, which means that the radar-target range remains constant during the transmission of one burst of frequencies. It is assumed that the entire sub-band signals are collected before the aircraft moves by half of the antenna size. This ensures that the largest Doppler variation among all sub-band signals will be small. Although azimuth compression and range curvature correction are essential for obtaining high resolution SAR images, this thesis is only concerned with the issue of obtaining high range resolutions. Motion compensation is another important consideration for airborne SAR systems, but is only briefly discussed in Section 2.4.3. Another problem not discussed at all in this thesis is the variation of the radar response with frequency and observation angle (Axelsson 1995), which varies significantly over the synthetic aperture path.

## 2.2   Side-Looking Strip-Map SAR

An intuitive introduction to basic SAR theory is given by (Stimson 1983). More advanced treatments on basic SAR theory are provided by (Vant 1989), (Kirk 1975), (Sack, Ito and Cumming 1985) and (Munson and Visentin 1989). A theoretical basis for understanding SAR images is provided by (Oliver and Quegan 1998). Other texts with a treatment of SAR theory are offered by (Curlander and McDonough 1991), (Skolnik 1990), (Elachi 1988) and (Fitch 1988).

The data for a SAR image is collected by an aircraft or satellite with a side-looking antenna, which transmits a stream of radar pulses and records the backscattered signal corresponding to each pulse. The rate or pulse repetition frequency (PRF) at which pulses are transmitted and received may be constant or may vary over time. Varying the PRF allows the system to maintain a constant spatial distance between pulses if the sensor velocity changes. Since the moving antenna beam covers a strip of the earth's surface, this type of SAR imaging is referred to as strip-map SAR.

Figure 2.1 shows the strip-map SAR geometry. The radar antenna is pointed to the side of the aircraft towards the ground and orthogonal to the flight track. As
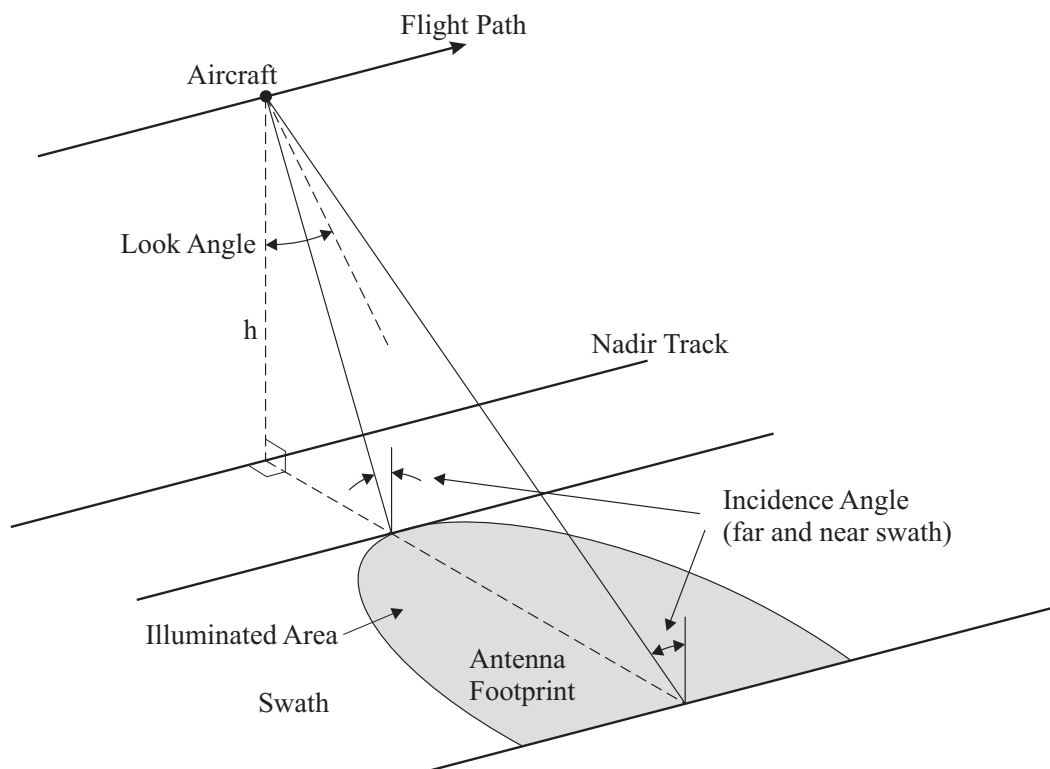
**Figure 2.1:** *Side-looking strip-map SAR geometry.*

the aircraft moves, a swath is mapped out on the ground by the antenna footprint. The radar transmits pulses at the pulse repetition frequency, $f_{\mathrm{prf}}$, and for each pulse the backscatter return from the ground is sampled in range at the *analogue-to-digital* (A/D) sampling frequency, $f_{ad}$. The radar operation is coherent, which means that both the return magnitude and phase (with respect to the transmitted signal) are sampled. For each range sample the in-phase and quadrature values ($I$ and $Q$) are stored. The raw data file is thus a two-dimensional array of complex values (with $I$ as the real part and $Q$ as the imaginary part), with range (cross track or fast time) as one dimension and the transmitted pulse number (along track or slow time) as the other dimension. This two-dimensional data set is then processed to form an image. SAR processing algorithms include the *range-Doppler algorithm* (Munson and Visentin 1989), the *chirp scaling algorithm* (Raney, Runge, Bamler, Cumming and Wong 1994), (Moreira, Mittermayer and Scheiber 1998), and the *range migration algorithm* (Cafforio, Prati and Rocca 1991), (Carrara et al. 1995a). A comparison of SAR processing algorithms is given by (Bamler 1992).

## 2.3 Range Resolution

### 2.3.1 Definition

*Resolution* can be defined as the minimum distance that describes how well the radar discriminates closely-spaced reflectors (Raney 1998). For any system, the available resolution is proportional to the reciprocal of the system bandwidth (Raney 1998). For radars employing pulse compression techniques, the resolution actually achieved also depends on many additional factors, including signal coherence and the precision with which the processor is able to match the signal modulation.

Formally, the definition of resolution requires two test targets of equal strength, and is given as the minimum spacing for which the targets in the image are discernable as being two separate objects. In practice, however, radar resolution is taken to be the width of a single impulse response, referred to as the *impulse response width* (IRW). The IRW may be specified either as the 3 dB width, which is the width of the pulse at its half power level, or as the equivalent rectangle width, which is the width of a rectangular representation of the pulse that has the same peak power and the same integrated power (energy). This thesis uses the 3 dB width definition to measure resolution.

### 2.3.2 Direct short pulse

The system bandwidth $B$ of a radar that uses a short pulse waveform is approximately equal to the inverse of the transmitted pulse length $T_p$, and therefore the slant range resolution $\rho_r$ is given by

$$\rho_r = \frac{c}{2B} \approx \frac{cT_p}{2} \tag{2.1}$$

Hence, the resolution relates to the narrowness of the transmitted pulse.

The average transmitted power $P_{\text{av}}$ of short pulse waveforms is limited to

$$P_{\text{av}} = P_{\text{peak}} \, T_p \, f_{\text{prf}} \tag{2.2}$$

where $P_{\text{peak}}$ is the peak transmitted power and $f_{\text{prf}}$ is the pulse repetition frequency. Thus, for fixed peak power and PRF, increasing the average transmitted

power will require wider pulsewidths with lower range resolution. This is a practical limitation of the short pulse waveform.

### 2.3.3 Pulse compression

In order to achieve increased average transmitted power and simultaneously to obtain wide bandwidth for high range resolution, pulse compression techniques are used. Pulse compression systems transmit a frequency- or phase-modulated waveform, which can be compressed with signal processing operations after reception.

The linear FM or chirp waveform is the popular choice for fine-resolution SAR systems (Skolnik 1990). It is described by

$$p(t) = \cos\left[2\pi\left(f_c t + \frac{\gamma t^2}{2}\right)\right] \ \text{for} \ |t| \leq \frac{T_p}{2} \tag{2.3}$$

where $f_c$ is the carrier frequency and $T_p$ is the pulse length. Its frequency is a linear function of time, varying at a rate $\gamma$ referred to as the chirp rate. Correspondingly, its phase is a quadratic function of time. The bandwidth $B$ of the pulse is approximately equal to the rate of change of frequency multiplied by the pulse length, which gives $B \approx \gamma T_p$. The resolution is also proportional to a window constant $K_r$ which is dependent on the type of weighting used to suppress sidelobes during either range or azimuth compression. From (Harris 1978), the window constant is 0.89 for a rectangular weighting function, and 1.30 for a Hamming weighting function. The slant range resolution is given in terms of the window constant as

$$\rho_r = \frac{cK_r}{2B} \tag{2.4}$$

The range compression factor is the ratio of the pulse's length before time compression, $T_p$, to its length after compression, $1/B$. This *pulse compression ratio* (PCR) is

$$\text{PCR} = T_p B \approx \gamma T_p^2 \tag{2.5}$$

The PCR is thus equal to the time-bandwidth product of the transmitted pulse and represents the improvement in resolution that pulse compression offers, assuming $K_r$ in Equation 2.4 is unity.

The availability of higher average power offered by pulse compression techniques overcomes the related sensitivity problem with the narrow pulse system. How-

ever, if the *instantaneous* bandwidth required for the processing (sampling, A/D conversion and recording) of the compressed narrow pulse is very large, the demands placed on the system hardware might make it economically not viable.

## 2.3.4   Stepped-frequency waveform

The stepped-frequency waveform overcomes the wide instantaneous bandwidth problems associated with a pulse compression system. Rather than transmitting a wide-bandwidth signal as a single pulse at each sensor location, the stepped-frequency system constructs its wide-bandwidth signal at each sensor location over a group of narrow-bandwidth pulses, stepped at a fixed frequency step size $\Delta f$. As already mentioned in the previous chapter (Section 1.3), further advantages of using stepped-frequency waveforms include an increase in receiver dynamic range (since the A/D converters only have to sample the instantaneous *narrowband* pulses), and also offer the possibility of avoiding spectral regions contaminated with RFI. Furthermore, the stepped-frequency operation can be used to synthesize a longer pulse to improve the system SNR.

The disadvantages of using stepped-frequency waveforms include the increase in PRF and the need for velocity compensation in the case of moving targets. These aspects are described in Sections 2.4.1 and 2.4.2. The requirement for separate motion compensation for each pulse in a burst is described in Section 2.4.3. This requirement might be an advantage of stepped-frequency processing in the sense that it opens the possibility of performing more accurate and more efficient motion compensation; however, this aspect requires further work. There is also an increased complexity of the signal processing involved in combining the narrowband pulses. The sections following Section 2.4 describe two methods of processing stepped-frequency waveforms, namely:

1. An IFFT method;

2. A time-domain method;

A further frequency-domain method of processing stepped-frequency data is described in Chapter 3.

## 2.4 Stepped-Frequency Processing Implications

### 2.4.1 PRF and unambiguous range

Range ambiguity exists when the backscattered energy from a particular transmitted pulse arrives back at the radar during the reception period of another pulse. To ensure that no range ambiguities arise from the mainlobe illumination, an upper limit on the PRF may be imposed. For airborne systems the trailing edge of the backscattered pulse from a point target at the maximum range must be received before transmission of the next pulse. Using this criterion, the maximum range is given by

$$r_{\max} = \frac{c}{2f_{\mathrm{prf}}} - T_p c \tag{2.6}$$

The second term of the above equation, which is the pulse duration, is generally small in comparison to the first term and is therefore usually neglected (Horrell 1999).

The increase in PRF of a stepped-frequency system is proportional to the number of frequency steps contained in a burst, $n$. For systems employing a large number of frequency steps, the technique of multiple PRF ranging (Hovanessian 1984) may be used to increase the unambiguous range.

Another possibility for increasing the PRF is to use more than one receiver. Using two receivers effectively permits the PRF to be doubled. However, every time a pulse is transmitted all receivers will have to be switched off to avoid leakage of energy from the transmitter to the receivers. The gap in the received data during the transmit intervals may have to be interpolated, or the PRF would need to be dithered to avoid this gap occurring at the same position every time
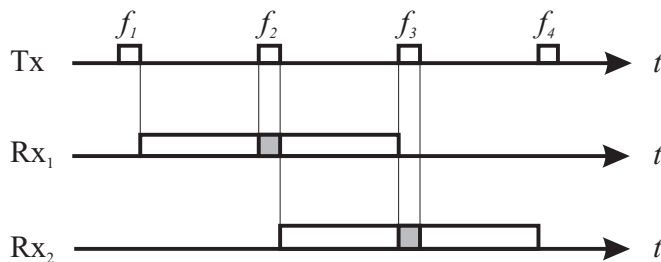


***Figure 2.2:*** *Gap in received data when using multiple receivers.*

a pulse is transmitted. This gap in the received data is illustrated by the grey areas in Figure 2.2.

## 2.4.2 Velocity compensation

The stepped-frequency signal processing methods described in this chapter all assume that the illuminated target is stationary. If the target is moving, the range-shift that results from the target being at a slightly different position on a pulse-to-pulse basis can be compensated for by multiplying the spectrum of each return by an appropriate phase ramp, according to the Fourier time-shift theorem

$$f(t - t_i) \Rightarrow F(\omega) \, e^{-j\omega t_i} \tag{2.7}$$

with

$$t_i = \frac{2 \, \Delta r_i}{c} \tag{2.8}$$

and

$$\Delta r_i = \frac{i \, v_t}{f_{\mathrm{prf}}} \tag{2.9}$$

where $i = 0 \ldots (n - 1)$ with $n$ representing the number of frequency steps in one burst and $v_t$ is the radial velocity of the target, positive values representing approaching targets. In practice, the resulting range-shift of moving targets will be less than the width of one coarse range bin, given for example the parameters of the L-band search radar shown in Table 2.1. It is therefore more important to compensate for the phase shift that results from the target being at a different location at each frequency step. The appropriate phase, that has to be added to each return, is given by

$$\phi_i = \frac{-4\pi \, \Delta r_i \, f_i}{c} \tag{2.10}$$

where $f_i$ is the centre frequency of the $i$ th frequency step.

## 2.4.3 Motion compensation

Motion compensation is an important topic for airborne SAR systems, and especially for ultra-wideband SAR systems. It requires that all signals are effectively moved along a straight reference line which is defined along the aircraft flight line. In this way, equally spaced azimuth samples along this straight reference line can be derived for the azimuth compression operation.

A similar task is performed when all the sub-band signals are combined to effectively form a signal which is the same as the received echo with one continuous transmit signal under the start-stop approximation. It is important that all the sub-band signals are combined coherently without any discontinuities at the sub-band boundaries. If any discontinuities in phase or amplitude exist, the range resolution may degrade and the sidelobe level may increase. Furthermore, all sub-band signals must be collected before the aircraft moves by half the antenna length, in order to satisfy the Nyquist sampling requirement. When combining the sub-band data, each sub-band is effectively moved to one point along the flight line. Therefore, when the sub-band data are combined, the motion compensation can be implemented simultaneously.

Although motion compensation has not been investigated in this thesis, it is noteworthy to mention that the motion compensation phase shift applied to each range line is dependent on the centre frequency of the transmitted pulse. Referring to Equation 2.29, the baseband returned signal after demodulation is

$$v_{bb}(t, i) = p\left(t - t_0\right) \exp\left(-j2\pi f_i t_0\right) \tag{2.11}$$

where the phase term $\exp\left(-j2\pi f_i t_0\right)$ includes the carrier frequency $f_i$ of the $i$ th frequency step, *and* an expression for the time shift $t_0 = \frac{2r_t}{c}$, determined by the radar-target distance $r_t$. For a stepped-frequency system this implies that separate motion compensation must be performed on each narrowband pulse, rather than applying motion compensation to the reconstructed wideband signal.

More information on motion compensation, particularly regarding the SASAR system, is given by (Horrell 1999).

## 2.5   IFFT Method

### 2.5.1   Overview

To obtain a high-resolution synthetic range profile from stepped-frequency data using the IFFT method entails the following steps (Wehner 1995):

1. Transmit a burst of $n$ pulses, each pulse shifted in frequency by a fixed frequency step size, $\Delta f$.

26

2. Collect one $I$ and $Q$ sample of the target's baseband echo response in each coarse range bin for every transmitted pulse. These samples can be regarded as the frequency-domain measurements of the target's spectral profile.

3. Apply an IFFT to the $n$ complex samples in each coarse range bin to obtain an $n$-element SRP of the target in the respective coarse range bin.

Stepping the centre frequency by the frequency step size $\Delta f$ has the effect of producing a pulse-to-pulse phase shift which manifests itself within the radar as an apparent Doppler frequency. This apparent Doppler frequency is a function of the range to the target. The phase, $\phi_1$, of the returned signal associated with a transmitted pulse of frequency $f_1$ is given by

$$\phi_1 = \frac{4\pi r f_1}{c} \tag{2.12}$$

for a non-moving target at range $r$. If a pulse at a different frequency, $f_2$, is transmitted, then the phase, $\phi_2$, of the signal returning from a non-moving target would be

$$\phi_2 = \frac{4\pi r f_2}{c} \tag{2.13}$$

For a sequence of pulses, where each pulse is equally spaced from adjacent pulses by a frequency step of $\Delta f$, there is a predictable pulse-to-pulse phase shift of $\Delta \phi$ for a fixed target, which is given by

$$\Delta \phi = \phi_2 - \phi_1 = \frac{4\pi r \Delta f}{c} \tag{2.14}$$

The spectral analysis performed to obtain a range profile of the target takes the form of an inverse fast Fourier transform (IFFT) of the ensemble of received pulses, since frequency maps to range as a result of the IFFT process. These conditions only apply for non-moving targets which exhibit no true Doppler frequency shift. If the target has a radial component of relative velocity, then Doppler effects will shift the apparent range to the target, as an unavoidable effect of the IFFT process.

The synthesised unambiguous range length $w_s$, which is the length of the synthesised range profile after the IFFT process has been performed, is determined by the frequency step size and is given by

$$w_s = \frac{c}{2\Delta f} \tag{2.15}$$

The synthesised unambiguous range length has to be at least as long as the pulse length of the radar. If it is less than the pulse length, any target returns after the unambiguous range will be aliased into the synthetic range profile (Wehner 1995). Note that the synthesised or SRP unambiguous range is not the same as the normal radar unambiguous range (see Section 2.4.1). If the received signal is sampled at a rate greater than $\Delta f$, which means that the sample spacing in metres is less than the synthetic range length, adjacent range profiles will overlap. The percentage overlap between SRPs of successive coarse range bins is calculated from

$$\% \text{ overlap} = \frac{w_s - \Delta\rho_r}{w_s} \cdot 100\% \qquad (2.16)$$

where $\Delta\rho_r$ is the sample spacing given by

$$\Delta\rho_r = \frac{c}{2f_{ad}} \qquad (2.17)$$

and $f_{ad}$ is the A/D (complex) sampling rate.

The synthetic range resolution $\rho_r$ may be defined as the synthetic range length divided by the number of frequency steps (Wehner 1995), which gives

$$\rho_r = \frac{w_s}{n} = \frac{c}{2n\Delta f} \qquad (2.18)$$

For the case where $B_{tx} = \Delta f$, the range resolution would therefore be increased by a factor of $n$, the number of frequency steps. A restriction on the required $\Delta f$ as a function of the transmitted pulsewidth is that undersampling of the apparent Doppler (induced by the frequency stepping) must not occur. This requires that $\Delta f$ be no larger than $B_{tx} \approx 1/T_p$ for a purely rectangular pulse (Currie and Brown 1987). Generally, the frequency step size is chosen to be approximately equal to $1/(2T_p)$ (Currie and Brown 1987).

## 2.5.2   Simulation results

Point target simulations have been conducted in order to illustrate the IFFT method of producing SRPs. The results obtained from these simulations are shown in Appendix A.

These simulations have shown that the IFFT method can produce high resolution range profiles of targets. However, the target should, ideally, be contained in only one coarse range bin. Because target energy spills over into neighbouring

coarse range bins, this method is not suited to the production of range profiles of extended targets covering many coarse range bins, and is therefore also not suited for SAR processing applications.

## 2.5.3   Results from stepped-frequency aircraft data

Over the last few years a substantial amount of work has been carried out at UCT to produce SRPs of aircraft targets using an L-band search radar. The high range resolution that can be obtained from SRP processing makes it feasible to extract characteristic features from a profile obtained from an aircraft. The ultimate aim of producing SRPs is to use these extracted features for non-co-operative target recognition (NCTR), so as to be able to identify an aircraft type from the echo signal received by the radar. The feasibility of using stepped-frequency waveforms to produce high resolution down-range profiles has already been demonstrated by the production of SRPs of aeroplanes (Robinson and Inggs 1994). More information regarding the NCTR project can be obtained from (Inggs and Lord 1996) and (Lengenfelder 1998a).

| Start frequency | $f_0$ | 1265.0 MHz |
|---|---|---|
| Frequency step size | $\Delta f$ | 1.5 MHz |
| Number of steps | $n$ | 66 |
| Chirp bandwidth | $B_{tx}$ | 3.6364 MHz |
| ADC sample rate | $f_{ad}$ | 3.75 MHz |
| Number of coarse range bins | | 64 |
| Coarse range bin length | $\Delta \rho_r = \frac{c}{2\,f_{ad}}$ | 40.0 m |
| Pulse length | $T_p$ | 5 $\mu$s |
| Antenna Rotation Rate | $\dot{\theta}$ | 30 rpm |

**Table 2.1:** *Parameters of L-band stepped-frequency radar system.*

Table 2.1 summarises the parameters of the radar system used to obtain the stepped-frequency aircraft database. The total radar bandwidth is given by

$$
\begin{aligned}
B_t &= n\,\Delta f \\
&= 66 \cdot 1.5\,\text{MHz} = 99\,\text{MHz}
\end{aligned}
\tag{2.19}
$$

which gives a synthetic range profile resolution of

$$
\rho_r = \frac{c}{2\,B_t} = 1.52\,\text{m}
\tag{2.20}
$$

29

This resolution is expected to be sufficient to resolve the characteristic features of an aircraft, such as the cockpit, hull, engines, etc. The length of the synthetic range profile is

$$w_s = \frac{c}{2\,\Delta f} = 100\,\mathrm{m} \tag{2.21}$$

This length should be sufficient to contain even the largest aircraft. Since the returned echo is sampled every $\frac{c}{2\,f_{ad}} = 40\,\mathrm{m}$, the synthetic range profiles associated with the coarse range bins have an overlap of $60\,\mathrm{m}$.

The experience gained from producing synthetic range profiles from the stepped-frequency aircraft data is summarised as follows:

- Decide whether or not to do *moving target indication* (MTI) processing.

  For each frequency step, two pulses were transmitted, in order to perform MTI processing, which is implemented by subtracting the return of one pulse from the return of the other. However, this has not always yielded the best results, especially when the radial speed of the aircraft was low. The SRPs shown in this thesis have been obtained by taking the *average* of the two pulses.

- Remove the DC component of the data.

  An analysis of the data has revealed that the $I$ and $Q$ values of the data contain a DC-offset. (This offset would not be as severe if MTI processing had been applied.) If this offset is not removed, the IFFT operation produces a DC peak, which will mistakenly be regarded as an aircraft feature.

- Apply velocity compensation.

  It has been shown that velocity compensation is very important in order to produce accurate range profiles. Unfortunately, the radial velocity is not accurately known for the aircraft data. An estimate has been calculated by interpolating the flight path described in the recorded data log file.

- Select the coarse range bin containing the target.

  From the 64 coarse range bins, select the one with the maximum absolute peak value, since it is the one most likely to contain the aircraft. Instances where this was not the case could usually be attributed to clutter return.
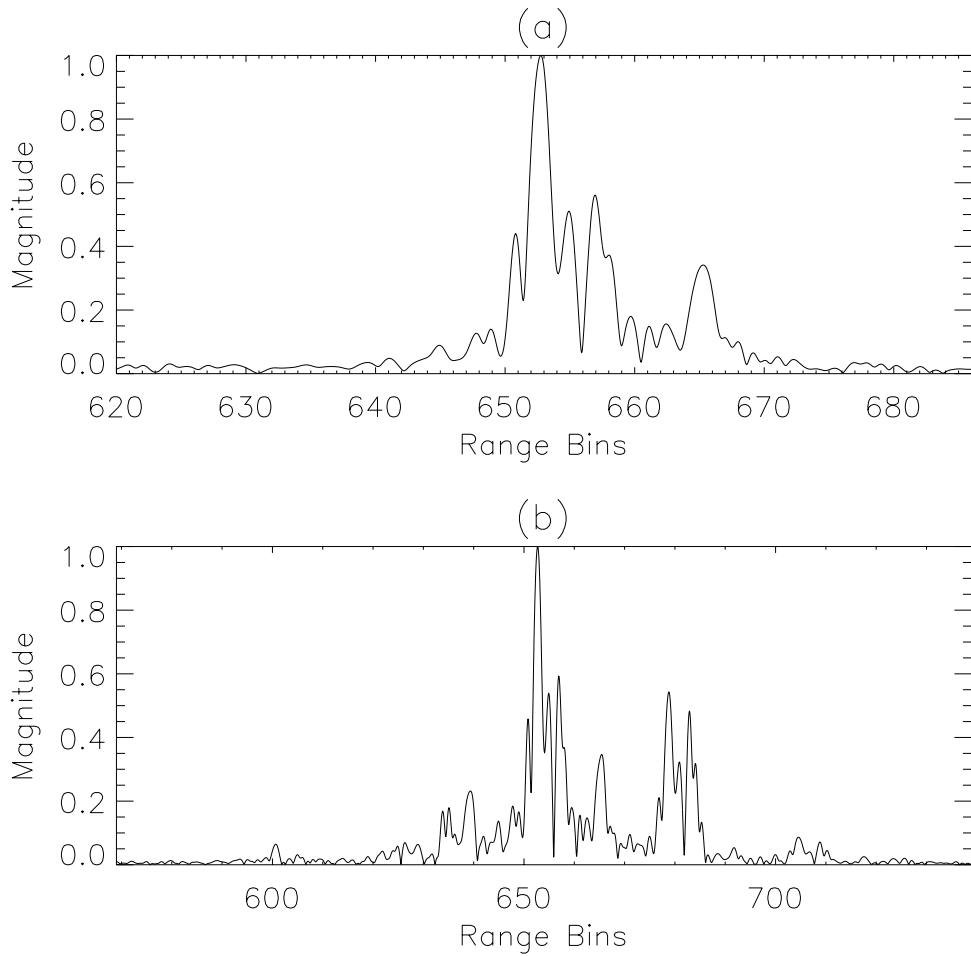
**Figure 2.3:** *(a) Synthetic range profile of a real Boeing 737; (b) Five adjacent SRPs of the Boeing, appropriately overlapped.*

- Apply an IFFT across all 66 frequency steps to obtain the SRP.

  A circular shift may be applied to the result in order to display the peak in the centre of the profile.

Figure 2.3 (a) shows the synthetic range profile of a real Boeing 737, which has been upsampled by a factor of 20. Figure 2.3 (b) shows five adjacent, overlapped range profiles of the Boeing. A large amount of spill-over of target energy into neighbouring range bins is evident.

### 2.5.4   SAR processing using IFFT method

In order to perform SAR processing from stepped-frequency waveforms, it is important that the process which combines the stepped-frequencies should produce synthetic range profiles that do not contain repeated target artefacts or so-called "ghost" targets. The IFFT method described in this chapter is a very efficient and easy way of obtaining high-resolution range profiles of targets such as aircraft. Although successful results have been obtained, the IFFT-based method is not a true model for reconstructing target profiles, but rather a robust estimator. Due to the matched filter effect, and because of sampling at a rate greater than the Nyquist rate, target energy spills over into neighbouring coarse range bins. This causes repeated replicas of the target to appear in the resulting synthetic range profile. The simulation results and the results obtained from real stepped-frequency aircraft data have shown that these "ghost" images are very significant, and therefore the IFFT method is not a suitable method to use when processing stepped-frequency SAR data.

The next section introduces an alternative method of producing synthetic range profiles which does not produce these "ghost" targets and is therefore more suitable for stepped-frequency SAR processing applications.

## 2.6   Time-Domain Reconstruction of Wideband Chirp Signal

### 2.6.1   Introduction

The concept of combining an ensemble of narrow-bandwidth chirp waveforms to produce one wide-bandwidth chirp waveform is illustrated in Figure 2.4. In the figure, two narrow-bandwidth chirp waveforms at baseband are shown. Before combining these two waveforms coherently to form the wide-bandwidth chirp waveform, they have to be upsampled and shifted in frequency, and a phase-correction term has to be added to each of them.

Since the narrow-bandwidth chirp waveforms are essentially fractions of a reconstructed wide-bandwidth chirp waveform, it is required that each of them should have the same chirp rate $\gamma$. Furthermore, in order to avoid gaps or overlaps in
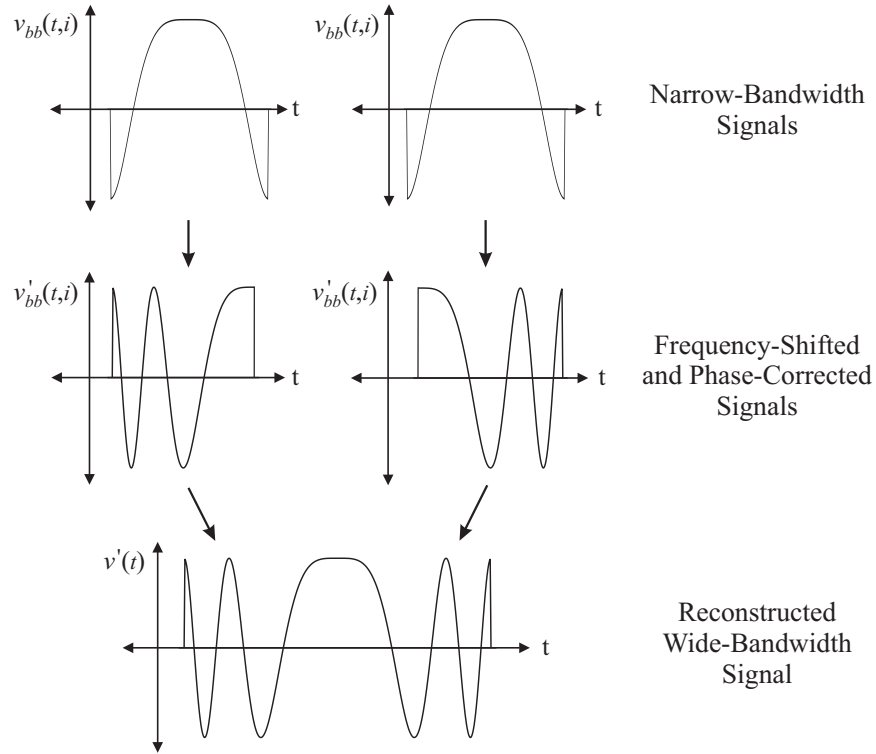
**Figure 2.4:** *Combination of narrow-bandwidth chirp waveforms to form one wide-bandwidth chirp waveform.*

the reconstructed chirp waveform, the narrowband pulse lengths $T_p$ and the corresponding bandwidths $B_{tx} = \gamma T_p$ have to be chosen carefully. The derivation that follows assumes for simplicity that the narrowband pulses each have the same bandwidth $B_{tx} = \frac{B_t}{n}$, where $B_t$ is the total radar range bandwidth, and that the frequency spacing between individual pulses is $\Delta f = B_{tx}$.

## 2.6.2 Waveform modelling

A linear FM chirp waveform at baseband can be described by

$$p(t) = A \operatorname{rect}\left(\frac{t}{T_p}\right) \exp\left(j\pi\gamma t^2\right) \tag{2.22}$$

where $A$ is the amplitude, $T_p$ the pulse length and $\gamma$ the chirp rate. The spectrum is approximately rectangular with bandwidth $B_{tx} \approx \gamma T_p$. This is a good approximation for linear FM chirp pulses with a high time-bandwidth product.

The transmitted RF signal is

$$v_{tx}(t) = p(t) \, \exp\left(j2\pi f_c t\right) \tag{2.23}$$

where $f_c$ is the centre frequency. For a stepped-frequency system which transmits $n$ frequency steps the carrier frequency of pulse $i$, where $i = 0, \dots, (n-1)$, is given by

$$f_i = f_c' + \delta f_i \tag{2.24}$$

where $f_c'$ is the centre frequency of the reconstructed wide-bandwidth chirp pulse, and $\delta f_i$ is the frequency shift associated with pulse $i$, given by

$$\delta f_i = \left(i + \frac{1-n}{2}\right) \Delta f \tag{2.25}$$

The transmitted pulses belonging to one burst can thus be described by

$$v_{tx}(t, i) = p(t) \, \exp\left(j2\pi f_i t\right) \tag{2.26}$$

The received signal from a single scatterer at a distance $r_t$ is a time-delayed version of the transmitted signal, given by

$$v_{rx}(t, i) = v_{tx}\left(t - t_0, i\right)$$

where $t_0 = \frac{2r_t}{c}$. After coherent demodulation, the signal at baseband is given by

$$
\begin{aligned}
v_{bb}(t, i) &= v_{rx}(t, i) \, \exp\left(-j2\pi f_i t\right) && \text{(2.27)} \\
&= v_{tx}\left(t - t_0, i\right) \, \exp\left(-j2\pi f_i t\right) && \text{(2.28)} \\
&= p\left(t - t_0\right) \, \exp\left(-j2\pi f_i t_0\right) && \text{(2.29)}
\end{aligned}
$$

This signal is then sampled at a complex sampling rate of $f_{ad} > B_{tx}$.

It is now proposed to reconstruct a wide-bandwidth chirp pulse in the time-domain by coherently adding several narrow-bandwidth chirp pulses, each obtained by separate transmission and reception of pulses of bandwidth $B_{tx}$, but stepped in frequency by appropriate choice of the carrier frequency. If the frequency step $\Delta f = B_{tx}$, then the desired reconstruction is possible; otherwise, there will be gaps or overlaps in the reconstructed wide-bandwidth chirp waveform. The required signal processing steps for performing the reconstruction are described below.
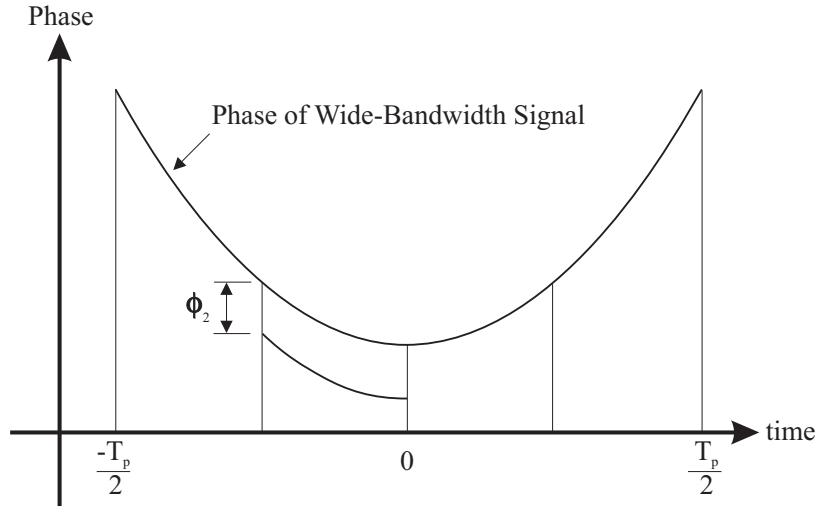
*Figure 2.5:* *Addition of phase-correcting term to narrow-bandwidth signals.*

## Upsampling

Unless the narrow-bandwidth pulses are already oversampled at a rate $f_{ad} >$ $nB_{tx}$, they must be upsampled before applying the frequency-shift described below, in order to avoid aliasing. Usually the time-domain signals have to be upsampled by a factor of $n$, where $n$ is the number of pulses used to synthesise the wide bandwidth. The upsampling operation can be achieved by applying an FFT, zero-padding the spectrum and then applying an IFFT.

## Frequency-shift

The amount of frequency-shift associated with pulse $i$ is given by $\delta f_i$, which can be achieved in the time-domain by multiplication by the factor $\exp(j2\pi \, \delta f_i \, t)$. The frequency-shifted pulses are thus described by

$$v'_{bb}(t, i) = v_{bb}(t, i) \, \exp(j2\pi \, \delta f_i \, t) \qquad (2.30)$$

## Phase correction

The need to add a phase-correcting term to each pulse can be explained with the aid of Figure 2.5. In the figure, the phase versus time plot of the wide-bandwidth signal and of the second narrow-bandwidth signal (from a burst of

35

four such signals) is shown. The narrow-bandwidth signal has already been shifted in frequency and time, but a phase-correcting term given by

$$\phi_i = \exp\left[j\pi\gamma T_p^2 \left(i + \frac{1-n}{2}\right)^2\right] \tag{2.31}$$

has to be applied in order to avoid phase discontinuities in the wide-bandwidth signal. This phase term may be applied to the narrow-bandwidth signals before they are upsampled, thus requiring fewer multiplications and leading to a faster implementation of the procedure.

**Time-shift**

Before adding the narrow-bandwidth pulses together, they have to be shifted in the time domain. The necessary time-shift is given by

$$\delta t_i = \left(i + \frac{1-n}{2}\right) T_p \tag{2.32}$$

Since the signals are sampled at the A/D rate $f'_{ad}$ (after they have been upsampled), the time-shift given in terms of number of samples is

$$m_i = \delta t_i \, f'_{ad} \tag{2.33}$$

Ideally $m_i$ should be an integer, because fractional values would require the narrow-bandwidth pulses to be interpolated. This would be computationally inefficient and might lead to errors in the reconstructed wide-bandwidth signal. This requirement can be achieved by adjusting either the pulse length $T_p$ or the A/D sampling rate $f'_{ad}$.

## 2.6.3 Combining narrow-bandwidth chirps

The reconstructed wide-bandwidth signal $v'(t)$ is obtained by coherently adding the processed narrow-bandwidth signals. Observing that $\Delta f = B_{tx} = \gamma T_p$, one obtains the following expression for $v'(t)$ after simplification:

$$
\begin{aligned}
v'(t) &= \sum_{i=0}^{n-1} v'_{bb}(t - \delta t_i, i)\, \phi_i \\
&= \sum_{i=0}^{n-1} A \operatorname{rect}\left(\frac{t - \frac{2r_t}{c} - \delta t_i}{T_p}\right) \exp\left[j\pi\gamma\left(t - \frac{2r_t}{c} - \delta t_i\right)^2\right]
\end{aligned} \tag{2.34}
$$

$$\cdot \exp\left[j2\pi f_i\left(t - \frac{2r_t}{c} - \delta t_i\right)\right]\exp\left[-j2\pi f_i\left(t - \delta t_i\right)\right]$$

$$\cdot \exp\left[j2\pi\,\delta f_i\,(t - \delta t_i)\right]\exp\left[j\pi\gamma T_p^2\left(i + \frac{1-n}{2}\right)^2\right] \qquad (2.35)$$

$$= A\exp\left[j\pi\gamma\left(t - \frac{2r_t}{c}\right)^2\right]\sum_{i=0}^{n-1}\mathrm{rect}\left(\frac{t - \frac{2r_t}{c} - \delta t_i}{T_p}\right) \qquad (2.36)$$

$$= A\exp\left[j\pi\gamma\left(t - \frac{2r_t}{c}\right)^2\right]\mathrm{rect}\left(\frac{t - \frac{2r_t}{c}}{nT_p}\right) \qquad (2.37)$$

This is simply the expression of a wide-bandwidth chirp pulse with a bandwidth of $B_t \approx \gamma T_p' = nB_{tx}$, with $T_p' = nT_p$. Range compression may be achieved by convolving this signal with a matched filter, which is given by the time-reversed conjugate of the wide-bandwidth pulse.

## 2.6.4 Simulation results

A stepped-frequency radar system was simulated to validate and illustrate the method described above. Table 2.2 summarises the relevant parameters used. These parameters were chosen to correspond with the VHF-band SASAR system, which has a centre frequency $f_c' = 141\,\mathrm{MHz}$ and transmits linear FM chirps with a pulse length of $T_p = 10\,\mu\mathrm{s}$ (among others) and a bandwidth of $B_{tx} = 12\,\mathrm{MHz}$ sampled at $f_{ad} = 24\,\mathrm{MHz}$. In the simulation, four pulses were transmitted, each with a bandwidth of $12\,\mathrm{MHz}$, spaced at $12\,\mathrm{MHz}$ intervals. The total radar bandwidth is given by $B_t = nB_{tx} = 48\,\mathrm{MHz}$, and therefore the expected resolution is $2.78\,\mathrm{m}$, which includes the mainlobe broadening factor $K_r = 0.89$ associated with a rectangular weighting window. (Note that the current SASAR system cannot achieve such a bandwidth due to antenna and receiver limitations.)

| First centre frequency | $f_0$ | $123\,\mathrm{MHz}$ |
|---|---|---|
| Frequency step size | $\Delta f$ | $12\,\mathrm{MHz}$ |
| Number of steps | $n$ | 4 |
| Bandwidth of narrowband chirp pulses | $B_{tx}$ | $12\,\mathrm{MHz}$ |
| ADC (complex) sample rate | $f_{ad}$ | $24\,\mathrm{MHz}$ |
| Pulse length of narrowband chirp pulses | $T_p$ | $10\,\mu\mathrm{s}$ |
| Total radar bandwidth | $B_t$ | $48\,\mathrm{MHz}$ |

**Table 2.2:** *Stepped-frequency simulation parameters of time-domain method.*
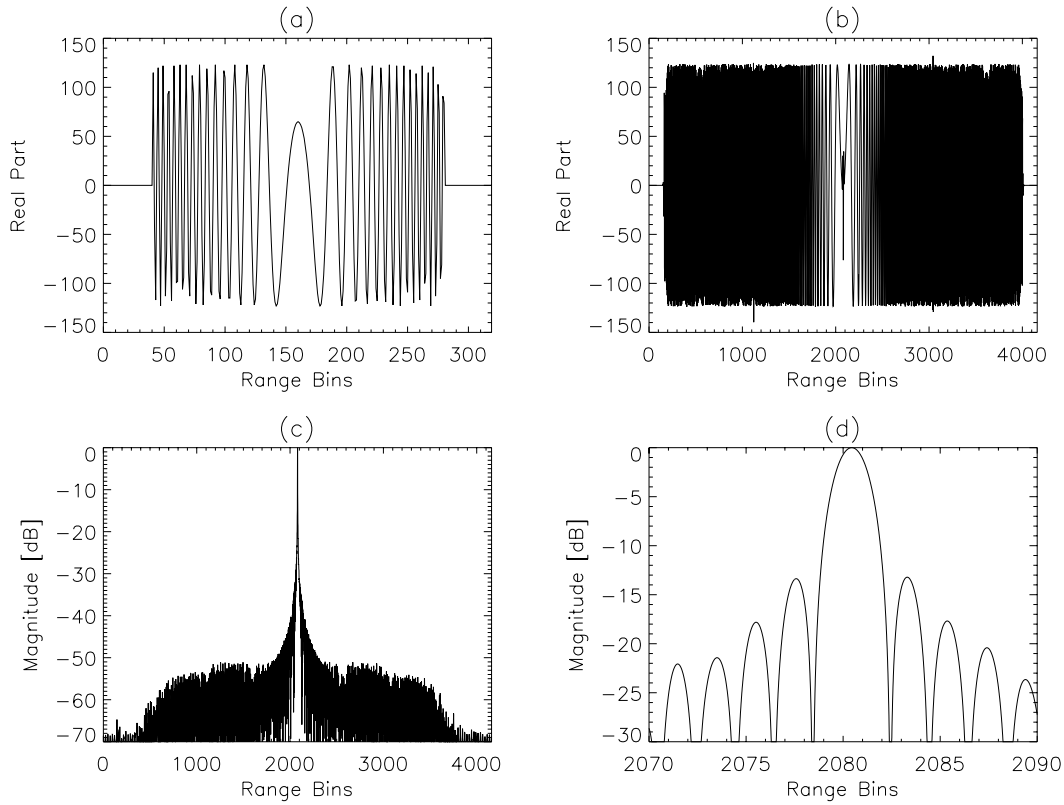
**Figure 2.6:** *Simulation results of time-domain method to combine stepped-frequency waveforms.*

The results of the simulation are summarised in Figure 2.6, which displays the following graphs:

(a) The real return of the first narrowband chirp pulse.

(b) The real part of the reconstructed wideband chirp waveform, which has a bandwidth of $B_t = 48\,\text{MHz}$.

(c) A dB plot of the entire range profile, after the signal shown in (b) has been range compressed.

(d) A zoomed-in portion of the range profile, after the complex data has been upsampled by a factor of 100.

The peak sidelobe levels have been measured to be $-13.2\,\text{dB}$ below the main-lobe, which agrees with the expected theoretical value when using a rectangular

window function. The integrated sidelobe ratio, measured across the range extent shown in Figure 2.6 (d), was calculated to be $-10.6\,\text{dB}$, and the measured $3\,\text{dB}$ mainlobe width was $2.79\,\text{m}$, which also agrees with the expected value. This simulation illustrates that the time-domain method can be used to combine stepped-frequency waveforms without introducing repeated target artefacts in the high-resolution range profile.

## 2.6.5 Results using E-SAR data

In order to verify the stepped-frequency time-domain approach on real data, the range frequency spectrum of a raw German E-SAR C-band image of Lechfeld, Germany, was divided into five parts, each part approximating the frequency spectrum of a fictitious narrow-bandwidth pulse. It is only an approximation, since the rectangular window, which was used to split the wide-bandwidth frequency spectrum, introduces ringing in the time domain. Nevertheless, an inverse FFT was then applied to the narrow-bandwidth spectra, effectively yielding the time-domain return of five narrow-bandwidth pulses. Table 2.3 shows the relevant parameters of the original E-SAR image. After dividing the range spectrum into five parts, the centre frequency of the first pulse became $f_0 = 5.26\,\text{GHz}$, the bandwidth of each narrowband pulse became $B_{tx} = 20\,\text{MHz}$, the sampling rate was reduced to $20\,\text{MHz}$ and the pulse lengths were reduced to $1\,\mu\text{s}$.

Figure 2.7 shows the result which was obtained after processing the image with the chirp scaling algorithm using only *one* of the five frequency steps. After combining all five frequency steps using the time-domain method, the image shown in Figure 2.8 was obtained. The improvement in range resolution is clearly visible. No visible difference could be detected between this image and the original wideband image, except for the fact that targets at near and far range became fainter. This is the result of information having been shifted out of the range extent when the time-shift was performed. According to Equation 2.33, 200 range

| Centre frequency | $f_c$ | $5.3\,\text{GHz}$ |
|---|---|---|
| Total radar bandwidth | $B_t$ | $100\,\text{MHz}$ |
| A/D (complex) sample rate | $f_{ad}$ | $100\,\text{MHz}$ |
| Pulse length | $T_p$ | $5\,\mu\text{s}$ |

**Table 2.3:** *Parameters of E-SAR image.*
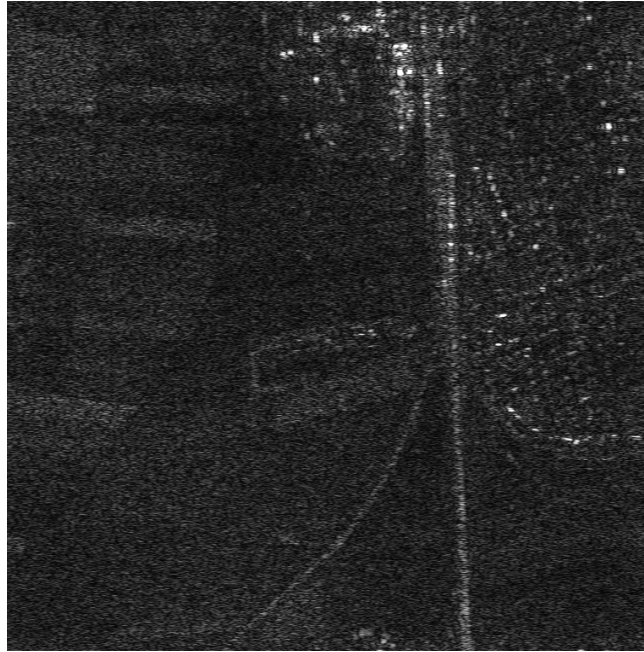
**Figure 2.7:** *Single-look E-SAR image of Lechfeld, Germany, obtained using only one frequency step, with $B_{tx} = 20\,MHz$. The flight path is along the vertical axis, with near range towards the left of the image.*
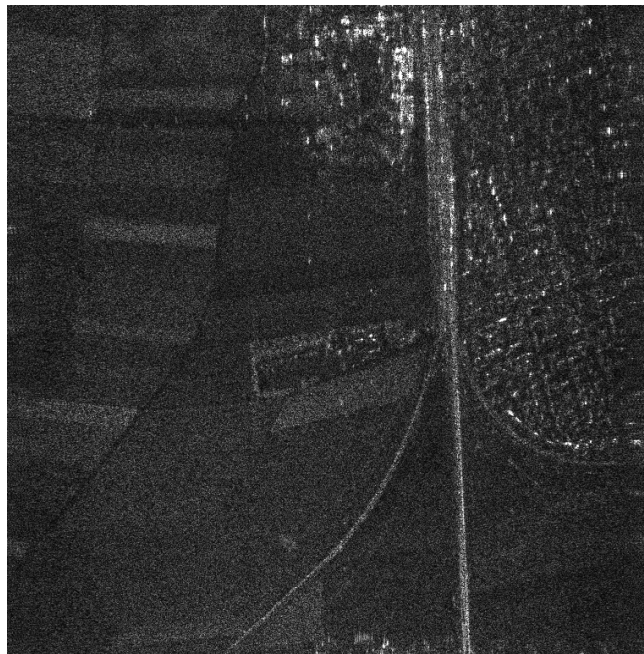


**Figure 2.8:** *Single-look E-SAR image obtained using five frequency steps, with $B_t = 100\,MHz$.*

bins were shifted out of the range extent at both ends of the swath, which is a significant number for this image, which is only 760 range bins wide.

### 2.6.6   SAR processing using time-domain method

The time-domain method of combining stepped-frequency waveforms has a few disadvantages, one of them being that information is shifted out of the range extent as in the example described above. Furthermore, in order to reconstruct the wide-bandwidth chirp signal perfectly, the spectra of the individual frequency steps may not overlap or contain gaps. Most importantly, however, this method is inefficient because of the upsampling requirement described in Section 2.6.2, and is therefore not suited for SAR processing applications. These considerations have led to the development of a frequency-domain method described in Chapter 3, which does not have these drawbacks.

## 2.7   Review and Summary

This chapter has given a brief introduction to side-looking strip-map SAR. The concept of range resolution has been described, and there has been discussion of how it applies to short pulse systems, pulse compression systems and stepped-frequency systems. The implications of a stepped-frequency system, such as the increase in PRF, velocity compensation and motion compensation have been discussed.

The IFFT method of processing stepped-frequency data has been applied on simulated data and on real stepped-frequency data of aircraft. Experience gained from applying the IFFT method has shown it to be unsuitable for processing SAR images, mainly because target energy spills over into consecutive coarse range bins as a result of the matched filter operation, causing "ghost targets" in the range profile. The time-domain approach is also not suitable for SAR applications, mainly because it is very inefficient to upsample the narrowband pulses in the time-domain.

Instead of recombining the stepped-frequency waveforms in the time-domain, they can also be recombined in the frequency domain. Essentially the aim is to reconstruct a larger portion of the target's reflectivity spectrum $Z(f)$ by com-

bining the individual spectra of the transmitted narrow-bandwidth pulses in the frequency domain. The target reflectivity function $\zeta(t)$ represents the target's reflection properties at range $r$ mapped into the time domain, where $t = \frac{2r}{c}$. This method is described in Chapter 3. It will be shown that the frequency-domain approach efficiently uses all of the information contained in the stepped-frequency data to produce reliable, high-resolution range profiles, which do not contain any repeating artefacts or "ghost targets".

The IFFT method can be seen to be a limiting case of the spectrum reconstruction method. Instead of obtaining the narrowband spectrum for every transmitted pulse and then shifting and coherently adding all the subspectra to reconstruct the target's reflectivity spectrum, the IFFT method only operates on the coarse range bin containing the largest magnitude return. This value is regarded as a sample of the target's reflectivity spectrum. Both methods apply an inverse FFT to their respective target reflectivity spectrum to obtain a high-resolution time-domain range profile. The IFFT method only works well for targets which are completely contained in one coarse range bin, but it is unsuitable for extended targets or SAR applications.

The time-domain technique is also similar to the frequency-domain technique. Both methods require the narrowband pulses to be shifted in frequency, after which they are coherently added. However, the time-domain pulses need to be upsampled before applying the frequency shift, making this method computationally intensive and inefficient.

# Chapter 3

# Reconstruction of Target Reflectivity Spectrum

## 3.1 Introduction

The concept of reconstructing a target's reflectivity spectrum by coherently adding all the narrowband spectra in the frequency domain has already been introduced in the previous chapter. This chapter describes this approach of processing stepped-frequency data in more detail. Section 3.2 gives the mathematical background, and Sections 3.3 and 3.4 describe the steps involved when reconstructing the target's reflectivity spectrum. Section 3.5 describes the design of the compression filter, which flattens the spectral "ripples" at the subspectra boundaries, that would otherwise produce repeating artefacts in the time-domain.

This technique involves the reconstruction of a wider portion of the target's reflectivity spectrum by combining the individual spectra of the transmitted narrow-bandwidth pulses in the frequency domain. The principle of enhancing the range resolution by recovering a larger band of the reflectivity's spectrum was introduced by Prati and Rocca (Prati and Rocca 1992), but that was in the context of coherently combining SAR images taken from different observation angles. This thesis shows how the technique may be applied to the concept of stepped-frequency processing.

The CARABAS-II system, which operates in the 20–90 MHz band, also em-

ploys stepped-frequency processing to obtain a bandwidth of 70 MHz (Ulander 1998), (Ulander and Frölind 1999). The CARABAS-II processing method has been independently developed but is very similar to the method described in this chapter, since it also involves the coherent addition of complex narrowband subspectra to reconstruct the wide-bandwidth spectrum. To the best of the candidate's knowledge, the concept of describing this technique in terms of the target reflectivity profile is novel.

The technique is verified and illustrated in Section 3.6 by implementing it on simulated data. It is shown how frequencies may be skipped in order to avoid spectral regions that would be corrupted by RFI. It is also shown that both the frequency step sizes and the individual transmit bandwidths within a burst of pulses can be varied. This offers more flexibility in notching out specific regions of the spectrum that contain dominant interferers. Section 3.7 describes the results that have been obtained when applying this technique on the real stepped-frequency aircraft data described in the previous chapter.

The methods described in this chapter adopt the start-stop approximation, which means that the radar-target range remains constant during the transmission of one burst of frequencies. The candidate is indebted to Andrew Wilkinson (RRSG, UCT) for the mathematical modelling and description of this technique (Wilkinson 1996), reviewed in Sections 3.2–3.5. Only the coding, implementation and characterization of the performance of this method are the candidate's own work. Some of the material in this chapter has been published in the Proceedings of COMSIG'98 (Wilkinson, Lord and Inggs 1998).

## 3.2   Waveform Modelling

For reasons of flow and ease of reading, the first few equations of Section 2.6.2 are repeated here. Thus, as already mentioned, a linear FM chirp waveform at baseband can be described by

$$p(t) = A \operatorname{rect}\left(\frac{t}{T_p}\right) e^{j\pi\gamma t^2} \qquad (3.1)$$

where $A$ is the amplitude, $T_p$ the pulse length and $\gamma$ the chirp rate. The spectrum is approximately rectangular with bandwidth $B_{tx} \approx \gamma T_p$. This is a good approximation for linear FM chirp pulses with a high time-bandwidth product.

The transmitted RF signal is modelled by

$$v_{tx}(t) = p(t)\, e^{j2\pi f_c t} \tag{3.2}$$

where $f_c$ is the centre frequency. The received signal is given by the convolution of the scene reflectivity function $\zeta(t)$ and the transmitted pulse:

$$
\begin{aligned}
v_{rx}(t) &= \zeta(t) \circledast v_{tx}(t) && (3.3)\\
&= \int \zeta(t-\tau)\, v_{tx}(\tau)\, d\tau && (3.4)
\end{aligned}
$$

After coherent demodulation, the signal at baseband is given by

$$
\begin{aligned}
v_{bb}(t) &= v_{rx}(t)\, e^{-j2\pi f_c t} && (3.5)\\
&= \int \zeta(t-\tau)\, p(\tau)\, e^{j2\pi f_c \tau}\, d\tau\, e^{-j2\pi f_c t} && (3.6)\\
&= \int \zeta(t-\tau)\, e^{-j2\pi f_c (t-\tau)}\, p(\tau)\, d\tau && (3.7)\\
&= \left[ \zeta(t)\, e^{-j2\pi f_c t} \right] \circledast p(t) && (3.8)
\end{aligned}
$$

All linear receiver distortions (for example front-end filters, antenna responses, etc.) can be included in the signal model by introducing an equivalent baseband filter $x(t)$. Receiver noise is modelled by an equivalent referred RF noise signal $n(t)$ with spectrum $N(f)$. The signal as it appears at the input to the receiver analogue to digital converter is therefore

$$v_{bb}(t) = \left[ \zeta(t)\, e^{-j2\pi f_c t} + n(t) e^{-j2\pi f_c t} \right] \circledast p(t) \circledast x(t) \tag{3.9}$$

This signal is sampled at a complex sampling rate of $f_{ad} > B_{tx}$. In the frequency domain the expression for the baseband signal is

$$V_{bb}(f) = \left[ Z\,(f + f_c) + N\,(f + f_c) \right] P(f)\, X(f) \tag{3.10}$$

Thus, the spectral representation of the received signal can be viewed as a windowed version of the target's reflectivity spectrum $Z\,(f)$, where the position of the window is determined by the centre frequency, and the shape is determined by the spectrum of the transmitted pulse and the receiver distortions.

Range compression is usually achieved by convolving the received signal with a matched filter, which is given by the time-reversed conjugate of the transmitted pulse, and which maximises the instantaneous signal to noise ratio. More generally, a compression filter $H(f)$ can be designed as a trade-off between compressing

the received signal into a narrow pulse (with desirable low sidelobe properties) and improving the instantaneous signal to noise ratio. In the frequency domain the range-compression operation is given by

$$
\begin{align}
V(f) &= V_{bb}(f)\,H(f) \tag{3.11}\\
&= [Z(f+f_c) + N\,(f+f_c)]\,P(f)\,X(f)\,H(f) \tag{3.12}\\
&= [Z(f+f_c) + N\,(f+f_c)]\,W(f) \tag{3.13}
\end{align}
$$

where $W(f) = P(f)\,X(f)\,H(f)$. The time-domain signal is

$$
v(t) = \left[\zeta(t)\,e^{-j2\pi f_c t} + n(t)e^{-j2\pi f_c t}\right] \circledast w(t) \tag{3.14}
$$

The phase of $H(f)$ is always chosen to cancel the phase of $P(f)\,X(f)$, thus $\arg(H(f)) = \arg(P^*(f)\,X^*(f))$. The amplitude of $H(f)$ is chosen according to the desired time-domain impulse response. For example, if it is assumed that $P(f)\,X(f)$ is strictly bandlimited to $B_{tx}$, which is a good approximation for linear FM chirp pulses with a high time-bandwidth product $(> 100)$, and if $|P(f)\,X(f)\,H(f)| = 1$ across that bandwidth, then

$$
V(f) = [Z(f+f_c) + N\,(f+f_c)]\,\mathrm{rect}\left(\frac{f}{B_{tx}}\right) \tag{3.15}
$$

This is simply a bandlimited, shifted version of the target reflectivity spectrum. Inverse transforming, the time-domain waveform is

$$
v(t) = \left[\zeta(t)\,e^{-j2\pi f_c t} + n(t)e^{-j2\pi f_c t}\right] \circledast \mathrm{Sa}\left(\pi B_{tx} t\right) \cdot B_{tx} \tag{3.16}
$$

where $\mathrm{Sa}(x) = \frac{\sin(x)}{x}$. Thus the time-domain impulse response is a sinc function with a $3\,\mathrm{dB}$ resolution of $\delta t = \frac{1}{B_{tx}}$. The sidelobe response can be reduced by introducing an appropriate frequency-domain window function, at the expense of widening the mainlobe.

## 3.3   Coherent Addition of Subspectra

We now reconstruct a wider portion of the target's reflectivity spectrum by piecing together several adjacent subportions of the spectrum, each obtained by separate transmission and reception of pulses of bandwidth $B_{tx}$, but stepped appropriately in frequency by appropriate choice of the carrier frequency. If the

frequency step $\Delta f$ satisfies the inequality $\Delta f \leq B_{tx}$, then the desired reconstruction is possible. Assuming a sequence of $n$ adjacent windows (indexed by $i = 0, \ldots, n-1$), a broad region of the frequency spectrum can be reconstructed, symmetrical about zero, by shifting each spectrum at baseband by an amount

$$\delta f_i = \left( i + \frac{1-n}{2} \right) \Delta f \tag{3.17}$$

in the positive direction, and adding together the shifted versions. For an array with $M$ discrete bins sampled at a complex rate of $f_{ad}$, the frequency shift in terms of number of samples is

$$m_i = \frac{M}{f_{ad}} \delta f_i \tag{3.18}$$

Ideally $m_i$ should be an integer, because fractional values would otherwise require the subspectra to be interpolated. This would be computationally inefficient and might lead to errors in the reconstructed spectrum.

If we assume a linear superposition of the shifted subspectra, the reconstructed spectrum as shown in Figure 3.1 is

$$V'(f) = \sum_{i=0}^{n-1} V_i(f - \delta f_i) \tag{3.19}$$

$$= \sum_{i=0}^{n-1} \left( [Z(f + f_i - \delta f_i) + N(f + f_i - \delta f_i)] \, W(f - \delta f_i) \right) \tag{3.20}$$

where $f_i$ is the carrier frequency of pulse $i$ and $V_i(f)$ is the frequency spectrum at baseband of pulse $i$. The expression $(f_i - \delta f_i)$ can, by substitution and simplification, be seen to be the centre frequency $f'_c$ of the entire reconstructed spectrum:

$$f'_c = f_i - \delta f_i \tag{3.21}$$

$$= (f_0 + i \, \Delta f) - \left( i + \frac{1-n}{2} \right) \Delta f \tag{3.22}$$

$$= f_0 + \left( \frac{n-1}{2} \right) \Delta f \tag{3.23}$$

$$= \frac{f_0 + f_{n-1}}{2} \tag{3.24}$$

The reconstructed spectrum can thus be expressed as

$$V'(f) = [Z(f + f'_c) + N(f + f'_c)] \sum_{i=0}^{n-1} W(f - \delta f_i) \tag{3.25}$$

$$= [Z(f + f'_c) + N(f + f'_c)] \, W'(f) \tag{3.26}$$
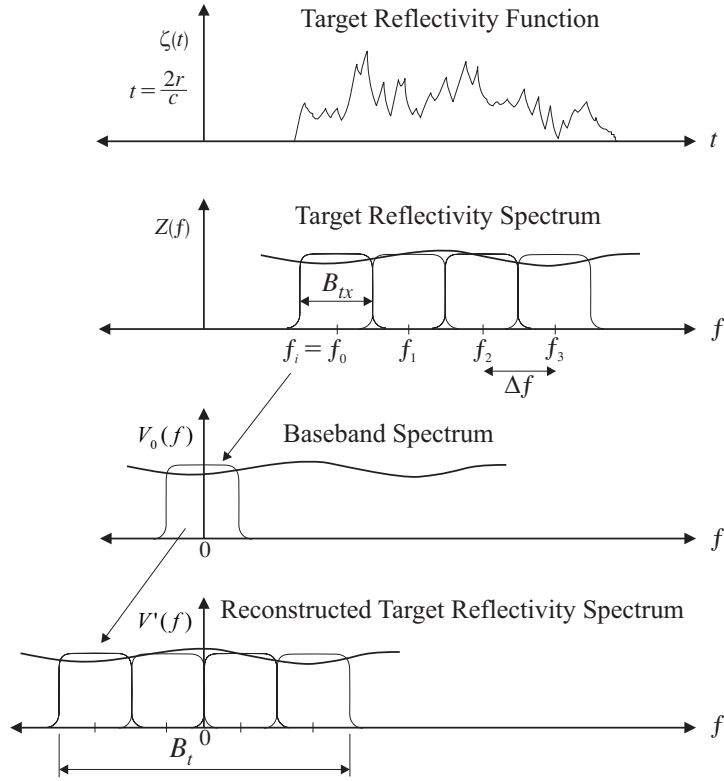
**Figure 3.1:** *Reconstruction of target reflectivity spectrum for $n = 4$ transmitted pulses, each with carrier frequency $f_i$ and bandwidth $B_{tx}$.*

where

$$W'(f) = \sum_{i=0}^{n-1} W\left(f - \delta f_i\right) \tag{3.27}$$

The time-domain signal can then be obtained by inverse transforming to yield

$$v'(t) = \left[\zeta(t)\, e^{-j2\pi f'_c t} + n(t) e^{-j2\pi f'_c t}\right] \circledast w'(t) \tag{3.28}$$

If, for example, we consider the case where the frequency step $\Delta f = B_{tx}$, then the total bandwidth of the reconstructed spectrum is $B_t = n B_{tx}$, as is shown in Figure 3.1. If the combined compression filter

$$H'(f) = \sum_{i=0}^{n-1} H(f - \delta f_i) \tag{3.29}$$

is chosen such that $W'(f) = \mathrm{rect}\left(\frac{f}{B_t}\right)$, then the time-domain signal is

$$v'(t) = \left[\zeta(t)\, e^{-j2\pi f'_c t} + n(t) e^{-j2\pi f'_c t}\right] \circledast \mathrm{Sa}(\pi B_t t) \cdot B_t \tag{3.30}$$

and the 3 dB resolution is $\delta t' = \frac{1}{B_t}$, which is a factor of $n$ better than would have been achieved without reconstruction.

## 3.4   Practical Implementation on Sampled Data

The steps below describe how the spectral reconstruction can be performed with sampled data.

1. Choose a range of carrier frequencies $f_0, \ldots, f_{n-1}$ spaced at $\Delta f$ equal to, or marginally less than $B_{tx}$. If $\Delta f > B_{tx}$, the reconstructed spectrum will contain gaps and the resulting time-domain range profile will possess undesirable properties in the form of repeated artifacts spaced at multiples of $\frac{1}{\Delta f}$. However, even if there are gaps, an improvement in mainlobe resolution is still possible.

2. For each pulse obtain a sampled version of $v_{bb}(t)$, starting at $t_0$, with a complex sampling rate $f_s$, where $f_s > B_{tx}$.

3. Apply an FFT to each sampled pulse to obtain the individual subspectra of the target's reflectivity spectrum.

4. To obtain an optimal SNR, each subspectrum is matched-filtered prior to addition.

5. Since $v_{bb}(t)$ was sampled starting at $t_0$, each subspectrum has to be multiplied by the delay compensation factor $\exp(+j2\pi f t_0)$.

6. Shift the spectrum of pulse $i$ to its appropriate location, centred on $f = \left(i + \frac{1-n}{2}\right)\Delta f$.

7. Form the combined spectrum by coherently adding all of the individual subspectra.

8. Multiply the combined spectrum by the compression filter $H'(f)$ to obtain the discrete equivalent of $V'(f)$.

9. Multiply the entire spectrum by $\exp(-j2\pi f t_0)$. This re-shifts the time domain back to a sampled set beginning at $t = t_0$.

10. Apply a reshaping window, such as a Hanning or Taylor window, to suppress time-domain sidelobes at the expense of widening the mainlobe.

11. Inverse FFT the entire spectrum to obtain the high-resolution range profile.

## 3.5  Design of Compression Filter

The design of the compression filter $H'(f)$ is the most critical and important step in this method. It is important to consider the following points when constructing this filter:

- Obtain an estimate of the combined impulse response spectrum

$$
\begin{aligned}
U'(f) &= P'(f)\,X'(f) & (3.31) \\
&= \sum_{i=0}^{n-1} P(f - \delta f_i)\,X(f - \delta f_i) & (3.32)
\end{aligned}
$$

  For a real system, this should be achieved by measuring the return of a real, physical point target, for example a corner reflector, and recombining the individual spectra as described in the previous section. For such a target $Z(f) \approx \alpha$, where $\alpha$ is a constant, and therefore the combined baseband spectrum would be $V'_{bb}(f) \approx \alpha P'(f)\,X'(f)$. This method automatically provides an accurate description of the receiver distortions given by $X'(f)$.

- If it is impractical to obtain the return of a real, physical point target, a point target simulation may be used. It may be difficult, however, to predict the receiver distortions given by $X'(f)$. In the simulations that follow it has been assumed that $X'(f) = 1$. Note also that the position of the high-resolution profile will be relative to the target range chosen in the simulation and may therefore need to be shifted.

- If the sampled data has already been range-compressed by a matched filter to optimise the SNR, the subspectra used in constructing $H'(f)$ must also be range-compressed first with the same matched filter.

- When using a simulation it is important to ensure that there is no aliasing and that the individual subspectra are bandlimited. In the simulations that follow, this has been accomplished as follows:

  - First the return was oversampled by an arbitrary factor of 10 in order to reduce aliasing. If the time-bandwidth product is relatively high, the spectrum decays fairly quickly and a factor of 10 should be sufficient.

- After applying an FFT, the corresponding spectrum was multiplied by $\text{rect}\left(\frac{f}{B_{tx}}\right)$ to bandlimit the return to $B_{tx}$.

- To accomplish downsampling by a factor of 10, an appropriate number of zeroes was removed from the centre of the spectrum (i.e. the most positive and most negative frequency components).

- An IFFT transforms the now anti-aliased and bandlimited signal back into the time-domain.

- Having obtained an approximation of $U'(f)$, the filter $H'(f)$ is piecewise defined as follows (refer to Figure 3.2):

$$
H'(f) = \begin{cases}
\frac{U'^*(f)}{|U'(f_a)|} & \text{for} \quad f \leq f_a \\[2ex]
\frac{1}{U'(f)} & \text{for} \quad f_a < f < f_b \\[2ex]
\frac{U'^*(f)}{|U'(f_b)|} & \text{for} \quad f \geq f_b
\end{cases}
\tag{3.33}
$$

where the region $[f_a, f_b]$ includes the major part of the reconstructed spectrum, containing all the subspectra boundaries. This will effectively smoothen any ripples at the subspectra boundaries, yielding the desired time-domain impulse response. The first section and the last section of $H'(f)$, where the target spectrum decays to zero, is equated to the conjugate of $U'(f)$. This prevents the amplification of noise for a real system, while still cancelling the phase correctly. Note that $U'(f)$ has to be scaled appropriately
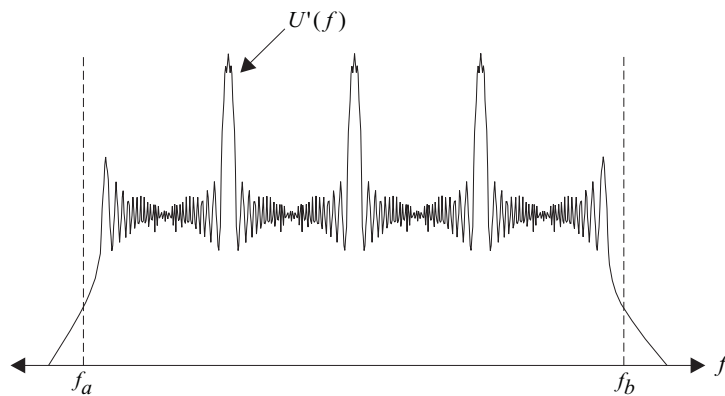


**Figure 3.2:** *Construction of compression filter $H'(f)$.*

so that no discontinuities arise at $H'(f_a)$ and $H'(f_b)$. An upper limitation for the function $U'(f)$ could be necessary in practical cases with low time-bandwidth products, in order to avoid a too strong amplification of the signal between the sub-bands, which would lead to a very large amplification of the noise component. Before combining the sub-bands, each sub-band may be tapered to arrive at an optimum solution when the range resolution and the sidelobe level are considered simultaneously.

## 3.6 Simulation Results

A stepped-frequency radar system was simulated in order to validate and illustrate the method described above. The simulated stepped-frequency data was obtained using the SAR simulation software written by Lengenfelder (Lengenfelder 1998b), whereas the processing of the simulated data was done entirely using software written in IDL by the candidate. Therefore the compression filter $H'(f)$ was not constructed with the same simulation software used to produce the stepped-frequency data. This procedure gave valuable insight into the importance of constructing the compression filter properly in order to flatten the reconstructed spectrum successfully.

The relevant parameters of the simulations are summarised in Table 3.1 and include the following:

- The first centre frequency $f_0$.

- The frequency step size $\Delta f$. Note that the simulations shown in Figures 3.6, 3.7 and 3.8 have varying frequency step sizes, whereas the other simulations have constant frequency step sizes.

- The number of frequency steps $n$.

- The bandwidth $B_{tx}$ of the narrowband chirp pulses. This bandwidth has been chosen to be 12 MHz for most simulations, since the VHF-band SASAR system has a transmit bandwidth of 12 MHz. The transmitted bandwidth of the simulation shown in Figure 3.8 varies for the different frequency steps.

| Fig. | $f_0$ [MHz] | $\Delta f$ [MHz] | $n$ | $B_{tx}$ [MHz] | $f'_c$ [MHz] | $B_t$ [MHz] | Overlap [MHz] |
|---|---|---|---|---|---|---|---|
| 3.3 | 123 | 12 | 4 | 12 | 141 | 48 | 0 |
| 3.4 | 124.8 | 10.8 | 4 | 12 | 141 | 44.4 | 1.2 |
| 3.5 | 119.4 | 14.4 | 4 | 12 | 141 | 55.2 | $-2.4$ |
| 3.6 | 124.8 | 21.6, 10.8 | 3 | 12 | 141 | 44.4 | $-9.6$, 1.2 |
| 3.7 | 123 | 9, 12.9, 14.1 | 4 | 12 | 141 | 48 | 3, $-0.9$, $-2.1$ |
| 3.8 | 123 | 9, 15, 15 | 4 | 12, 8, 14, 6 | 141 | 48 | 1, $-4$, $-5$ |
| 3.9 | 1363.75 | 1.875 | 55 | 3.636 | 1314 | 104.9 | 1.761 |
| 3.10 | 1363.75 | 1.875 | 55 | 3.636 | 1314 | 104.9 | 1.761 |

**Table 3.1:** *Stepped-frequency simulation parameters of spectrum reconstruction method.*

- The centre frequency $f'_c$ of the entire reconstructed spectrum, which is the midpoint between the two outer edges of the reconstructed spectrum. The centre frequency has been chosen to be 141 MHz for most simulations, since this is the centre frequency of the SASAR system.

- The total bandwidth $B_t$ of the reconstructed spectrum. It is calculated as the frequency range between the two outer edges of the entire reconstructed spectrum, regardless of any gaps that may occur in the reconstructed spectrum.

- The amount of spectral overlap between adjacent subspectra. Spectral *gaps* between adjacent subspectra are indicated with *negative* numbers. The overlap (or gap) between adjacent subspectra varies for the simulations shown in Figures 3.6, 3.7 and 3.8.

The simulation results are shown in Figures 3.3–3.8 on the following pages. Each figure displays the following graphs:

(a) The magnitude of the range-compressed target return, first frequency step. Where the target return has not been range-compressed (Figure 3.3 and Figure 3.4), the real part of the target return is shown.

(b) The spectrum obtained after coherent addition of the frequency-shifted subspectra.

(c) The spectrum of the compression filter $H'(f)$.

(d) The target reflectivity spectrum $V'(f)$ after applying the compression filter shown in (c).

(e) A dB plot of the high-resolution range profile, after inverse Fourier transforming the spectrum shown in (d). No window functions have been applied prior to inverse Fourier transforming.

(f) A zoomed-in section of the high-resolution range profile, in order to display the peak sidelobe level. For improved accuracy, the complex values were interpolated (using a Shannon interpolator) to one fiftieth of a sample to increase the accuracy when measuring the resolution (3 dB mainlobe width), *peak sidelobe ratios* (PSLR) and *integrated sidelobe ratios* (ISLR), with the integration having been performed over the range extent shown in this graph. The extent of the main peak region was found by defining the main peak as the region bounded by the points at which the gradient of the peak changed sign. The ISLR is defined here as the ratio of the integrated energy in the sidelobe region to the integrated energy contained in the main peak region. These results are summarised in Table 3.2.

Figure 3.3 shows a simulation where the target return signal has not been bandlimited, which is evident from the abrupt edges of the uncompressed chirp signal shown in graph (a). This implies that the spectrum of this signal does not decay to zero and is therefore aliased. However, the compression filter $H'(f)$ shown in graph (c) has been constructed with bandlimited signals and is therefore not properly matched to the reconstructed spectrum shown in graph (b). As a result, the target reflectivity spectrum shown in graph (d) contains ripples at the subspectra boundaries, even though there was no overlap between adjacent subspectra. These ripples increase the sidelobes and the integrated sidelobe ratio of the time-domain range profile (refer to Table 3.2). Graph (e) shows a dB plot of the entire high-resolution range profile, after inverse Fourier transforming the spectrum shown in graph (d), and graph (f) shows a zoomed-in section of this high-resolution range profile.
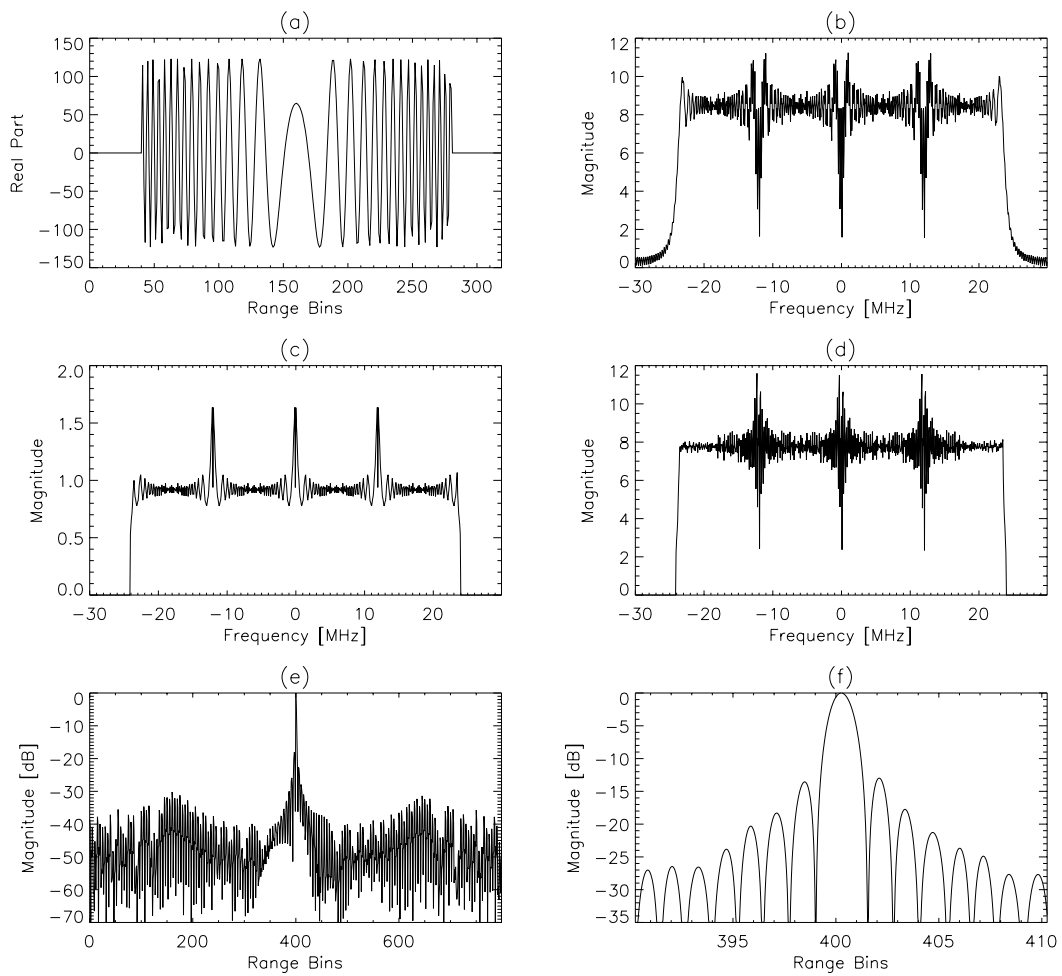
**Figure 3.3:** *Stepped-frequency simulation showing the effect when the returned target spectrum is not bandlimited.*
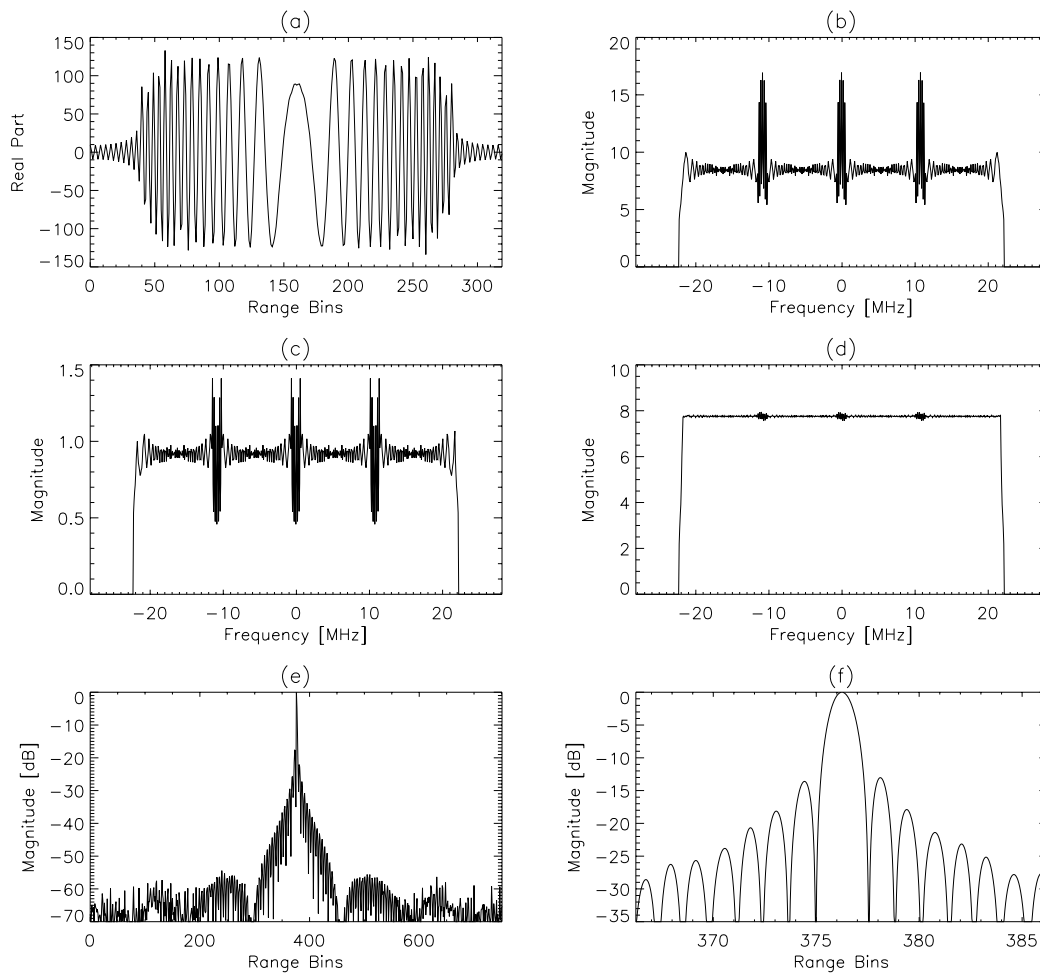
**Figure 3.4:** *Stepped-frequency simulation showing the effect when the returned target spectrum is bandlimited, and when there is an overlap between successive subspectra.*

Figure 3.4 shows a simulation where the return signal *has* been bandlimited as described in Section 3.5. Note that the chirp signal shown in graph (a) does not have abrupt edges. Furthermore, there is a subspectra overlap of 1.2 MHz. The "ripples" at the three subspectra boundaries are clearly visible in graph (b). After multiplication by the compression filter shown in graph (c), the target reflectivity spectrum in graph (d) is virtually flat, causing the sidelobes in graph (e) to decay faster when compared to Figure 3.3 (e). Graph (f) shows a zoomed-in section of the high-resolution range profile.

56
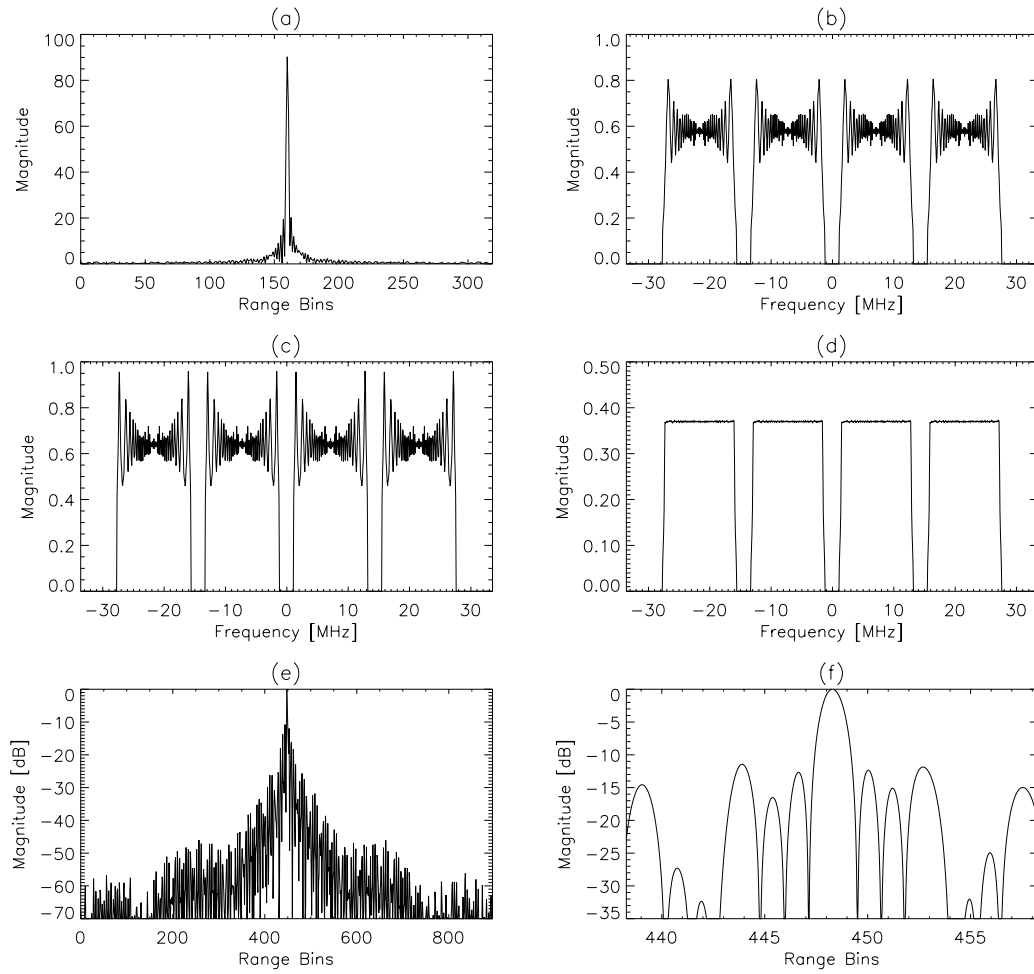
***Figure 3.5:*** *Stepped-frequency simulation showing the effect when there is a gap between successive subspectra.*

Figure 3.5 shows an example where the frequency step size is larger than the transmit bandwidth. In this example, there is a gap of 2.4 MHz between adjacent subspectra. The measured resolution improved from 3.08 m in the previous example (Figure 3.4) to 2.36 m. However, the peak sidelobe levels and integrated sidelobe levels both increased (see Table 3.2). This is also evident in graph (f), which shows a zoomed-in section of the high-resolution range profile.
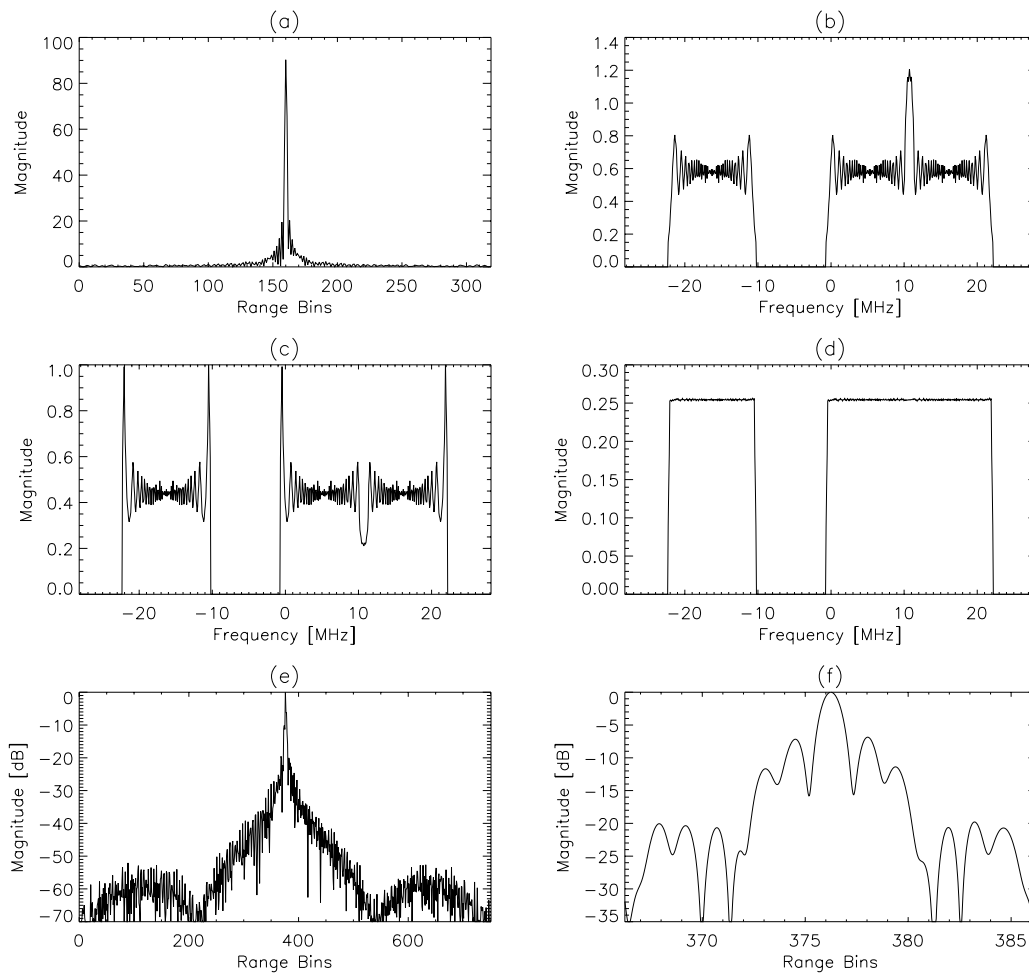
**Figure 3.6:** *Stepped-frequency simulation showing an example in which one frequency step has been omitted.*

Figure 3.6 shows the same simulation as Figure 3.4, except that the second frequency step has been omitted. The measured resolution, peak sidelobe levels and integrated sidelobe levels all deteriorated when compared to the simulation shown in Figure 3.4 (see Table 3.2). Omitting one or more frequency steps is one way to avoid receiving radio frequency interference in certain regions of the spectrum. However, this method is very wasteful of bandwidth, since the interfering frequency band is most probably much more narrow than the gap created by omitting a frequency step. Again the sidelobe levels increased significantly, which is shown in graph (f).
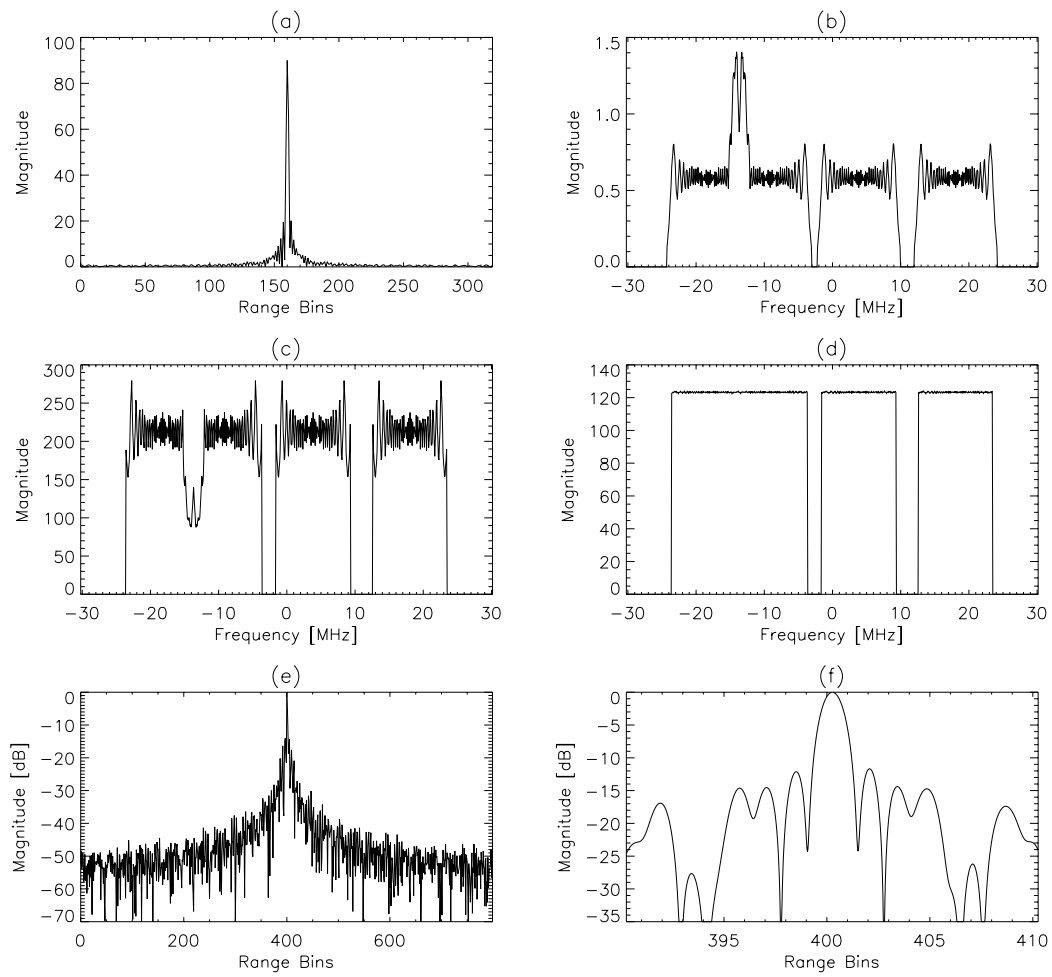
***Figure 3.7:*** *Stepped-frequency simulation showing an example in which different frequency step sizes have been used.*

Figure 3.7 shows an example in which the frequency step size varies from pulse to pulse, keeping the transmitted bandwidth constant. There is a spectral overlap of 3 MHz between the first two subspectra, and a spectral gap of 0.9 MHz and 2.1 MHz between the following subspectra. Varying the frequency step size allows for much greater control in terms of avoiding radio frequency interferers.
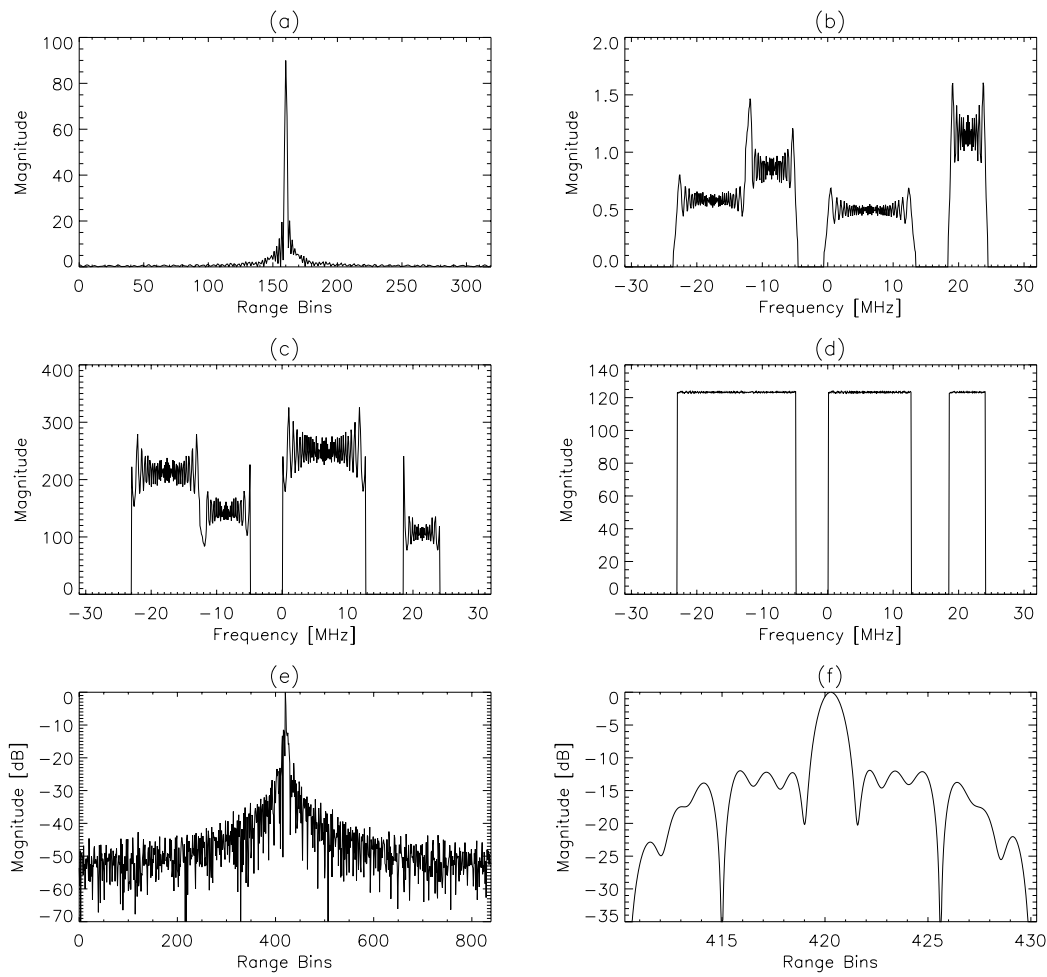
***Figure 3.8:*** *Stepped-frequency simulation showing an example in which different frequency step sizes and different transmit bandwidths have been used.*

Figure 3.8 shows an example in which the frequency step size varies from pulse to pulse, *and* the transmit bandwidth varies from pulse to pulse. There is a spectral overlap of 1 MHz between the first two subspectra, and a spectral gap of 4 MHz and 5 MHz between the following subspectra. This example illustrates the flexibility of this stepped-frequency processing method. However, it is important that the compression filter should be suitably matched to the data in order successfully to flatten the reconstructed spectrum. Being able to control the frequency step size and the transmit bandwidth from pulse to pulse offers the greatest flexibility in terms of notching out RFI.
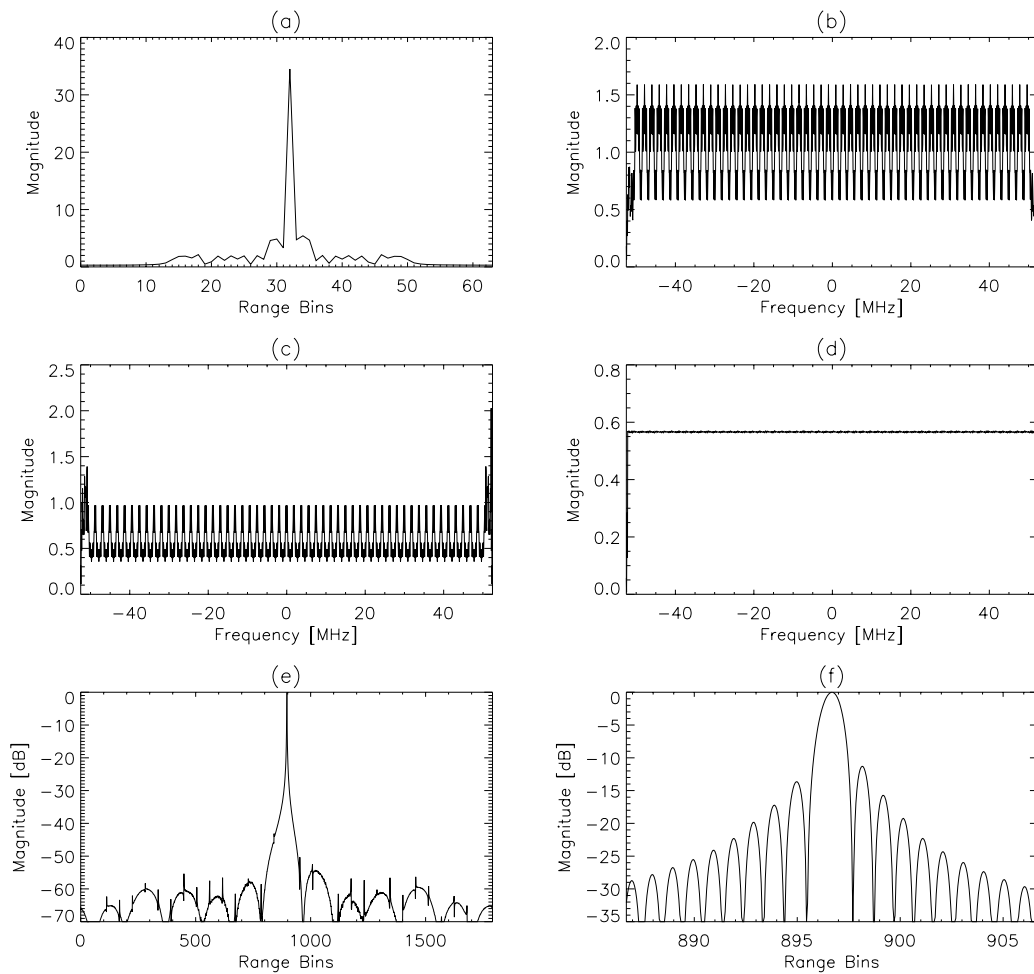
**Figure 3.9:** *Stepped-frequency simulation using parameters of real aircraft stepped-frequency data.*

Figure 3.9 shows a simulation using the stepped-frequency aircraft data parameters introduced in the previous chapter. This simulation has been included in order to demonstrate that this stepped-frequency processing method can, in theory, be applied to the stepped-frequency aircraft data. The results that have been obtained from the real aircraft data using this method are described in Section 3.7.
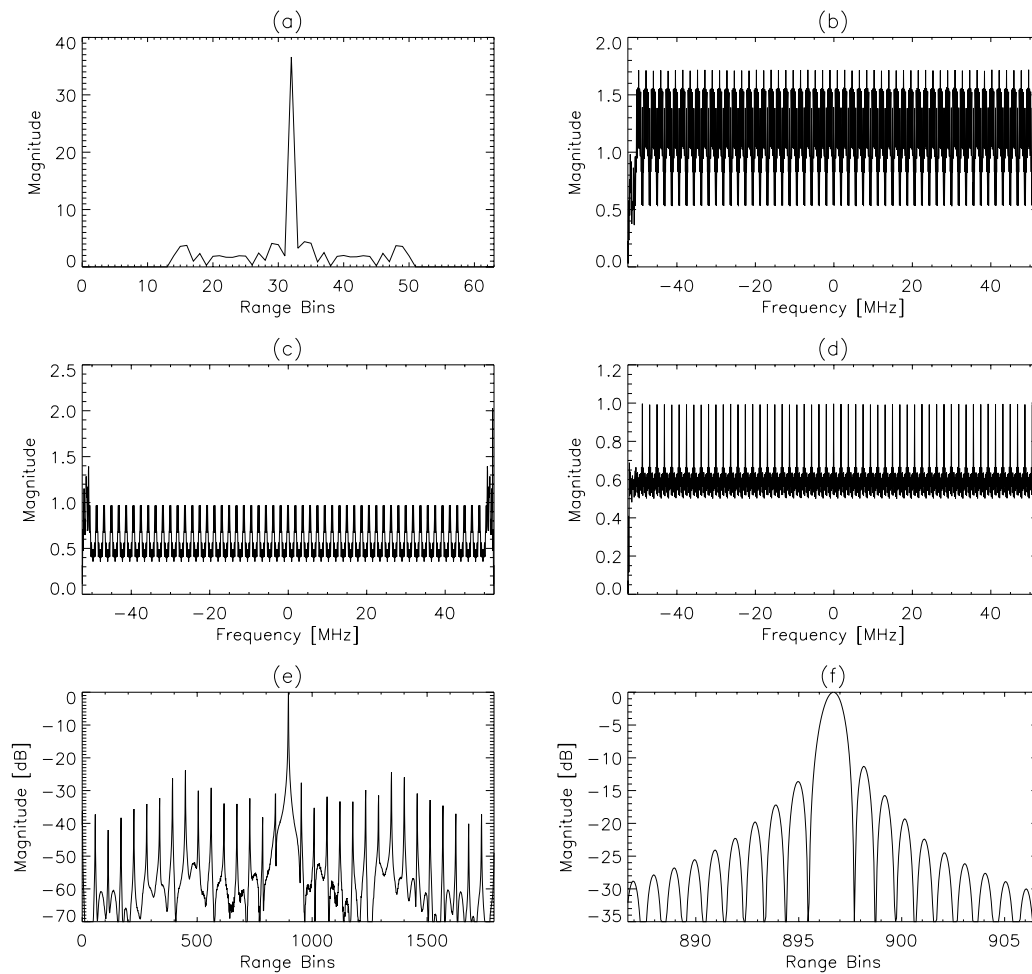
**Figure 3.10:** *Stepped-frequency simulation using parameters of real aircraft stepped-frequency data, without bandlimiting target returns.*

Figure 3.10 shows the same simulation as Figure 3.9. However, the signals have *not* been bandlimited. Although the peak sidelobe level and the integrated sidelobe level have remained virtually the same as when compared to Figure 3.9 (see Table 3.2), repeating artefacts of the target can be seen in graph (e). These artefacts are caused by the ripples in the reconstructed spectrum shown in graph (d).

| Fig. | Theoretical res. [m] | Measured res. [m] | | PSLR [dB] | | ISLR [dB] | |
|---|---|---|---|---|---|---|---|
| | | with gaps | gaps filled | with gaps | gaps filled | with gaps | gaps filled |
| 3.3 | 2.78 | 2.80 | | −13.2 | | −10.2 | |
| 3.4 | 3.01 | 3.08 | | −13.2 | | −10.3 | |
| 3.5 | 2.42 | 2.36 | 2.34 | −11.4 | −9.97 | −5.52 | −4.29 |
| 3.6 | 3.01 | 2.74 | 2.76 | −6.97 | −7.63 | −2.93 | −3.92 |
| 3.7 | 2.78 | 2.75 | 2.75 | −11.83 | −11.2 | −6.28 | −6.50 |
| 3.8 | 2.78 | 2.74 | 2.74 | −12.0 | −11.9 | −3.89 | −4.37 |
| 3.9 | 1.27 | 1.36 | | −13.1 | | −9.99 | |
| 3.10 | 1.27 | 1.36 | | −13.1 | | −10.0 | |

***Table 3.2:*** *Stepped-frequency simulation results of spectrum reconstruction method.*

Table 3.2 shows the theoretical resolution $\rho_r = \frac{cK_r}{2B_t}$ (with $K_r = 0.89$ for a rectangular window) of the range profiles, and summarises the measured resolution (3 dB mainlobe width), the peak sidelobe ratio (PSLR) and the integrated sidelobe ratio (ISLR). Since the reconstructed spectra of the simulations shown in Figures 3.5–3.8 all contain gaps, separate simulations have been carried out in which these gaps have been filled with a signal containing random phase and having a magnitude equal to the magnitude of the surrounding spectrum. Table 3.2 therefore also shows the measured resolution, PSLR and ISLR for those cases where the spectral gap has been filled, in order to investigate the effect of this filling process. The measured resolution has remained approximately the same, whereas the PSLR has deteriorated slightly (except for Figure 3.6), and the ISLR has improved slightly (except for Figure 3.5). Therefore the effect of filling the spectral gap with a signal with random phase and matching magnitude was not significant for the simulations shown here.

## 3.7 Results Obtained from Real Stepped-Frequency Data of Aircraft

Appendix B shows high-resolution synthetic range profiles of aircraft, which have been obtained using the IFFT method and the spectrum reconstruction method. These profiles have been upsampled (using a Shannon interpolator) by a factor of 20, in order to facilitate better comparison between the profiles obtained from the two methods. The two graphs in the top row show a zoomed-in portion of the entire high-resolution synthetic range profile, whereas the two graphs in the bottom row show a larger portion of the entire profile in order to expose "ghost targets" adjacent to the main target.

The profiles that have been obtained from both methods look very similar, although this aircraft database is not ideally suited for processing with the spectrum reconstruction method for the following reasons:

- The radial velocity is not accurately known. An estimate is calculated by interpolating the flight path described in the recorded data log file. This estimate has been used to apply a velocity correction to the datasets shown in Appendix B.

- The data contains a dc-offset. This offset has been removed by subtracting the mean from the entire burst.

- The data is not entirely bandlimited. This causes inaccurate compensation at the subspectra boundaries, which in turn causes "ghost" profiles in the time-domain range profile.

- The radar impulse response is not known. To obtain the compression filter for these datasets it has been assumed that the radar is ideal and that there are no non-linearities. Ideally one would like to have the real return from a point target or corner reflector, and then use that data to create the compression filter. An attempt has been made to create a compression filter using an aircraft dataset whose target profile resembles a point target, in the form of a sharp spike, but the results that have been obtained were not significantly better.

It is encouraging to see that the main profiles of both methods resemble each other significantly. However, due to the spill-over of target energy, the "ghost targets" seen in the profiles obtained from the IFFT method are significantly larger than those seen in the profiles obtained from the spectrum reconstruction method. This serves to confirm that the spectrum reconstruction method is the preferred choice when combining stepped-frequencies for SAR processing applications.

## 3.8 Conclusions

This chapter has described a frequency-domain method to combine stepped-frequency waveforms, which entails the reconstruction of the target's reflectivity spectrum. This method is fast, since only FFTs and phase multiplications are used, and it is flexible, because the frequency step size and the transmit bandwidth may vary from pulse to pulse within a burst of pulses. This flexibility offers the opportunity to avoid spectral regions that are highly contaminated with RFI, thereby reducing the likelihood of receiver saturation.

The spectrum reconstruction method efficiently uses all of the information contained in the stepped-frequency data to produce reliable, high-resolution range profiles that do not contain any repeating artefacts or "ghost targets", as long as great care is invested in the design of the compression filter which smooths the reconstructed spectrum. It has been demonstrated on simulated data and on real aircraft data.

# Chapter 4

# RFI Suppression for VHF/UHF SAR

## 4.1 Introduction

Radio frequency interference is a major problem for SAR systems operating at VHF/UHF-band, because the spectrum is already used extensively by other services such as television, mobile communications, radio and cellular phones. Experience with the SASAR system has shown that even in remote locations the interference power often exceeds receiver noise by many dB, becoming the limiting factor on system sensitivity and severely degrading the image quality. RFI suppression is also important when producing interferometric images at VHF/UHF-band. This is illustrated in Appendix C, which presents the first interferometric results of the SASAR system. These results have shown that in order to see fringe patterns in the interferogram, the RFI has to be suppressed.

The previous chapter described how spectral regions which are heavily contaminated with RFI can be avoided with the aid of stepped-frequency waveforms. However, since virtually the entire VHF/UHF spectrum is scattered with interference spikes, the above technique can only be applied to notch out the most dominant RFI sources. This chapter addresses other methods that may be used to suppress the remaining RFI in the received spectrum.

A brief literature review of the approaches to RFI suppression that have been used successfully in the SAR community is given in Section 4.2. Of these ap-

proaches, only the notch filter and the LMS adaptive filter have been implemented here, and these are described in Sections 4.5 and 4.6 respectively. It is beyond the scope of this thesis to implement all of the RFI suppression methods mentioned in Section 4.2. Results using both simulated data and real P-band and VHF-band data are shown and discussed for these two filters.

In addition to assessing the suitability of the notch filter and the LMS adaptive filter to suppress RFI in P-band and VHF-band images, the original contributions of this thesis also entail modifications to these filters in order to enhance their performance. These modifications include the use of a median filter in order to obtain an approximation to the signal spectrum envelope, which is then used by the notch filter to identify and remove interference spikes (see Section 4.5.2). Furthermore, the notch filter has been efficiently integrated with the range-compression stage of the range-Doppler SAR processor. Modifications to the LMS adaptive filter include sweeping the filter through each range line from both ends and then averaging the two outputs, sweeping the filter through each range line twice to allow better convergence of the weight vector, and zero-padding each range line to reduce edge effects (see Section 4.6.2).

Section 4.7 discusses the issue of finding optimal filter parameters. Ideally one would like to develop a procedure that automatically finds the optimal set of filter parameters, regardless of the characteristics of the data or the RFI. Another issue that is addressed in this section is whether the same filter tap weights may be used over many successive range lines. This is an important issue, because it might allow the LMS adaptive filter to be re-written in terms of an equivalent transfer function, which would facilitate efficient integration with the range-Doppler algorithm. This method is also an original contribution of this thesis and is described in detail in Section 4.8. Finally, Section 4.9 describes a novel technique for reducing range sidelobes, which arise as an unwanted by-product of the RFI suppression stage. This technique is demonstrated on simulated data and also on real P-band and VHF-band data.

The development, coding, simulation and testing of these techniques is the candidate's own work. Some of the material in this chapter has been published in the Proceedings of COMSIG'98 (Lord and Inggs 1998), Electronics Letters (Lord and Inggs 1999b) and in the Proceedings of IGARSS'99 (Lord and Inggs 1999a).

## 4.2 Approaches to RFI Suppression

Suppressing radio interference from a received signal essentially involves three steps (Abend and McCorkle 1995):

1. Finding a model to parameterise the interfering signals;

2. Estimating the parameters of the interfering signals using the measured data;

3. Using the estimated parameters to suppress the interference in the data.

Modelling the interference environment would ideally include information such as the statistics on the density of the interference emitters, the identity (type) of emitters, their effective radiated power, modulation bandwidth, duty factor and their temporal dependence. The most direct way of achieving this is to make use of "sniffer" pulses or "listening beforehand" schemes (Abend and Mc-Corkle 1995). This method is useful for many signal processing methods, but its effectiveness depends strongly on how long the RFI remains coherent. Most approaches use a model of the RFI as being a superposition of single sinusoidal "tones", and of the wideband signal-plus-system noise as white noise. Surveys performed by the Grumman E-2C UHF radar (420–450 MHz) (Koutsoudis and Lovas 1995) have shown that 50 % of emitters have a spectral bandwidth between 0–50 kHz (single channel voice/radio telegraphy), 40 % between 50–150 kHz and less than 10 % have a bandwidth greater than 150 kHz (data communications, multichannel telephony, etc.) It is important to estimate the modulation time of the RFI, which is the inverse of the RFI bandwidth, in order to predict whether the parameters of the modelled sinusoidal interference change across one range line, so as to deduce whether the tone model of the RFI breaks down. According to Braunstein *et al* (Braunstein, Ralston and Sparrow 1994), most RFI has a modulation time of 5–10 $\mu$s, which is consistent with an effective bandwidth of a few hundred kHz or less.

RFI suppression algorithms fall into two classes, namely:

1. Spectral estimation and coherent subtraction approaches;

2. Various filter approaches.

The relative merits and disadvantages of these approaches are discussed in the following subsections. One approach that is not investigated here is the creation of antenna pattern nulls in the direction of the RFI source as a means for suppressing the interference. This approach has been addressed by Goris *et al* (Goris, Joseph, Hampson and Smits 1999).

## 4.2.1 Spectral estimation and coherent subtraction approaches

These approaches have been shown to be extremely effective and powerful to the extent that the model of RFI as a superposition of sinusoids is true. They require the estimation of the frequency, phase and amplitude $(\omega, \phi, A)$ of each interfering sinusoid, after which the sinusoids are subtracted from the contaminated signal. Their performance is excellent in terms of low signal distortion and good interference suppression. However, their effectiveness is reduced for high modulation bandwidths, since the parameters change over the record length. For computational efficiency and effectiveness, these methods must be "tuned" to use *a priori* knowledge, such as knowledge of where the FM-broadcast band is located (Miller, McCorkle and Potter 1995). Furthermore, the parameters of the tones (especially the phase) must be estimated for every pulse.

Braunstein *et al* (Braunstein et al. 1994) have achieved very good results using a *maximum likelihood estimate* (MLE) approach. For a single sinusoid in white noise the parameter vector $(\omega, \phi, A)$ can be found analytically; however for multiple sinusoids it becomes an extremely difficult nonlinear problem involving $3m$ variables, where $m$ is the number of sinusoids to be estimated. An efficient technique of overcoming this problem is to use an iterative algorithm, where the initial guess of the estimates is iteratively improved. The initial guess may be obtained from the data spectrum by applying an FFT. Another method would be to model the RFI, signal and noise as an *autoregressive* (AR) process (Abend and McCorkle 1995), (Marple, S. L. Jr. 1987). The estimate $\widehat{x}[n]$ of the $n$th sample of the measured data $x[n]$ is given by

$$\widehat{x}[n] = -\sum_{k=1}^{p} a[k]\, x[n-k] + u[n] \tag{4.1}$$

where $p$ is the order of the model, indicating that $p/2$ sinusoids can be estimated, $a[k]$ are the autoregressive parameters which need to be derived from the mea-

sured data, and $u[k]$ is the signal plus noise (without interference). According to Braunstein *et al* (Braunstein et al. 1994) the results obtained by using this method are similar to those obtained by using the MLE method.

Golden *et al* (Golden, A. Jr., Werness, Stuff, DeGraaf and Sullivan 1995) used a *parametric maximum likelihood* (PML) algorithm for the estimation of the parameters of the RFI tones. This algorithm is also applied to deramp SAR. It is claimed that 90–95 % of the RFI that could have corrupted a SAR image may be removed. The number of iterations through the PML algorithm at each threshold is approximately equal to the number of tones being estimated.

Miller *et al* (Miller et al. 1995) have developed a *chirp-least-squares algorithm with clipping* (CLSC). When comparing this method to adaptive FIR filtering methods, the following advantages are claimed:

- An estimate-and-subtract algorithm provides the narrowest possible stop-band for a given data length and therefore minimises time-sidelobes.

- The CLSC technique allows iterative, nonlinear signal (target) excision, which reduces sidelobes and signal loss even further.

- There are no filter edge effects.

This method makes use of *a priori* knowledge of the RFI environment. A non-least-squares approach is used to model FM signals, which vary by as much as 75 kHz from the centre frequency.

Ferrell (Ferrell 1995) has developed a method which requires 2-D compression of the SAR image (containing both signal and interference), after which a second compressed SAR image (containing only interference) is coherently subtracted. This requires two arrays of data to be collected in an interleaved manner, which may require the PRF to be increased by a factor of 2. It is claimed that this method leaves the target and clutter phase history essentially intact.

## 4.2.2   Filter approaches

A common suppression approach is to examine the spectrum of the contaminated signal, to identify the interference spikes which are usually many dB larger than

the signal, and then to remove these spikes with a notch filter. Although the notching concept is effective for very narrowband interferers and a small number of emitters, it can also produce adverse effects on the overall radar system performance (Koutsoudis and Lovas 1995), such as reducing image intensity, reducing range resolution, creating loss in the target's integrated signal-to-noise ratio and introducing time-sidelobes.

Koutsoudis and Lovas (Koutsoudis and Lovas 1995) describe an RFI *Minimisation Algorithm* developed by Grumman Aerospace Corporation, which is based on least-mean-squares estimation theory. A single filter is used to achieve both the interference suppression as well as the equalisation needed to overcome the distortions caused by the notching function. This method has been tested extensively using numerous data sets, and excellent performance results have been obtained for all scenarios.

Buckreuss (Buckreuss 1998) has implemented a notch filter to suppress RFI in contaminated P-band data. The interferences have been removed to a large extent, with some sidelobes visible in areas with intense backscatter, as well as a slight degradation of the contrast.

Abend and McCorkle (Abend and McCorkle 1995) have achieved good results using an adaptive FIR filter approach. The adaptive filter is an over-determined system producing an FIR filter with $n$ taps, independent of the number of interfering signals. As opposed to tone extraction methods, this method simultaneously eliminates hundreds of narrowband interferers. A low update rate for the filter tap weights is allowed, since the filter weights were found to be effective for hundreds of subsequent radar pulses. Furthermore, minimal computational complexity is required, making this a very fast method. An iterative technique has been used to reduce the range sidelobes caused by the filter's impulse response. The adaptive filter is based on an autoregressive (AR) all-pole interference model, which also models the RFI as sinusoidal tones. However, the sinusoidal model needs to be valid across the relatively short filter length only. Furthermore the filter depends only on spectral energy, so the tap weights are not affected by the phase of the interference tone. A further advantage is that the adaptive filter "learns" the environment. It is claimed that the interference suppression filter can be superior to the tone extractor (Abend and McCorkle 1995). A disadvantage of using a filter approach is the reduction in record length that arises because of edge effects.

Le *et al* (Le, Hensley and Chapin 1997) have implemented an LMS adaptive filter with very good results. The filter performance with respect to the filter parameters is analysed in terms of radar performance parameters such as the *integrated sidelobe ratio* (ISLR) and *peak sidelobe ratio* (PSLR).

# 4.3    Measurements and Characteristics of RFI as Measured by the SASAR System

## 4.3.1    Introduction

Images obtained from the VHF-band SASAR system have shown that even in remote areas in South Africa the VHF-band is heavily contaminated with RFI. This section presents an investigation into the RFI environment encountered in South Africa in the VHF-band by analysing RFI that has been recorded by the SASAR system (Lord and Inggs 2000). This investigation includes RFI characteristics such as the number and density of emitters, their effective radiated power and their bandwidths. Information regarding the identity of emitters was given in Section 1.4.

The most direct way to measure RFI is to make use of "sniffer" pulses or "listening beforehand" schemes (Abend and McCorkle 1995). A similar method entails the recording of data before the transmitted pulse has returned to the receiver, i.e. before the nadir return. Both of these methods were employed by the SASAR system and therefore offered the unique opportunity to measure and characterise the RFI environment at VHF-band in South Africa.

## 4.3.2    RFI measurements

In order to assess the amount of RFI that could be expected by the SASAR system in the Cape Town area, a simple quarter wavelength antenna was attached to a spectrum analyser with a bandwidth resolution of 10 kHz. The output of the spectrum analyser from 129–153 MHz is shown in Figure 4.1 (a). This figure shows that there is significant RFI just above 141 MHz, which is the centre frequency of the SASAR system.
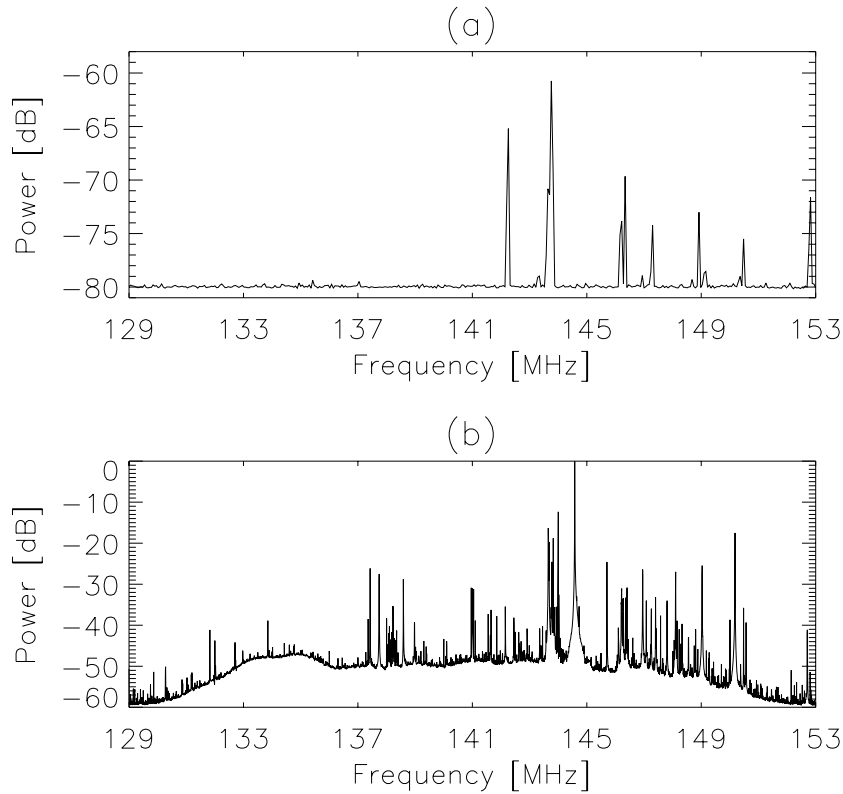
*Figure 4.1:* (a) RFI measured in Cape Town with a spectrum analyser; (b) RFI measured with the SASAR system near the Southern Cape, South Africa.

During a recent flight over the Southern Cape area in South Africa, the blanking switch of the SASAR system was deliberately switched on, so that no pulses were transmitted. This permitted the background interference to be recorded. Since the sampling rate of the SASAR system is 24 MHz, the recorded spectrum ranges from 129 MHz to 153 MHz, centred around 141 MHz. Figure 4.1 (b) shows the magnitude averaged range spectrum of 1000 range lines for the H-receive polarisation data, with a PRF of 136 Hz. The averaging of magnitude range spectra is performed in order to enhance the interference which is often fairly constant, whereas the noise, due to its random nature, averages out. Note that this graph shows that the antenna and receive filters have not adequately limited the receive bandwidth to 12 MHz, which is the transmitted pulse bandwidth of this system.

Although not shown here, the dominant interference for V-receive polarisation was found to be about 5 dB less than for H-receive polarisation (refer to Fig-

74

ure 1.2). Even though the interference pattern shown in Figure 4.1 (b) is not identical to the pattern measured by the spectrum analyser, the dominant interference in this case is again situated above 141 MHz.

### 4.3.3 Number and density of emitters

In order to count the number of RFI spikes shown in Figure 4.1 (b), the noise floor was estimated and subtracted from this graph. This can be achieved by applying a median filter to the averaged range spectrum. Median filtering is effective in removing isolated high or low values, which in this application are the RFI spikes.

Figure 4.2 shows the number of RFI spikes for both H- and V-receive polarisations as a function of power above the noise floor. Most RFI spikes are less than 10 dB above the noise floor. Only about 10 emitters where counted to be above 20 dB of the noise floor. It is important to note, however, that many emitters are so closely spaced that they appear to be single emitters with larger bandwidths. Referring to Figure 4.1 (b) there appear to be many emitters lumped together just below 145 MHz and in the region from 146–150 MHz. The next subsection investigates the bandwidth of the emitters with respect to their power level above the noise floor.
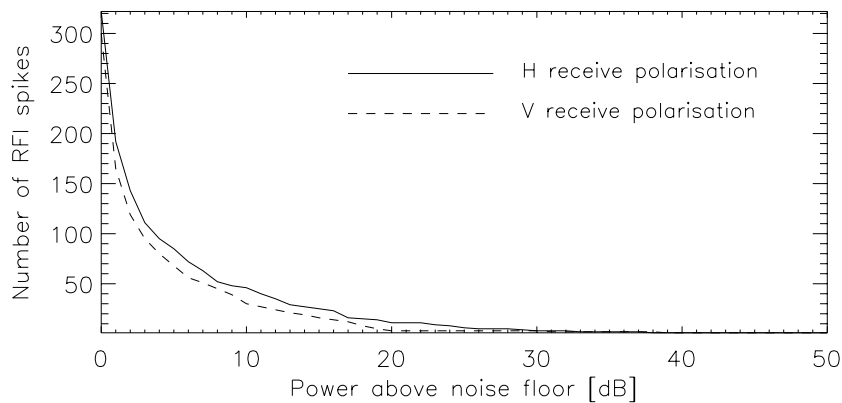


*Figure 4.2: Number of RFI spikes for both H and V polarisation versus power above noise floor.*

## 4.3.4 Radiated power and bandwidth

It has already been stated in Section 4.2 that surveys performed by the Grumman E-2C UHF radar (Koutsoudis and Lovas 1995) have shown that 50 % of emitters have a spectral bandwidth between 0–50 kHz, 40 % between 50–150 kHz and less than 10 % have a bandwidth greater than 150 kHz. It is important to estimate the modulation time of the RFI, which is the inverse of the RFI bandwidth, in order to predict whether the parameters of the modelled sinusoidal interference change across one range line, so as to deduce whether the model of the RFI consisting of sinusoidal tones breaks down. According to Braunstein *et al* (Braunstein et al. 1994), most RFI has a modulation time of 5–10 $\mu$s, which is consistent with an effective bandwidth of a few hundred kHz or less.

The graph shown in Figure 4.1 (b) has been investigated to find the percentage of RFI emitters that have a specified bandwidth and a specified power level above the noise floor. The results of this investigation are listed in Table 4.1. For example, 58 % of emitters which are above 5 dB of the noise floor have a bandwidth between 0 and 10 kHz. Less than 10 % of emitters have a bandwidth greater than 50 kHz, regardless of their power level above the noise floor. These findings suggest that for this isolated case the RFI environment is more narrowband than that encountered by the Grumman E-2C UHF radar, since about 60 % of emitters investigated have a bandwidth less than 10 kHz. This also suggests that RFI suppression algorithms that model the RFI as sinusoidal tones, such as the LMS adaptive filter described in Section 4.6, are applicable under these circumstances.

| Cutoff (dB) | % Emitters with bandwidths (in kHz) | | | |
|---|---|---|---|---|
| | 0–10 | 11–20 | 21–50 | > 50 |
| 2 | 62 | 19 | 10 | 9 |
| 3 | 62 | 18 | 12 | 8 |
| 5 | 58 | 18 | 16 | 8 |
| 10 | 62 | 24 | 9 | 5 |
| 20 | 71 | 21 | 1 | 7 |

***Table 4.1:*** *Percentage of RFI emitters within specified frequency bands and above specified power level above noise floor.*

## 4.4 Description of Real Data Containing RFI

### 4.4.1 P-band data

**Background**

The P-band image used in this thesis was generated by the experimental airborne SAR system E-SAR of the DLR. It shows an area in the vicinity of Weilheim, Germany, and is displayed in Figure 4.3. The raw data was supplied to the author by the DLR, Oberpfaffenhofen, Germany, and the processing was done with the G2 range-Doppler processor developed at the University of Cape Town. Table 4.2 lists the relevant radar parameters of this data set. The RF interference in this image can be clearly seen as bright lines in the range direction. The interference is more dominant at the far range due to *sensitivity time control* (STC). This is an important issue and is discussed in more detail below.
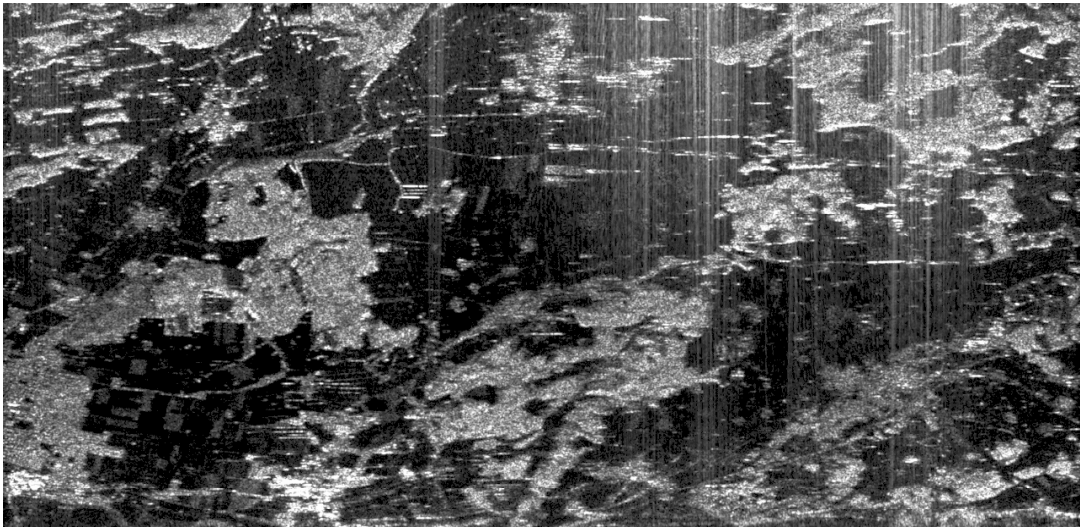


**Figure 4.3:** *P-band image of the vicinity of Weilheim, Germany, degraded by RF interference. The flight path is along the horizontal axis, with near range towards the bottom of the image.*

| | | |
|---|---|---|
| Centre frequency | $f_c$ | 450 MHz |
| Chirp bandwidth | $B_t$ | 18 MHz |
| Pulse length | $T_p$ | 5 $\mu$s |
| A/D (complex) sample rate | $f_{ad}$ | 60 MHz |
| Range bins | | 2048 |

***Table 4.2:*** *Parameters of P-band E-SAR data.*

**Sensitivity Time Control**

Since the received signal power decreases proportionally to the fourth power of the target range, it is common in radar systems to compensate for this feature by adjusting the signal strength proportionally. This process increases the dynamic range of the receiver and is known as *sensitivity time control* (STC). Before range compression, the "distortion" of the signal due to the application of STC is removed by dividing every range line by the appropriate STC curve, to ensure that the range compression will be applied on the undistorted signal. After range compression, the STC is again applied to the data to ensure that targets at near range do not appear brighter than similar targets at far range. Figure 4.4 shows the STC curve for the P-band data. It should be noted that this curve is not actually a 4th power curve, but rather an approximately 3rd power curve on account of antenna effects and SAR azimuth focusing.

Since the signal transmitted by interfering sources is independent of the signal transmitted by the radar, and since the distance of the interfering sources from the radar remains approximately constant during one range line, the interference power received by the radar remains approximately constant and does not decay across the range window, as does the signal power. One would therefore expect the STC curve to attenuate the interference signal at near range relative to far range. This can be seen in Figure 4.5 (a), which shows the real part of a range line of the P-band data before removal of the STC. It can be seen that the interfering signal is severely clipped at the far range. This results in the appearance of higher harmonics in the frequency domain. Furthermore, the signal, which rides on top of the interference, is therefore also clipped. These aspects cause a degradation in the final image quality.

It is important to remove the STC before finding the filter weights of the LMS adaptive filter (see Section 4.6.1), since the interference amplitude ought to re-
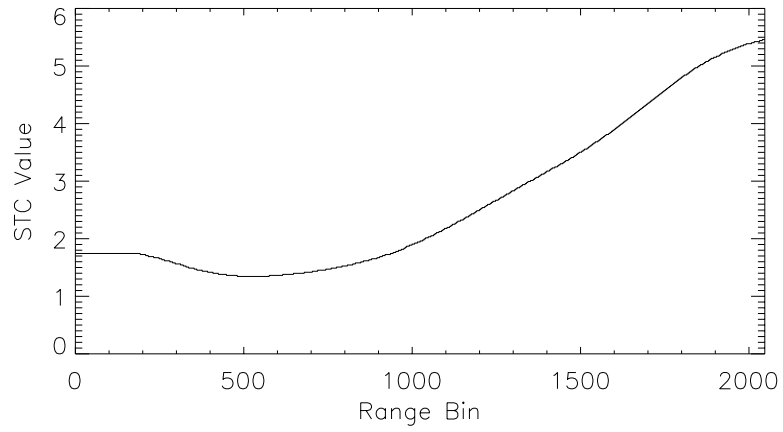
**Figure 4.4:** *STC curve of P-band data.*
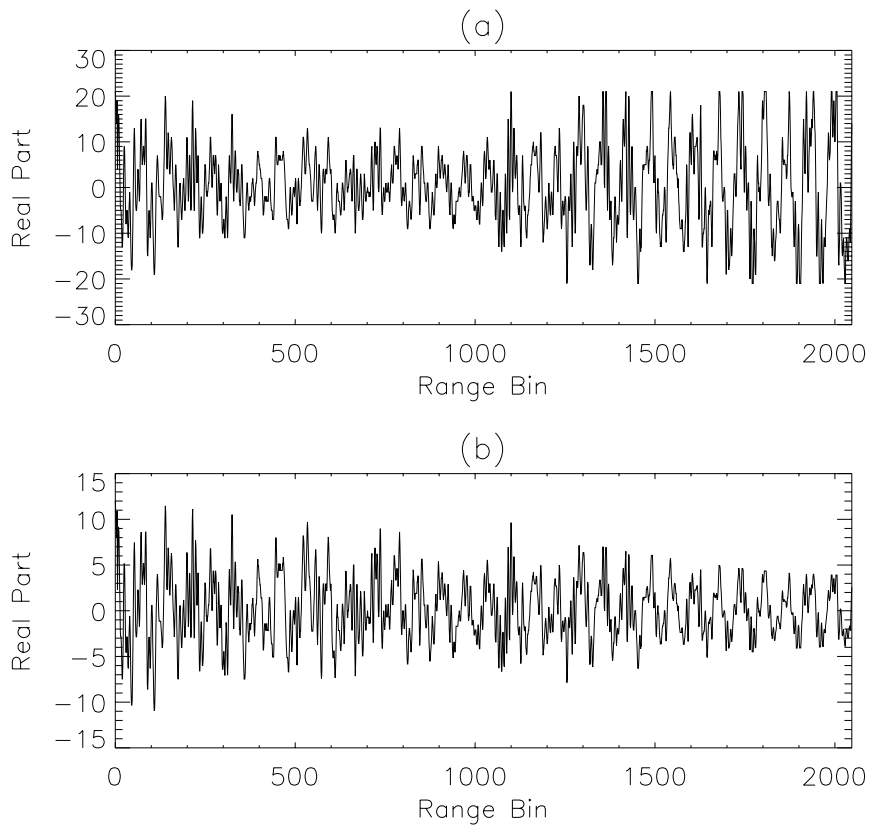


**Figure 4.5:** *Real part of a range line of the P-band data: (a) before STC removal; (b) after STC removal.*
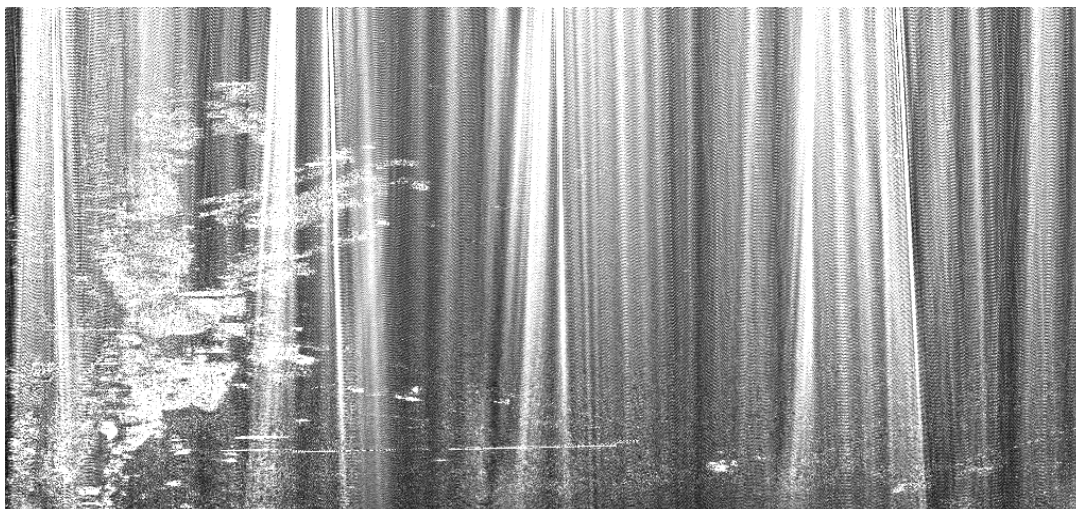
**Figure 4.6:** *VHF-band image of the vicinity of Upington, South Africa, degraded by RF interference. The flight path is along the horizontal axis, with near range towards the bottom of the image.*

main as constant as possible across the range line. Figure 4.5 (b) shows the same range line as in Figure 4.5 (a) after STC removal (note different vertical scales). The interference now seems to decay with range instead of remaining constant; however, this can be attributed to the clipping described above.

### 4.4.2 VHF-band data

The VHF-band image used in this thesis was generated by the South African SAR (SASAR) system. It shows an area in the vicinity of Upington, South Africa, and is displayed in Figure 4.6. The raw data was processed with the G2 range-Doppler processor developed at the University of Cape Town (Horrell 1999). The size of the image is 16.7 km in azimuth and 12.8 km in range. Table 4.3 lists the relevant radar parameters of this data set. The RFI in this image is very

| Centre frequency | $f_c$ | 141 MHz |
|---|---|---|
| Chirp bandwidth | $B_t$ | 12 MHz |
| Pulse length | $T_p$ | 10.5 $\mu$s |
| A/D (complex) sample rate | $f_{ad}$ | 24 MHz |
| Range bins | | 2048 |

**Table 4.3:** *Parameters of VHF-band SASAR data.*

80

severe, hiding many features which become visible only once the interference has been suppressed. Note that the bright RFI lines have a slope that is due to the range-varying azimuth reference function (Horrell 1999). No STC curve has been applied to this data.

## 4.5 The Notch Filter

### 4.5.1 Description

The notch filter is probably the most intuitive approach to suppressing RFI. Since RFI is narrowband when compared with the transmitted pulse bandwidth, it shows up as narrow spikes in the frequency domain. These spikes are usually many dB stronger than the surrounding signal level. In order to estimate the interference, it is very useful to average a number of magnitude range spectra, because the signal, due to its random nature, will average out, but the RFI, due to its often fairly constant nature, will be enhanced. The interference spikes can then be identified in the frequency domain and notched out.

### 4.5.2 Application of median filter

When obtaining an averaged range spectrum of the data, one would ideally like to have the averaged range spectrum of the signal-minus-RFI, so that everything above a specified level of this "signal envelope" can be identified as RFI and notched out. This was successfully done by applying a median filter to the averaged range spectrum of the signal-plus-RFI. In an ordered set of values, the median is a value with an equal number of values above and below it. Median smoothing replaces each point with the median of the one- or two-dimensional neighbourhood of a given width. Therefore median filtering is effective in removing isolated high or low values, which in this application are the RFI spikes. This concept is illustrated in Figure 4.7. Figure 4.7 (a) shows 1000 averaged range spectra of the noisy VHF-band data. The 12 MHz bandwidth of the data is apparent, since an appropriate windowing function has been applied to the data. The frequency bin size is equal to the sampling frequency divided by the number of range bins, which is $24\,\text{MHz} \div 2048 = 11.7\,\text{kHz}$. After applying median filters
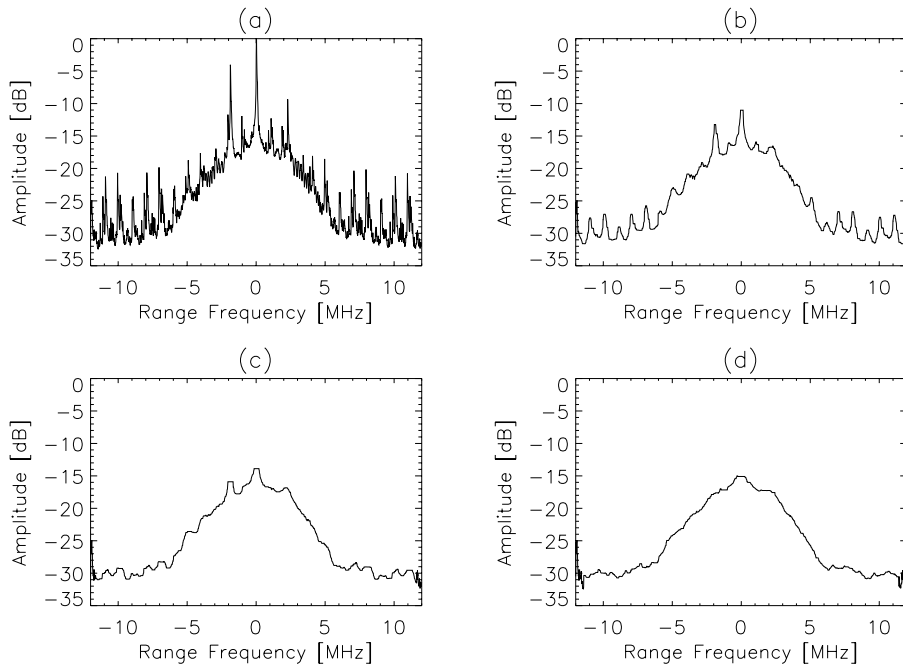
***Figure 4.7:*** *Averaged range spectrum of VHF-band data, showing (a) the noisy data; (b) the signal envelope obtained using a 33-kernel median filter; (c) the signal envelope obtained using a 65-kernel median filter; (d) the signal envelope obtained using a 101-kernel median filter.*

of length 33, 65 and 101 to this range spectrum, the signal envelopes shown in Figures 4.7 (b), (c) and (d) are obtained respectively. The length of the median filter becomes important when many RFI sources are lumped together, which leads to unwanted humps in the filtered spectrum, as shown in Figure 4.7 (b). In this example, a median filter of length 101 is most appropriate.

After finding the signal envelope, it is subtracted from the noisy range spectrum, as shown in Figure 4.8 (c). It is now straightforward to identify all RFI spikes which are a certain level above the signal envelope. Figure 4.8 (d) shows the cleaned range spectrum after notching out all interfering spikes more than 3 dB above the signal envelope. The notch filter incorporated with the G2 range-Doppler processor was implemented by applying notches with a tapering function in order to minimise sidelobes in the time domain. Furthermore, instead of notching out the spikes, they can also be replaced with the corresponding value of the signal envelope with random phase. However, it was found that this did not have any significant effect on the final image quality.
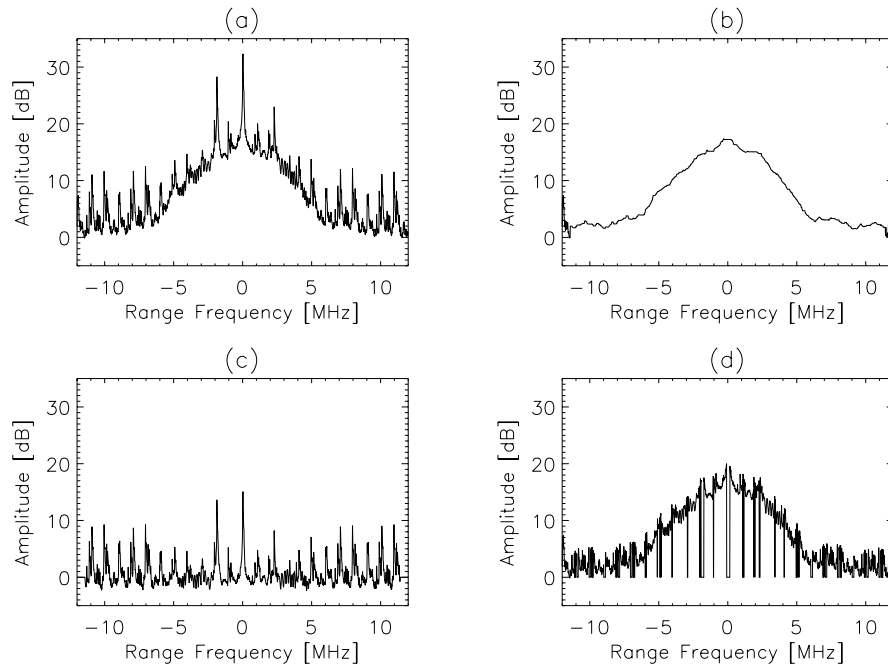
**Figure 4.8:** *Averaged range spectrum of VHF-band data, showing (a) the noisy data; (b) the signal envelope obtained using a 101-kernel median filter; (c) the noisy spectrum after subtracting the signal envelope; (d) the cleaned spectrum after notching out all RFI spikes more than 3 dB above the signal envelope.*

### 4.5.3   Integration with range-Doppler algorithm

After finding the positions of the RFI spikes in the averaged range spectrum, this information can be used to place notches at the appropriate positions in the spectrum of the matched filter $M(\omega)$, which is typically the complex conjugate of the transmitted pulse spectrum. This allows the range-compression and RFI suppression to be done simultaneously, leading to a very efficient implementation of the notch filter. A similar method is used to integrate the LMS adaptive filter with the range-compression stage of the range-Doppler algorithm. This method is described in Section 4.8.

### 4.5.4   VHF-band data results

Figure 4.9 shows the cleaned VHF-band image after applying a notch filter. The median length was 33 and the RFI cut-off level above the signal envelope
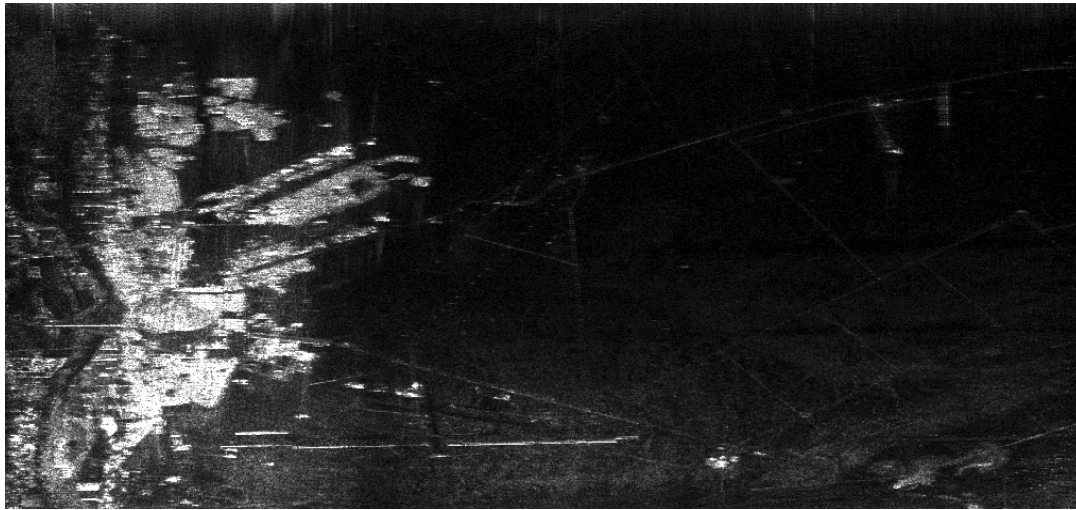
**Figure 4.9:** *VHF-band image after applying a notch filter to suppress RFI.*
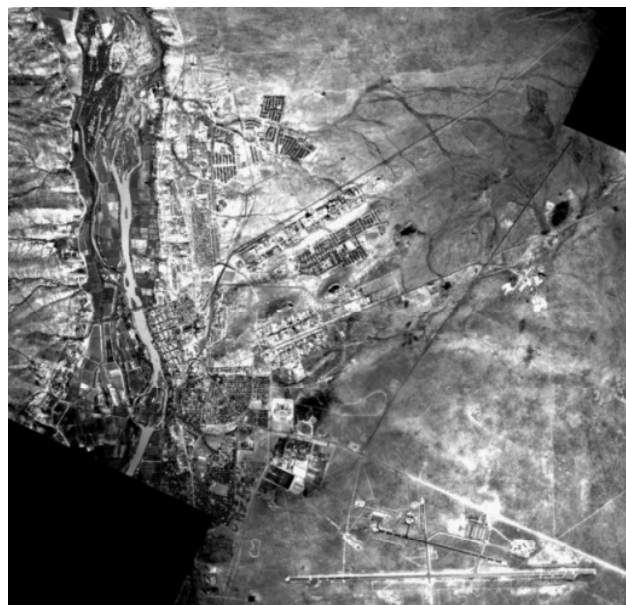


**Figure 4.10:** *Optical photo mosaic of VHF-band image.*
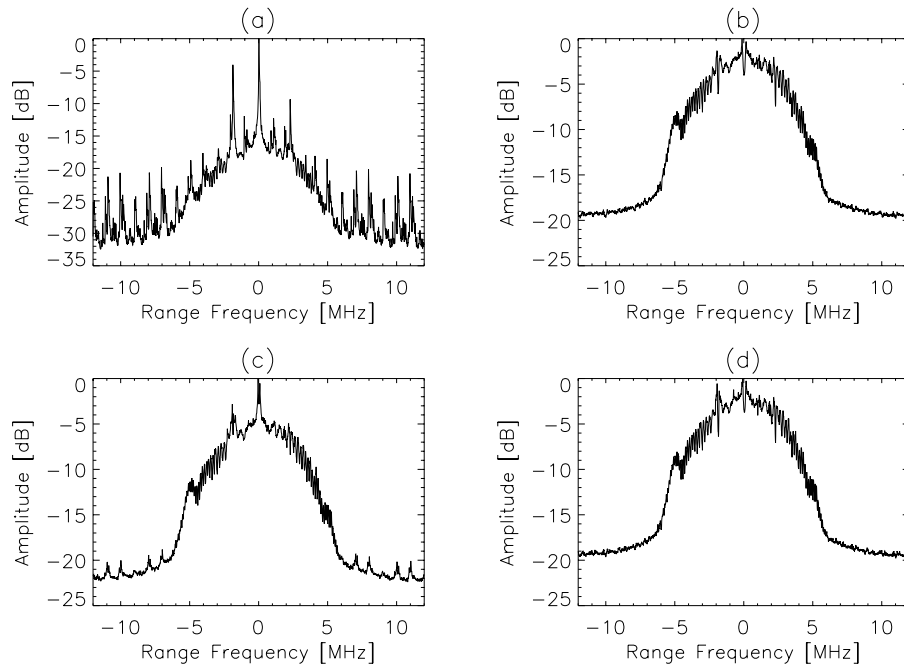
***Figure 4.11:*** *Averaged range spectrum of noisy and cleaned VHF-band data.*

was 3 dB. To obtain the averaged range spectrum, 100 magnitude range spectra were averaged. The notch filter was then applied to these 100 range lines, upon which the notch filter was updated using the same method. The cleaned image is definitely a vast improvement when compared to the noisy image shown in Figure 4.6. Many faint features have become visible, especially in the right half of the image. Figure 4.10 shows an optical photo mosaic of the area (courtesy Gavin Doyle, RRSG UCT). The town of Upington is seen as the bright region to the left of the image. The regions away from the town have very low radar backscatter at SASAR frequencies and correspond to flat unvegetated desert regions. The bright, horizontal feature near the base of the image is the airport fence. Other fence structures are also visible as linear features.

Figure 4.11 (a) shows the contaminated averaged range spectrum of the noisy image, and Figure 4.11 (b) shows the averaged range spectrum of the cleaned image shown in Figure 4.9. Figure 4.11 (c) shows the averaged range spectrum of a cleaned image where the RFI cut-off level has been set to 6 dB. There is still a prominent spike visible near the middle of the spectrum, showing that a median filter length of 33 is in fact insufficient (see Figure 4.7). Figure 4.11 (d) shows the averaged range spectrum of a cleaned image where the notch filter has

been updated only every 1000th range line, although only 100 range spectra were averaged. This verifies that the RFI is fairly constant, and that the notch filter can be implemented more efficiently by applying it to more range lines than were used to form the averaged spectrum.

## 4.6   The LMS Adaptive Filter

### 4.6.1   Description

Adaptive filters have been widely used in interference suppression applications (Abend and McCorkle 1995), (Glover, J. R. Jr. 1977), (Le et al. 1997), (Li and Stoica 1995), (Widrow, Glover, J. R. Jr., McCool, Kaunitz, Williams, Hearn, Zeidler, Dong, E. Jr. and Goodlin 1975a). In contrast to fixed filters, they have the desirable property of being able to adjust their own parameters automatically. Little or no *a priori* knowledge of the signal or noise characteristics is required. It is, however, assumed that the interference is sinusoidal. The adaptive filter relies on a recursive algorithm, which, in a stationary environment, converges to the optimum Wiener solution (Widrow et al. 1975a). In a non-stationary environment, the algorithm offers a tracking capability, whereby it can track time variations in the statistics of the input data.

Figure 4.12 shows a schematic of the LMS adaptive filter as it is used for RF interference cancelling. It requires a primary input $d$ and a reference input $x$, which is obtained by delaying the primary input for some time delay $\Delta$. The adaptive linear combiner weighs and sums a set of input signals to form an
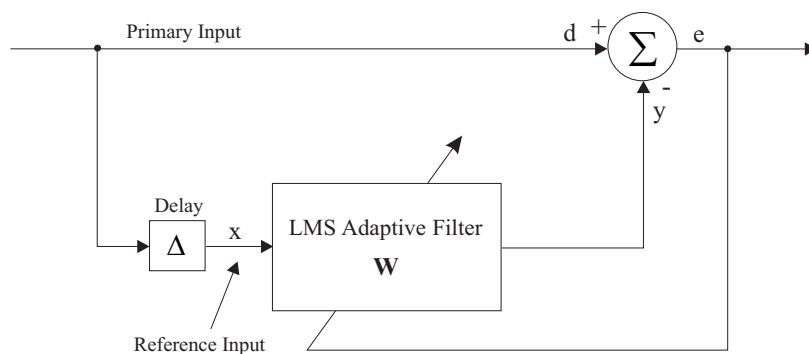


***Figure 4.12:*** *The LMS adaptive filter.*

86

adaptive output. The $n$-element input signal vector $\mathbf{D}$ and the weight vector $\mathbf{W}$ are defined at time $j$ as follows:

$$\mathbf{D}_j = \{d(j), d(j-1), d(j-2), ..., d(j-n+1)\} \tag{4.2}$$

and

$$\mathbf{W}_j = \{w_0(j), w_1(j), w_2(j), ..., w_{n-1}(j)\} \tag{4.3}$$

The reference signal vector $\mathbf{X}_j$ is defined as

$$\mathbf{X}_j = \mathbf{D}_{j-\Delta} \tag{4.4}$$

The output $y(j)$ of the filter is equal to the inner product of the row vectors $\mathbf{W}_j$ and $\mathbf{X}_j$

$$y(j) = \mathbf{W}_j \cdot \mathbf{X}_j^T \tag{4.5}$$

This output is an estimate of the RF interference. The error signal $e(j)$, which is the desired cleaned radar signal, is obtained by subtracting the RF interference estimate from the primary input $d(j)$ according to

$$e(j) = d(j) - y(j) = d(j) - \mathbf{W}_j \cdot \mathbf{X}_j^T \tag{4.6}$$

The LMS adaptive algorithm minimises the mean-square error $e(j)$ by recursively altering the weight vector $\mathbf{W}_j$ at each sampling instant according to the Widrow-Hoff algorithm (Widrow, McCool and Ball 1975b), yielding

$$\mathbf{W}_{j+1} = \mathbf{W}_j + 2\mu e(j)\mathbf{X}_j^* \tag{4.7}$$

where the $*$ symbol designates complex conjugation and $\mu$ is a convergence factor controlling stability and rate of adaptation. A larger value of $\mu$ increases the rate of convergence, but also leads to a larger final misadjustment, which is a quantitative measure of the amount by which the final value of the mean-squared error deviates from the minimum mean-squared error that is produced by the optimum Wiener filter.

## 4.6.2   Simulation setup and results

The adaptive filter was applied on simulated data to verify its suitability for RFI suppression. The parameters used for the simulation are the same as the P-band parameters listed in Table 4.2. This facilitated the use of an optimum set of filter parameters for suppressing the RF interference in the P-band data.
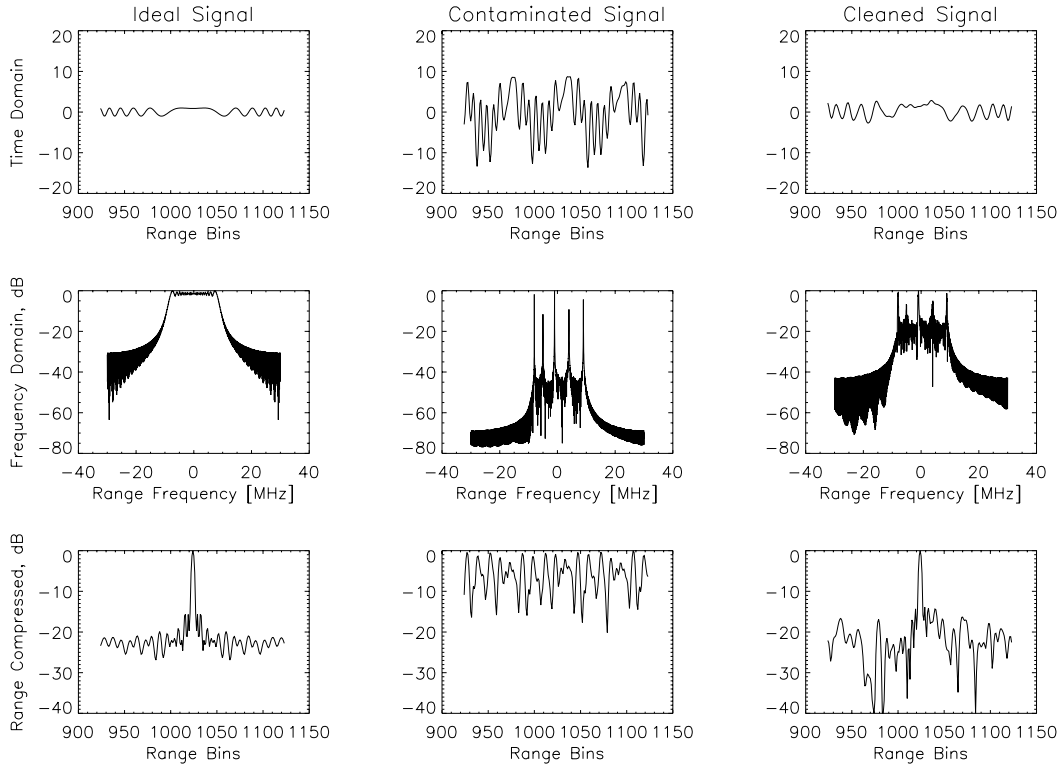
*Figure 4.13:* *Simulation results demonstrating the effectiveness of the adaptive filter when applied to RFI suppression. The three columns show the ideal, contaminated and cleaned signals respectively. The first row shows the real part of the signal in the time domain, the second row shows the signal in the frequency domain, and the third row shows the range compressed signal.*

The simulation was assembled as follows: a clean signal (see first column of Figure 4.13) representing the ideal return of a single point target was injected with baseband RF "interference" in the form of five pure sinusoids at frequencies $-8$, $-5$, $-1$, 4 and 9 MHz with corresponding interference-to-signal amplitude ratios of 6, 2, 7, 4 and 5 dB respectively and with random phase (see second column of Figure 4.13). White noise with an SNR of 20 dB was also added. This contaminated signal was fed to the adaptive filter (see third column of Figure 4.13), and the performance of the filter was evaluated by range compressing the filter output and measuring the target mainlobe width, the peak sidelobe ratio (PSLR) and the integrated sidelobe ratio (ISLR), measured across 200 range bins. The extent of the main peak region was found by defining the main peak as the region bounded by the points at which the gradient of the peak changed sign. The ISLR

| Filter Parameters | | Radar Performance | | |
|---|---|---|---|---|
| weights | $\mu$ | ML Width [range bins] | PSLR [dB] | ISLR [dB] |
| 20 | $10^{-4}$ | 3.1 | $-5.30$ | 3.09 |
| 20 | $10^{-5}$ | 3.2 | $-7.27$ | 1.20 |
| 20 | $10^{-6}$ | 3.4 | $-1.73$ | 10.2 |
| 100 | $10^{-4}$ | 2.9 | $-3.08$ | 7.15 |
| 100 | $10^{-5}$ | 3.1 | $-9.97$ | $-0.68$ |
| 100 | $10^{-6}$ | 3.2 | $-12.4$ | $-0.63$ |
| 256 | $10^{-4}$ | unstable | unstable | unstable |
| 256 | $10^{-5}$ | 3.0 | $-7.89$ | 0.40 |
| 256 | $10^{-6}$ | 3.2 | $-12.9$ | $-2.78$ |

**Table 4.4:** *Radar performance versus LMS adaptive filter parameters.*

is defined here as the ratio of the integrated energy in the sidelobe region to the integrated energy contained in the main peak region. For improved accuracy, the power values were interpolated (using a Shannon interpolator) to one hundredth of a sample before measuring the resolution, PSLR and ISLR.

Table 4.4 gives an indication of how the radar performance is affected by the number of filter weights and the convergence factor $\mu$. The delay $\Delta$ has not been included, since it was found that a delay of one time sample was sufficient, and larger values of $\Delta$ did not affect the results significantly. The best set of filter parameters is found where the absolute value of the PSLR is largest and the value of the ISLR is smallest. It has to be noted that the value of $\mu$ is inversely dependent on the amplitude of the input vector, and therefore the absolute value is not as important as the relative change with respect to the number of weights. Furthermore, as the number of weights increases, the value of $\mu$ needs to be decreased appropriately; otherwise the filter output becomes unstable. This can be seen in Table 4.4 with 256 weights and $\mu = 10^{-4}$. Generally the performance increases as $\mu$ decreases. However, if $\mu$ becomes too small, the weights do not converge, which also yields poor performance. This was the case with 20 weights and $\mu = 10^{-6}$. The results also improve as more weights are used, but this increases computation time and edge effects.

Figure 4.13 graphically illustrates the results that were obtained with 256 weights

and $\mu = 10^{-6}$. The first column displays the ideal signal, without any interference. The second column displays the contaminated signal, with the spectrum completely dominated by noise and interference. The point target is not detectable in the range compressed signal shown in the last row. The third column shows the output of the adaptive filter, which is clearly a vast improvement compared to the noisy signal. Looking at the second row, the filter has significantly suppressed the spikes caused by the sinusoidal interferences. The point target is clearly visible in the range compressed signal, with the peak sidelobe being $-12.9\,\mathrm{dB}$ below the mainlobe, using a rectangular weighting window.

The adaptive filter has been modified as follows in order to improve the performance measured in terms of the PSLR and ISLR:

- The range compressed output of the adaptive filter sometimes displayed one very prominent sidelobe. In order to minimise this effect, the adaptive filter was swept through the input vector from both ends, using two separate weight vectors, after which the two output vectors were averaged. This yielded significant performance improvements in terms of peak sidelobe reduction.

- Smaller values of $\mu$ generally yielded better results, in terms of lower PSLR and ISLR. Sometimes, however, this resulted in the tap weights not converging after one sweep through the input vector, consisting of 2048 range bins. Therefore the adaptive filter was applied to the data twice, using the weight values of the first sweep as starting values for the second sweep.

- In order to minimise the edge effects of the filter, the input vector was zero-padded by the appropriate amount.

These filter modifications reduced the computational efficiency. Section 4.8 describes a method to integrate the LMS adaptive filter with the range-Doppler algorithm, leading to a very efficient implementation. Furthermore, a technique to suppress sidelobes is described in Section 4.9.
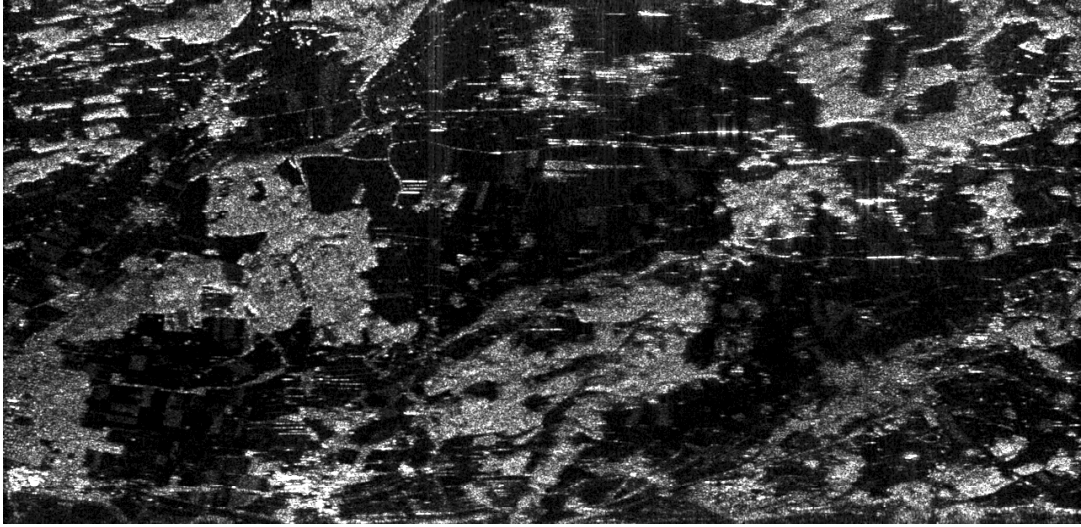
**Figure 4.14:** *P-band image after applying the LMS adaptive filter to suppress RF interference.*

### 4.6.3   P-band data results

Figure 4.14 displays the P-band image after it has been cleaned with a 512-tap LMS adaptive filter. The RF interference has been suppressed significantly, when comparing this image with the original image shown in Figure 4.3. Some features that were hidden by the interference have become visible, although sidelobes of bright targets have also become more pronounced. This issue is addressed in Section 4.9, where a technique for reducing these sidelobes is described.

In order to show how successfully the LMS adaptive filter has suppressed the RF interference, 100 range spectra were averaged before and after RFI suppression. Averaging a number of range spectra has the effect of enhancing the location and visibility of the interference spikes, because by coherently averaging the signal the random component is reduced, whereas the relatively constant interference is enhanced. However, it must be noted that the radar signal is not random within the unfocused SAR distance.

Figure 4.15 shows the averaged range spectrum of the noisy data, and the averaged range spectrum after the data has been cleaned with a 512-tap adaptive filter. The figure shows a large interference spike near the origin, and about 15 smaller spikes on either side of the origin. After the image has been cleaned, the large interference spike has been reduced by about 12 dB, which is a significant improvement. However, smaller interference spikes are still visible.
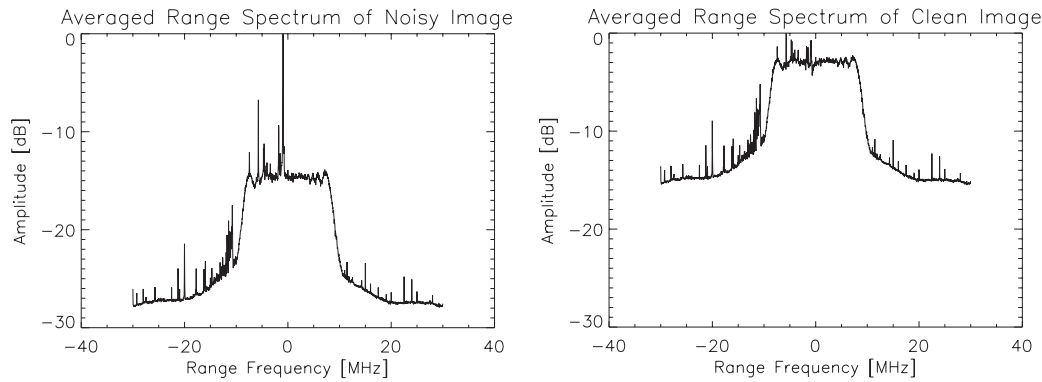
**Figure 4.15:** *Averaged range spectrum of noisy and cleaned P-band data.*

### 4.6.4  VHF-band data results

Figure 4.16 displays the VHF-band image after it has been cleaned with a 256-tap LMS adaptive filter. As was the case with the notch filter, the cleaned image is again a vast improvement when compared to the noisy image shown in Figure 4.6. Since no analytical and objective method was applied to compare the results obtained from the LMS adaptive filter with those obtained from the notch filter, it is difficult to say which technique yielded better results. Simply by looking at the images produced by the two filters, the LMS adaptive filter seems to yield slightly better results, perhaps because of its ability to adjust to the interference as the interference changes across one range line.
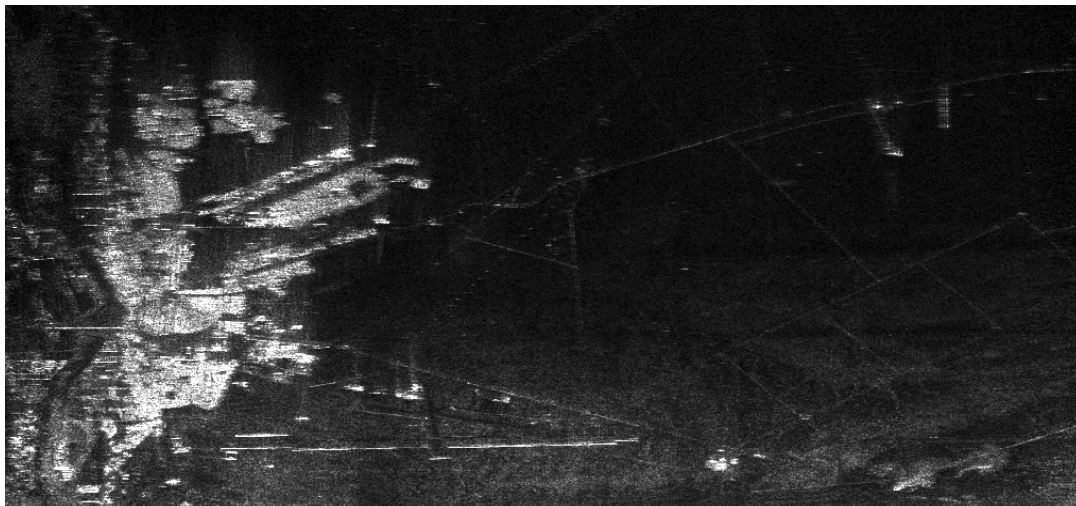


**Figure 4.16:** *VHF-band image after applying the LMS adaptive filter to suppress RF interference.*
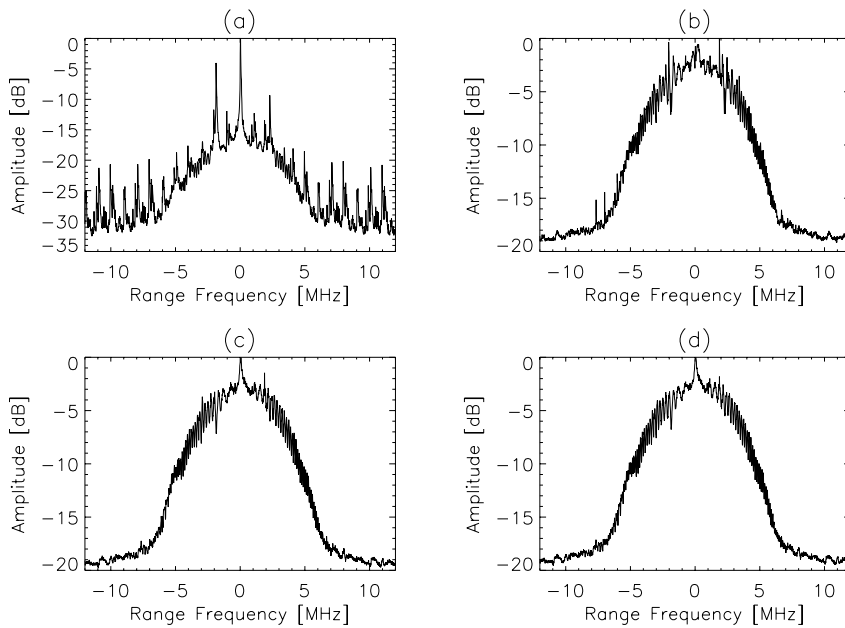
**Figure 4.17:** *Averaged range spectrum of (a) noisy VHF-band data; (b) cleaned data using a 64-tap LMS adaptive filter; (c) cleaned data using a 256-tap filter; (d) cleaned data using a 512-tap filter.*

Figure 4.17 shows a comparison between averaged range spectra after applying a 64-tap, a 256-tap and a 512-tap LMS adaptive filter. In all cases the RFI has been suppressed significantly.

## 4.7 Finding Optimal Parameters for the LMS Adaptive Filter

There are only three parameters associated with the LMS adaptive filter:

1. the delay $\Delta$;

2. the convergence factor $\mu$, and

3. the number of filter weights $N$.

It has been found that a delay $\Delta = 1$ sample is sufficient to decorrelate the reference input $x$ from the primary input $d$ (refer to Figure 4.12). This has also

been confirmed by other authors (Le et al. 1997). Therefore one only needs to find the convergence factor $\mu$ and the number of filter weights $N$. Another parameter that is of interest is the number of range lines across which the same set of filter weights may be applied successfully. This issue is addressed in Section 4.7.4.

## 4.7.1 Finding the convergence factor

There is an upper boundary on $\mu$, beyond which the weight-vector mean does not converge. It is shown by Widrow and Stearns (Widrow and Stearns 1985) that convergence is guaranteed only if

$$0 < \mu < \frac{1}{\lambda_{\max}} \tag{4.8}$$

where $\lambda_{\max}$ is the largest eigenvalue of the input correlation matrix. Widrow and Stearns go on to show that for a transversal adaptive filter, the convergence of the weight-vector mean is assured by:

$$0 < \mu < \frac{1}{(N+1)\,(\text{signal power})} \tag{4.9}$$

Although this is a more restrictive bound on $\mu$ than Equation 4.8, it is much easier to apply, since the signal power can be estimated more easily than the eigenvalues of the input correlation matrix.

The closer $\mu$ approaches 0, the smaller the convergence error of the weight-vector becomes when compared with the optimum Wiener solution. It is therefore desirable to make $\mu$ as small as possible. This causes the weight-vector to converge more slowly, which can be remedied by iterating the input vector several times, and keeping the weights at the end of each iteration as starting values for the next iteration. If this procedure is done for every range line, the computational burden increases tremendously, but, as will be shown in Section 4.8, it is intended to use the same weight-vector for many successive range lines.

The method implemented for finding the weight-vector starts with the first iteration by using a value of $\mu$ which is a tenth of the maximum value allowed according to Equation 4.9, and then divides this value of $\mu$ by 10 for each successive iteration, up to a maximum of 5 iterations. Thus, with each successive iteration the weight-vector is more finely tuned. The number of iterations and the division by a factor of 10 is arbitrary; however, good results have been achieved using these figures. Increasing the number of iterations is wasteful in terms of

computation time, and dividing $\mu$ by a factor greater than 10 often causes the weight vector to converge too slowly during the fifth iteration.

## 4.7.2  Finding a quality index

The most difficult aspect of finding the "optimal" filter parameters lies in finding a suitable quality index to serve as an objective value that quantifies how "well" the adaptive filter is doing. One method would be to create simulated data, containing a point target immersed in RF interference, and then to apply the adaptive filter to that data. After range-compressing the resulting cleaned signal, the mainlobe width, the peak sidelobe level and the integrated sidelobe level could be used as "goodness" parameters (this was demonstrated in Section 4.6.2). The simulated data should approximate as closely as possible the real dataset to be cleaned, by having the same number of range bins, the same A/D frequency, the same chirp bandwidth, *et cetera*. Most importantly, however, the RFI as well as the receiver noise should be modelled as accurately as possible. However, as the RF interference is often unknown, this method is unreliable. In addition, this method is cumbersome to implement and to automate.

A better way would be to find a quality index using the real dataset. The LMS adaptive filter tries to minimise the output power (refer to Section 4.6.1), and therefore it follows that the level of the output power should be a direct indication of how well the filter is doing. A possible quality index is therefore the ratio of the output power over the input power, subtracted from unity (the closer it approaches unity, the better the result). Thus we can define a quality index $\eta$ such that

$$\eta = 1 - \left( \frac{\text{Output Power}}{\text{Input Power}} \right) \tag{4.10}$$

This quality index is intuitive in the sense that the interference spikes become smaller as the quality index approaches unity. However, when this index is equal to unity, the output power is zero, which is obviously undesirable, since there is no signal power left. Therefore one would expect this index to reach some maximum value, at which point as much interference as possible has been filtered out of the corrupted signal.

95

### 4.7.3 Finding the number of weights

The number of interfering sinusoids that can be suppressed by the LMS adaptive filter depends directly on the number of weights $N$. Therefore better RFI suppression results are expected for higher values of $N$, at the expense of computation time. One might be tempted to think that the quality index defined above could be used to find an optimum value for $N$. However, in practice it has been found that $\eta$ *increases* with *decreasing* $N$. This is because the notches formed by the LMS adaptive filter become wider with fewer tap weights, thereby suppressing more RFI *and* more signal. Although this results in a higher value for $\eta$, the signal integrity is adversely affected as well. Therefore $\eta$ is not a good performance indicator for use in finding optimal filter parameters. However, it will be shown in the next section that it can be used to display the relative performance of the filter as it progresses through the image, keeping $N$ constant.

Experience has shown that a value of $N = 256$ is usually more than sufficient to suppress the RFI. Values of $N > 512$ have shown no significant improvement in RFI suppression with the images investigated. In order to avoid signal degradation, $N$ should be larger than 64.

### 4.7.4 Using the same weight vector for many successive range lines

One advantage of using a filter approach to suppress interference as opposed to an estimate-and-subtract approach (see Section 4.2.1) is that a filter approach minimises output *power*, which means that the change in phase of the RF interference from range line to range line is not important and does not require estimation. This opens the possibility of using the same weight-vector across many successive range lines, a method which does, however, rely on the assumption that the RFI itself does not change significantly across successive range lines. As it turns out, such an assumption is often valid. This has also been confirmed by Abend and McCorkle (Abend and McCorkle 1995). It is a reasonable assumption that interference from sources such as radio will be switched on for time durations that span many hundreds, even thousands, of range lines.

Although it is not possible to find the "best" value for $N$ using the quality index defined above, the index can be used to display the relative performance of the
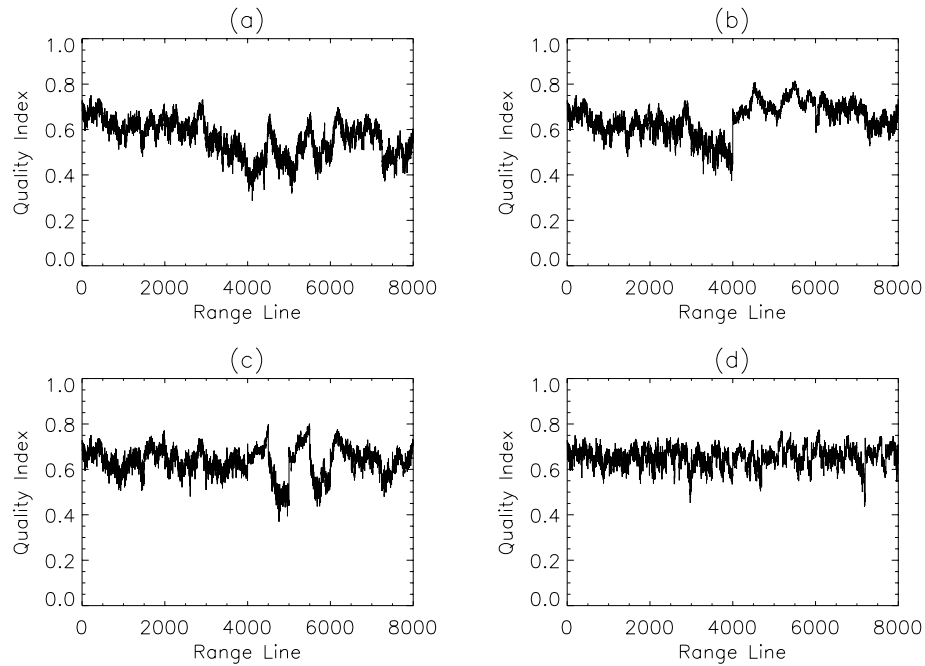
***Figure 4.18:*** *Quality index versus range line. Weight vector is updated (a) only once; (b) every 2000 range lines; (c) every 500 range lines; (d) every 100 range lines.*

filter as it progresses through the image, keeping $N$ constant and calculating $\mu$ as described in Section 4.7.1. Figure 4.18 (a) shows how the quality index $\eta$ changes across 8000 range lines (using the P-band data), when the weight vector is only updated at the first range line. After about 3000 range lines the value of $\eta$ decreases rapidly, indicating that the current weight vector is no longer applicable, probably because the RFI has changed significantly. Figures 4.18 (b), (c) and (d) show how the quality index $\eta$ changes when the weight vector is updated every 2000, 500 and 100 range lines respectively. The second half of Figure 4.18 (c) shows sudden changes in the quality index which might be due to sudden changes in RFI. When updating every 100 range lines, the average value of $\eta$ remains relatively constant, indicating that the filter weight vector is updated at an adequate rate.

## 4.8  Integration with Range-Doppler Algorithm

### 4.8.1  Description

The usual processing sequence is first to suppress the interference in the raw SAR image, and only then to process the cleaned image with a SAR processor. However, it has been shown that the interference suppression stage (implemented with an LMS adaptive filter) can be combined with the range compression stage of the range-Doppler SAR processing algorithm (Lord and Inggs 1999b). This is achieved by multiplying the equivalent transfer function of the interference suppression stage with the transfer function of the range compression stage, thereby creating a new transfer function which implements interference suppression and range compression simultaneously. Assuming that this combined transfer function is valid over many range lines, the only additional computational costs of implementing RFI suppression across those range lines are:

1. The calculation of the equivalent RFI transfer function, and

2. The multiplication of this transfer function by the already existing range compression transfer function.

Experience with P-band and VHF-band SAR data has shown that once the tap weights of the adaptive filter have converged, the same set of tap weights (and therefore the same equivalent RFI transfer function) may effectively be used for up to a few hundred range lines. From experience, a 10-fold increase in the speed of the RFI suppression stage is viable, assuming firstly that the time taken for the filter tap weights to converge and for the combined transfer function to be created is at most equal to the time taken to clean 10 range lines, and secondly that this transfer function will be used for 100 range lines, a number that has yielded good results with the P-band and VHF-band data.

### 4.8.2  RFI transfer function

The equivalent transfer function $H(\omega)$ of the LMS adaptive filter may be obtained once the filter tap weights have converged and are kept constant, making it unnecessary to feed the error signal $e$ back into the adaptive filter. Figure 4.19
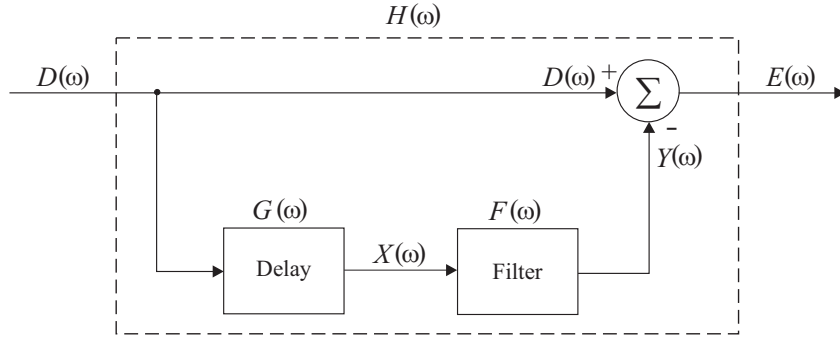
***Figure 4.19:*** *Block diagram of LMS adaptive filter with constant tap weights.*

shows the transfer function block diagram of the LMS adaptive filter with the weights kept constant. In the frequency domain, the output $E(\omega)$ is given by

$$
\begin{aligned}
E(\omega) &= D(\omega) - Y(\omega) && (4.11) \\
&= D(\omega) - F(\omega)\,G(\omega)\,D(\omega) && (4.12) \\
&= D(\omega)\,[1 - F(\omega)\,G(\omega)] && (4.13)
\end{aligned}
$$

Therefore the equivalent transfer function $H(\omega)$ of the RFI suppression stage is given by

$$
H(\omega) = \frac{E(\omega)}{D(\omega)} = 1 - F(\omega)\,G(\omega) \tag{4.14}
$$

where $G(\omega)$ is the transfer function of the time-delay $\Delta$, given by

$$
G(\omega) = e^{-j\omega\Delta} \tag{4.15}
$$

and $F(\omega)$ is the Fourier Transform of the *time-reversed* weight vector $\mathbf{W}$. Since we are dealing with digitised data, $\mathbf{W}$ must be zero-padded to the same length as the range compression transfer function described below.

### 4.8.3  Combined transfer function

Range compression in the frequency domain is accomplished by multiplying the received signal with a matched filter $M(\omega)$, which is typically the complex conjugate of the transmitted pulse spectrum. The combined transfer function $H'(\omega)$ is therefore given by

$$
H'(\omega) = H(\omega)\,M(\omega) \tag{4.16}
$$

This transfer function will simultaneously suppress RFI and perform range compression on the raw SAR image.
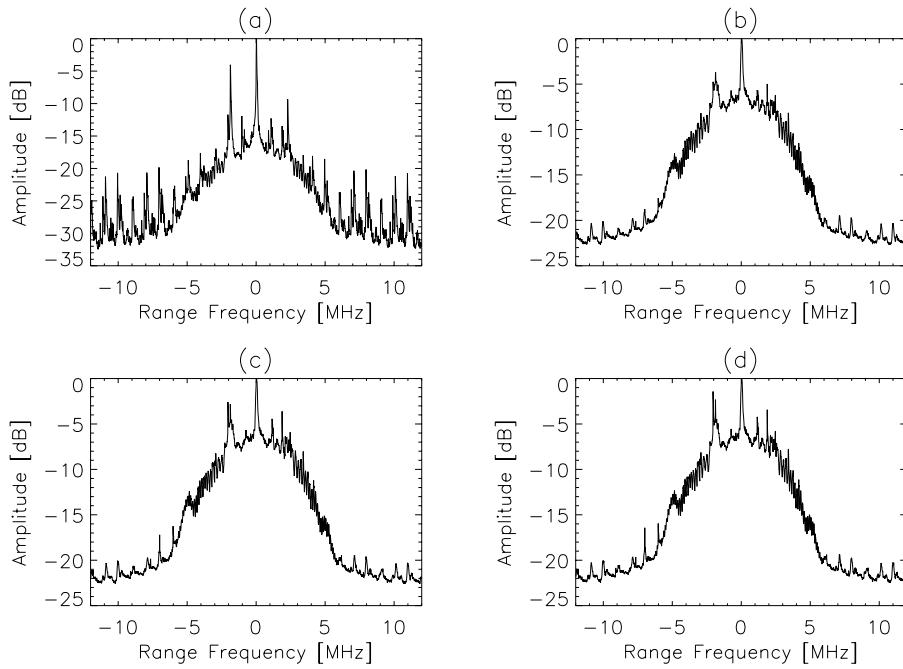
**Figure 4.20:** *Averaged range spectrum of (a) noisy VHF-band image, and of cleaned image with weight vector updated every (b) 100, (c) 500 and (d) 1000 range lines.*

## 4.8.4   VHF-band data results

Figure 4.20 shows the averaged range spectrum of the VHF-band data after cleaning it with a 256-tap filter. The weight vector was updated every 100, 500 and 1000 range lines and the impact on the RFI was assessed for each case. As expected, the RFI suppression decreases as the weight vector update rate is decreased. The images that were obtained with these update rates are shown in Appendix D. Even the image obtained with an update rate of 1000 shows a marked improvement in RFI suppression when compared with the noisy image.

## 4.9  Sidelobe Reduction

### 4.9.1  Description

Any interference suppressing filter will corrupt the desired signal with sidelobes. Abend and McCorkle (Abend and McCorkle 1995) have described a sidelobe reducing procedure which has some similarities to the sidelobe reducing procedure presented here. Figure 4.21 shows a graphical illustration of the technique.

In Figure 4.21 (a) the RFI contaminated signal passes through the LMS adaptive filter $H(\omega)$, yielding a signal free from RFI, but with introduced sidelobes which are asymmetrical. It is assumed that the RFI suppression is done perfectly, so that there is no RFI present in the filtered output. In Figure 4.21 (b), the output from (a) is subtracted from the unfiltered signal, the result of which is passed again through the LMS adaptive filter, yielding a cleaned signal which contains only the (negative) sidelobe. It is assumed that the sidelobe embedded in the RFI
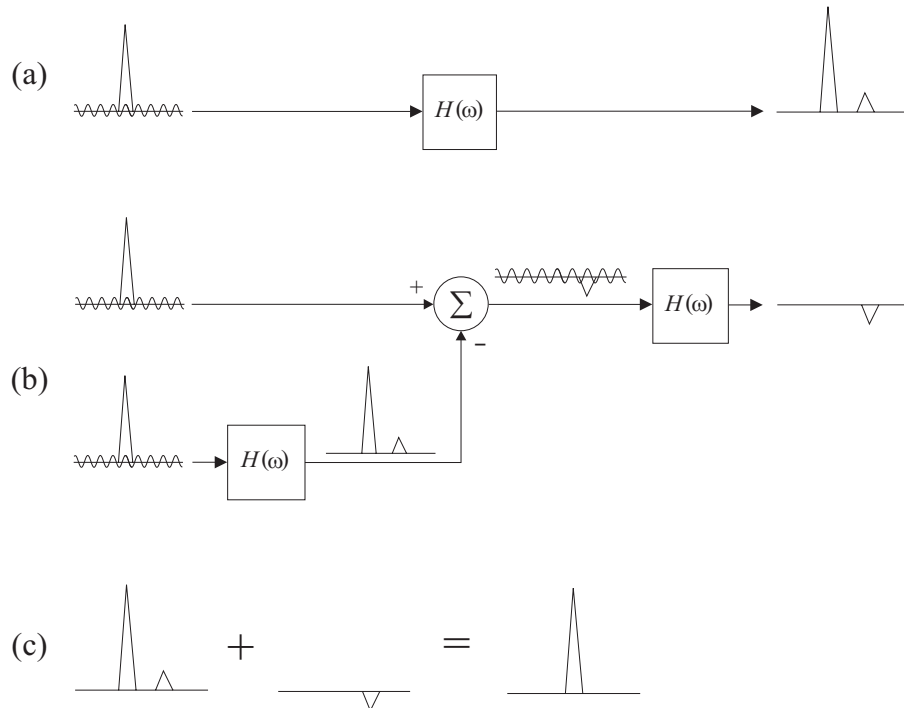


**Figure 4.21:** *Graphical illustration of sidelobe reduction procedure. The large triangle represents the wanted compressed target, the small triangle the unwanted sidelobe, and the sinusoidal waveform the unwanted RFI interference.*
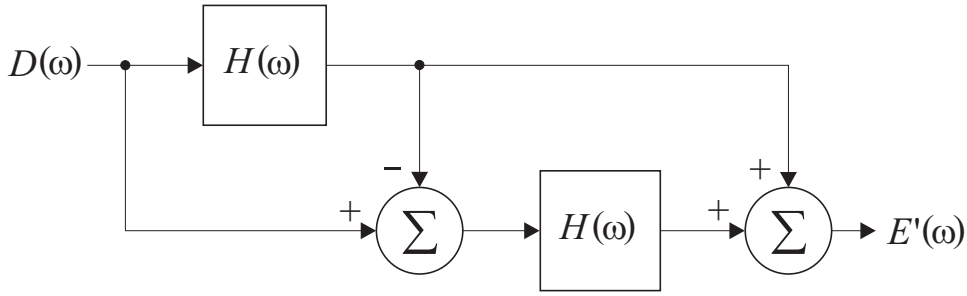
***Figure 4.22:*** *Block diagram of sidelobe reduction procedure.*

is already so small, that the output of the LMS adaptive filter does not contain any sidelobes of the sidelobe (or at least that the magnitude of such a feature is insignificant in comparison with the remaining noise at the filter output). Adding the results of (a) and (b) yields the result shown in Figure 4.21 (c), which is the desired cleaned signal without any sidelobes.

The complete sidelobe reduction procedure is shown in block diagram form in Figure 4.22. In Appendix E it is shown that the overall transfer function is

$$H_{1st}(\omega) = \frac{E'(\omega)}{D(\omega)} = H(\omega)\left[2 - H(\omega)\right] \tag{4.17}$$

The above assumption, that the "sidelobes of the sidelobe" are negligible, is not always valid. If such second-order features are deemed significant, then the same procedure that was described above to suppress the original sidelobe can be used to suppress the "sidelobe of the sidelobe". The overall transfer function of this so-called "second-order" sidelobe reduction procedure is

$$H_{2nd}(\omega) = H(\omega)\left[3 - 3H(\omega) + H(\omega)^2\right] \tag{4.18}$$

and the overall transfer function of the "third-order" sidelobe reduction procedure is

$$H_{3rd}(\omega) = H(\omega)\left[4 - 6H(\omega) + 4H(\omega)^2 - H(\omega)^3\right] \tag{4.19}$$

The derivations of these transfer functions are also given in Appendix E, where an expression which extends them to the general case may be found. The matched filter $M(\omega)$ in Equation 4.16 is now multiplied with $H_{1st}(\omega)$, $H_{2nd}(\omega)$ or $H_{3rd}(\omega)$, instead of $H(\omega)$, thus incorporating the sidelobe reduction procedure, and leading to a very efficient implementation.
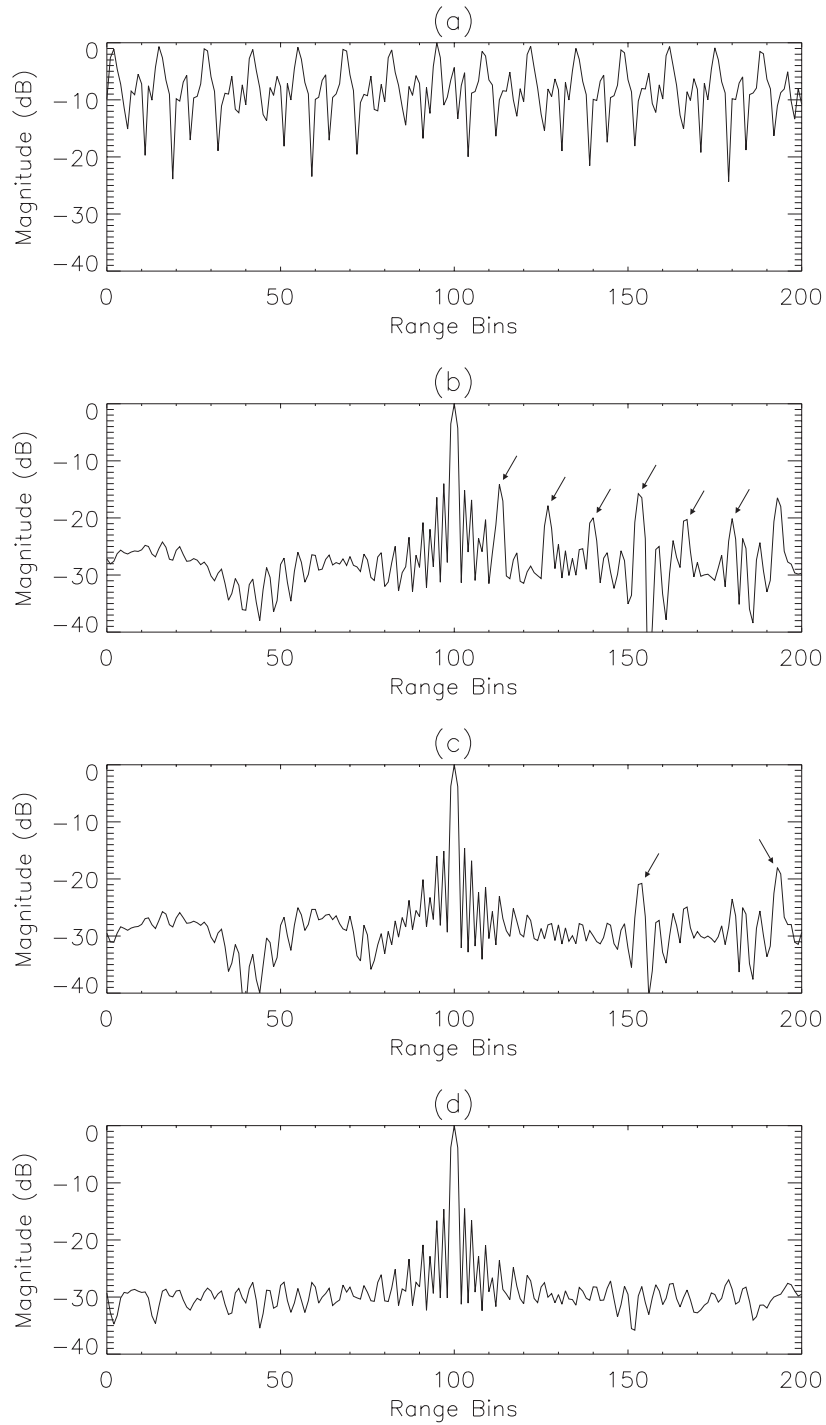
**Figure 4.23:** *Simulation results of sidelobe reduction procedure: (a) RFI contaminated echo return; (b) filtered echo return with no sidelobe reduction (arrows point at unwanted sidelobes); (c) filtered echo return with first-order sidelobe reduction; (d) filtered echo return with second-order sidelobe reduction.*

103

### 4.9.2 Simulation results

Figure 4.23 summarises simulation results which verify the effectiveness of the sidelobe reduction procedure. In Figure 4.23 (a) the range-compressed, RFI contaminated signal is shown. The target is swamped by RFI and cannot be detected. Figure 4.23 (b) shows the result obtained after cleaning the signal, with no sidelobe reduction applied. The arrows in the figure point to clearly visible asymmetric sidelobes. Figure 4.23 (c) and (d) show the cleaned signal with first-order and second-order sidelobe reduction applied respectively. A marked reduction in sidelobe levels is evident.

### 4.9.3 P-band data results

Figure 4.24 (a) displays a zoomed-in portion of the RFI contaminated P-band image. This region contained especially bright targets, which gave rise to unacceptably high sidelobes as depicted in Figure 4.24 (b). After cleaning this image with the third-order sidelobe reduction procedure, the image shown in Figure 4.24 (c) was obtained, which is clearly a vast improvement. However, some of the original interference started appearing again. Thus the original RFI suppression capability of the filter is compromised by applying the sidelobe reduction procedure. The sidelobe reduction order to use depends on the brightness of the target. Since the targets displayed in Figure 4.24 were exceptionally bright, the "sidelobes of the sidelobe" were still clearly visible after applying the first-order sidelobe reduction procedure. The best results were obtained using the third-order sidelobe reduction procedure.

### 4.9.4 VHF-band data results

Figure 4.25 (a) displays a zoomed-in portion of the VHF-band image after it has been cleaned without any sidelobe reduction. Figure 4.25 (b) shows the same image after it has been cleaned with a first-order sidelobe reduction procedure. Again there is a definite improvement in sidelobe levels visible. Applying higher order sidelobe reduction did not yield any better results.

Experience has shown that applying the sidelobe reduction technique sometimes reduces the RFI suppression capability of the filter. It is therefore important to keep the rate at which the filter weights are updated as small as possible, in order to maximise the amount of RFI suppression.
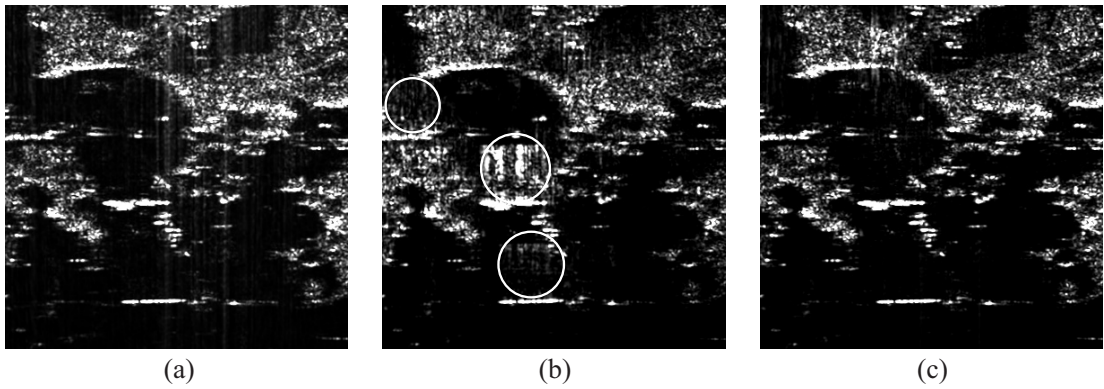
**Figure 4.24:** *P-band data results of sidelobe reduction procedure: (a) RFI contaminated image; (b) filtered image without any sidelobe reduction (the circles indicate regions with very high sidelobes); (c) filtered image with third-order sidelobe reduction.*
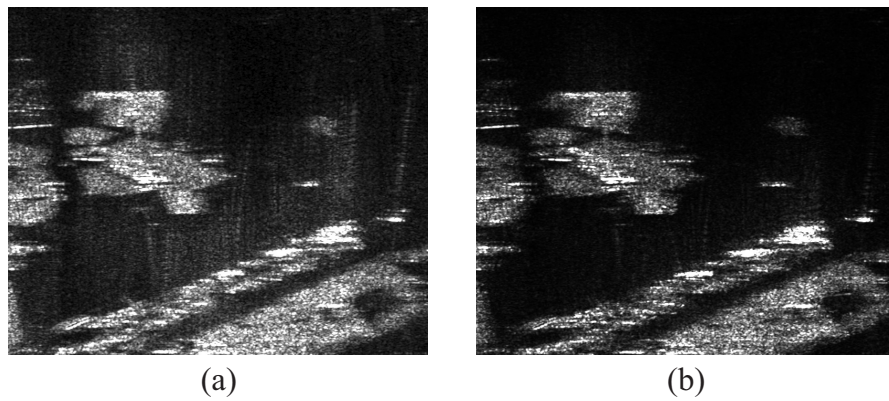


**Figure 4.25:** *VHF-band data results of sidelobe reduction procedure: (a) filtered image without any sidelobe reduction; (b) filtered image with first-order sidelobe reduction.*

## 4.10 Conclusions

Both the notch filter and the LMS adaptive filter have been applied successfully on real P-band data and on real VHF-band data which contained RFI. A remarkable improvement in image quality was apparent in all cases. A median filter has been applied to the averaged range spectrum in order to obtain an approximation for the signal spectrum envelope, which was then used by the notch filter to identify and remove interference spikes. It was described how the notch filter could be integrated with the range-Doppler algorithm, leading to an efficient implementation of the notch filter.

The issue of finding optimal filter parameters for the LMS adaptive filter was discussed. Although the quality index defined in Section 4.7.2 could not be used to find the optimum number of filter tap weights, it was used successfully to give an indication of the number of successive range lines over which the same filter tap weights could be used.

The LMS adaptive filter was re-written in terms of its equivalent transfer function, which facilitated efficient integration with the range-Doppler algorithm. Furthermore, a technique was described for reducing range sidelobes, which arise as an unwanted by-product of the RFI suppression stage. It was shown that the interference suppression and the sidelobe reduction can be integrated with the range-compression stage of the range-Doppler algorithm, thereby resulting in a very efficient implementation.

# Chapter 5

# Conclusions and Scope for Future Research

## 5.1 Conclusions

The objectives of this thesis have been the investigation of the following two aspects of low-frequency (VHF/UHF) SAR processing:

1. The use of stepped-frequency waveforms to synthesise larger total bandwidths and therefore higher range resolution, and

2. Radio frequency interference (RFI) suppression.

Three methods have been described for processing the stepped-frequency data, namely an IFFT method, a time-domain method and a frequency-domain method. Both the IFFT method and the time-domain method have been found to be unsuitable for SAR processing applications. The IFFT method suffers from spillover of energy into consecutive coarse range bins, which leads to the appearance of "ghost targets" in the resulting high-resolution range profile. The time-domain method, although not producing any "ghost targets" in the high-resolution range profile, is computationally inefficient because of the upsampling requirement of the narrowband pulses before applying the frequency shift.

These considerations have led to the development of a frequency-domain method, which efficiently uses all of the information in the narrowband pulses to obtain

a high-resolution range profile which does not contain any "ghost targets". The execution of the signal processing steps is fast, when compared to the time-domain implementation, since only FFTs and phase multiplications are required, and no upsampling of the narrow-bandwidth pulses is necessary. This method does, however, rely on the proper construction of a compression filter, whose function it is to compress the data if it has not already been range-compressed, and also to compensate for amplitude "ripples" at the subspectra boundaries. If these ripples are not properly compensated, repeating target artefacts become visible in the time-domain range profile.

This method has been shown to be very flexible. Both the step size and the transmit bandwidths may vary from pulse to pulse within a burst of pulses. It has therefore been proposed to make use of this property to avoid transmitting pulses in spectral regions that have been identified as containing large amounts of interference. Instead of simply omitting a frequency step which would be heavily contaminated with RFI, the spectral notches can be made suitably small so as to notch out as little of the spectrum as possible.

RFI has been shown to be a major problem for SAR systems operating at VHF/UHF frequencies, since the interference power is often many dB stronger than the received signal power, thereby causing receiver saturation. Stepped-frequency waveforms alleviate the problem of receiver saturation, firstly by notching out spectral regions containing the most dominant interfering sources, and secondly by allowing the A/D converters to sample with a larger number of bits, since they need only to sample the instantaneous narrowband pulses. Sampling with a larger number of bits increases the receiver dynamic range, which reduces the problem of receiver saturation.

Virtually the whole VHF/UHF spectrum is already in use by other services such as radio, TV and fixed/mobile communications. It is therefore impossible to avoid all the spectral regions containing RFI, and therefore other RFI suppression approaches need to be employed to suppress the remaining RFI in the received data. Various RFI suppression methods have been investigated. However, only the notch filter and the LMS adaptive filter have been implemented and applied on real P-band data obtained from the E-SAR system of the DLR, and on real VHF-band data obtained from the SASAR system.

The notch filter is perhaps the most intuitive approach for the suppression of RFI, since the interference, which shows up as narrowband spikes in the frequency-domain, is simply notched out. A median filter has been employed to obtain an approximation of the signal spectrum envelope, which was then used by the notch filter to identify and remove interference spikes. The notch filter was efficiently integrated with the range-compression stage of the range-Doppler SAR processing algorithm. The LMS adaptive filter was implemented because it received favourable review in the literature. Both methods significantly suppressed the RFI in the real images investigated. In particular, the cleaned VHF images showed detail that was not visible prior to RFI suppression.

Work done on finding optimal filter parameters for the LMS adaptive filter proved useful for estimating the number of range lines upon which the LMS adaptive filter could operate *without* adaptively changing the filter tap weights. It was found that the filter tap weights were often valid for several hundred range lines, and this facilitated the re-writing of the LMS adaptive filter in terms of an equivalent transfer function, which was then integrated with the range-compression stage of the range-Doppler SAR processing algorithm. Since the range-compression and the interference suppression could then be performed simultaneously, and since the equivalent transfer function of the RFI suppression stage is often effective for hundreds of range lines, large computational savings could be achieved.

A technique was derived to suppress the unwanted sidelobes that may be produced by the LMS adaptive filter. This method could also be written in terms of the equivalent transfer function of the LMS adaptive filter, and this allowed the sidelobe suppression technique to be integrated with the range-compression stage of the range-Doppler processor. It was found, however, that the sidelobe suppression technique compromised the LMS adaptive filter's ability to suppress RFI, and therefore the weights had to be updated more frequently. Nevertheless, significant computational savings could still be achieved.

## 5.2  Future Work

Scope for future work includes:

- Investigating the implications of upgrading a single frequency radar system to a stepped-frequency system in more detail. More work needs to be carried out on a systems level to calculate the costs involved when upgrading such a radar system.

- Investigating the issues of more accurate motion compensation and azimuth compression for widebeam, ultra-wideband, airborne, strip-map SAR. Possible advantages of applying motion compensation to narrowband stepped-frequency waveforms need to be investigated.

- Comparing the computational efficiency of the IFFT method, the time-domain method and the frequency-domain method of processing stepped-frequency data. Although the time-domain technique has been shown to be inefficient compared to the frequency-domain technique, more work could be conducted to quantify this statement.

- Investigating the use of a logarithmic low-noise amplifier. This could allow the increase of the receiver dynamic range without the need to increase the number of bits of the A/D converter. The correction of this non-linearity could be performed before the SAR processing, or before the re-combination of the sub-bands.

- Investigating backscatter-free data in more detail. Backscatter-free data can be obtained either by switching the transmitter off completely, or by recording the pre-nadir return, which entails starting the data recording process before the transmitted pulse has returned to the receiver. The SASAR system has already obtained backscatter-free data using both of these methods. In particular the pre-nadir return data could prove useful for RFI suppression, since the RFI in the pre-nadir return data would be very similar to the RFI in the remainder of the range line containing backscatter data.

- Investigating the calibration degradation of the implemented RFI suppression technique. If the V-polarisation and H-polarisation RFI signals are different, the polarimetric calibration accuracy will also be degraded.

- Investigating the effect of tapering notches on mainlobe width and sidelobe levels. In Section 4.5.2 it has been mentioned that the notches in the frequency-domain have been tapered in order to reduce time-domain sidelobes. However, more work could be conducted to show the effects of various degrees of tapering.

- Optimising the filter parameters of the LMS adaptive filter. This topic has already been addressed in Chapter 4, but more work could be conducted to investigate adaptively changing the parameters of the filter (such as the number of tap weights or the convergence factor) as it sweeps through the image.

- Investigating the problem of RFI suppression by making use of information theory. The two methods implemented in this thesis, namely the notch filter and the LMS adaptive filter, could be classified as *adhoc* approaches, which do not efficiently use *all* of the information that is contained in the RFI contaminated images. This would require more work to be conducted in analysing the characteristics of the interference, such as frequency spacing, bandwidth, polarisation, etc. This issue is currently being addressed by the candidate at UCT.

- Development of more quantified methods to evaluate the performance of RFI suppression techniques.

- Obtaining data from different sensors at different frequencies. Since the RFI encountered at different frequencies can be very different, one would have to investigate data at different centre frequencies in order to develop a strategy for automatically suppressing RFI in various scenarios.

# Appendix A

# IFFT Method Simulation Results

This appendix lists the point target simulation results of the IFFT method for producing synthetic range profiles from stepped-frequency data. Refer to Section 2.5.2 for a discussion regarding these results.

Table A.1 lists the relevant parameters for each simulation. These parameters were chosen to correspond with the VHF-band SASAR system, which has a centre frequency $f_c = 141\,\text{MHz}$ and which transmits linear FM chirps with a pulse length of $T_p = 10\,\mu\text{s}$ and a bandwidth of $B_t = 12\,\text{MHz}$ sampled at $f_{ad} = 24\,\text{MHz}$. Therefore, for every simulation, $n = 4$ narrowband pulses were transmitted with $B_{tx} = 12\,\text{MHz}$, $T_p = 10\,\mu\text{s}$ and a combined centre frequency of $f_c' = 141\,\text{MHz}$, which is the average between the first centre frequency and the last centre frequency. Note therefore that the first centre frequency of the simulations shown in Figures A.4 and A.6 are different from those of the other simulations due to the different frequency step size.

The pulses were range-compressed before applying the IFFT. The theoretical resolution for the narrowband pulses is given by $\rho_r = \frac{cK_r}{2B_{tx}} = 11.1\,\text{m}$, with $K_r = 0.89$ for rectangular window weighting. The percentage overlap between SRPs of successive coarse range bins is given by Equation 2.16.

Each figure in this appendix shows the following graphs:

(a) Magnitude of range-compressed target return, first frequency step.

(b) Nine coarse range bins centred around the peak of the target return shown in (a). The complex data has been upsampled (using a Shannon interpolator) by a factor of 100.

(c) A dB plot of the entire synthetic range profile, with appropriate overlapping of range profiles of neighbouring coarse range bins.

(d) Magnitude plot of a zoomed-in portion of the region centred around the peak of the synthetic range profile. The complex data has been upsampled by a factor of 100. The range extent shown here is the same as that shown in (b), in order to illustrate the increase in range resolution.

| | Fig. A.1 | Fig. A.2 | Fig. A.3 | Fig. A.4 | Fig. A.5 | Fig. A.6 |
|---|---|---|---|---|---|---|
| $f_0$ [MHz] | 123 | 123 | 123 | 132 | 123 | 132 |
| $\Delta f$ [MHz] | 12 | 12 | 12 | 6 | 12 | 6 |
| $f_{ad}$ [MHz] | 12 | 12 | 12 | 12 | 24 | 24 |
| $w_s$ [m] | 12.5 | 12.5 | 12.5 | 25.0 | 12.5 | 25.0 |
| Bin spacing [m] | 12.5 | 12.5 | 12.5 | 12.5 | 6.25 | 6.25 |
| % overlap | none | none | none | 50 % | 50 % | 75 % |
| Number of targets | 1 | 2 | 2 | 1 | 1 | 1 |

**Table A.1:** *Stepped-frequency simulation parameters of IFFT method.*
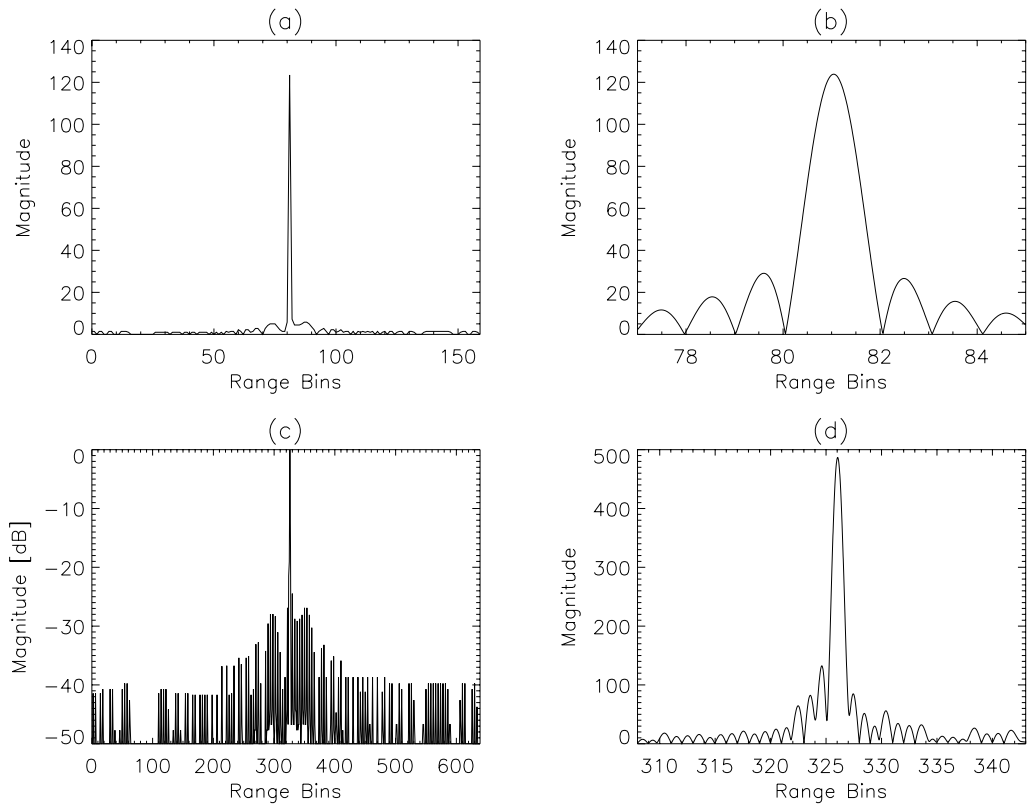
***Figure A.1:*** *Simulation result of IFFT method, with no overlap between successive SRPs. See beginning of appendix for details.*

Figure A.1 shows the simulation of a single point target. There is no overlap between successive range profiles. Comparing Figures A.1 (b) and (d), the fourfold increase in range resolution can be observed.
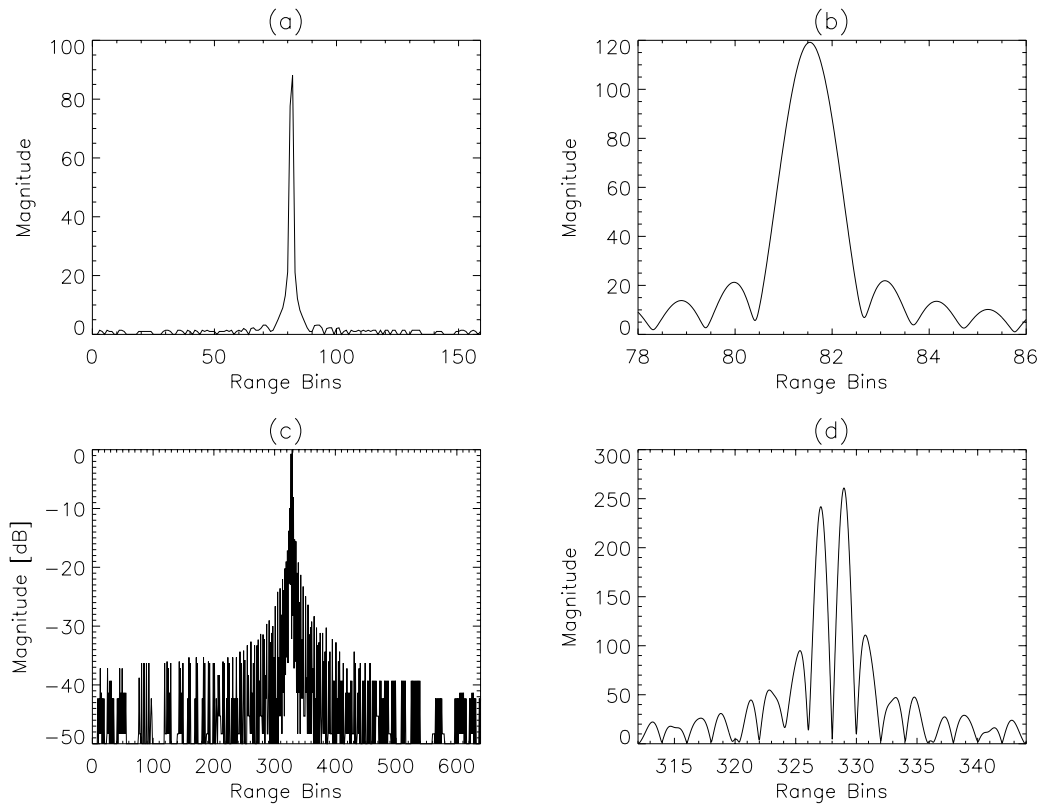
***Figure A.2:*** *Simulation result of IFFT method, showing the return from 2 point targets, which are both positioned in one coarse range bin. See beginning of appendix for details.*

Figure A.2 shows the same simulation as Figure A.1. However, the return from 2 point targets is measured. The point targets are spaced 6 m apart, which is less than the 11.1 m resolution associated with each narrowband pulse, and therefore Figure A.2 (b) appears to show only one point target. Furthermore, both targets were centred in one coarse range bin. After IFFT processing, the two point targets are clearly visible, as can be seen in Figure A.2 (d). Note that the sidelobes have increased, compared to the previous simulation. This can be attributed to signal energy leaking into neighbouring coarse range bins.

116
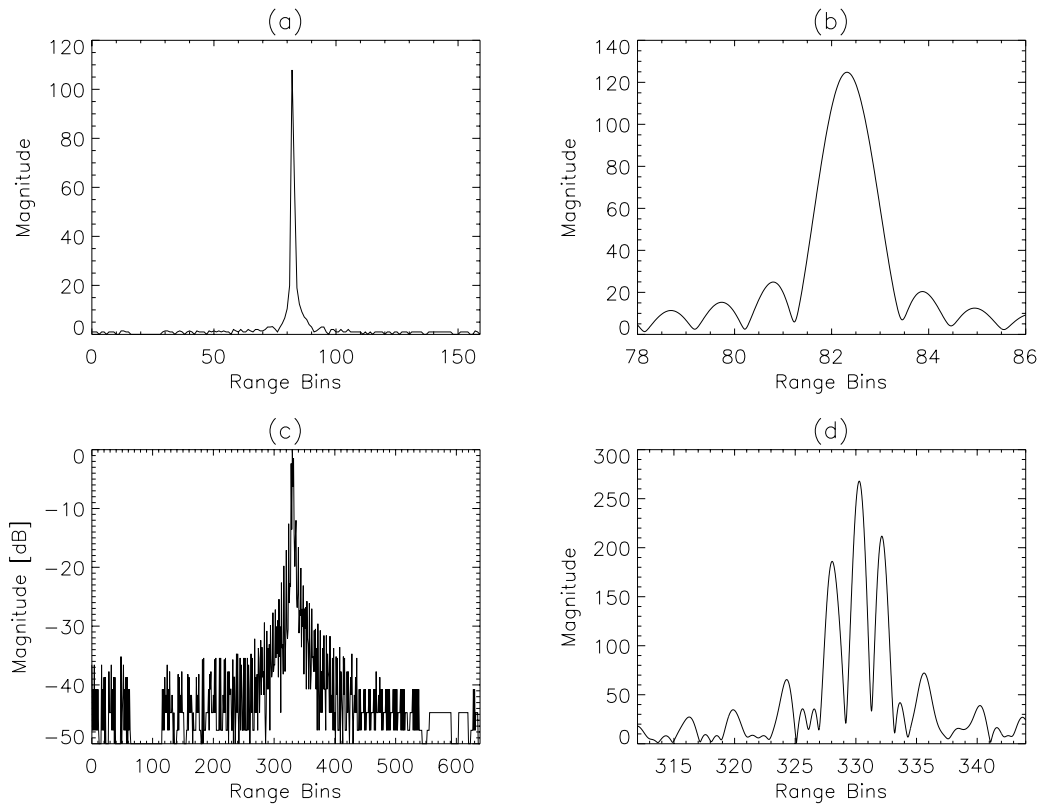
**_Figure A.3:_** _Simulation result of IFFT method, with the 2 point targets being positioned in neighbouring coarse range bins. See beginning of appendix for details._

Figure A.3 shows the same simulation as Figure A.2. However, now the two point targets are positioned in neighbouring *coarse* range bins. From Figure A.3 (d) it appears as though *three* point targets are present. This is because the signal energy of the first point target is nearly equally divided between two neighbouring coarse range bins, whereas most of the signal energy from the second point target is contained in only one coarse range bin.
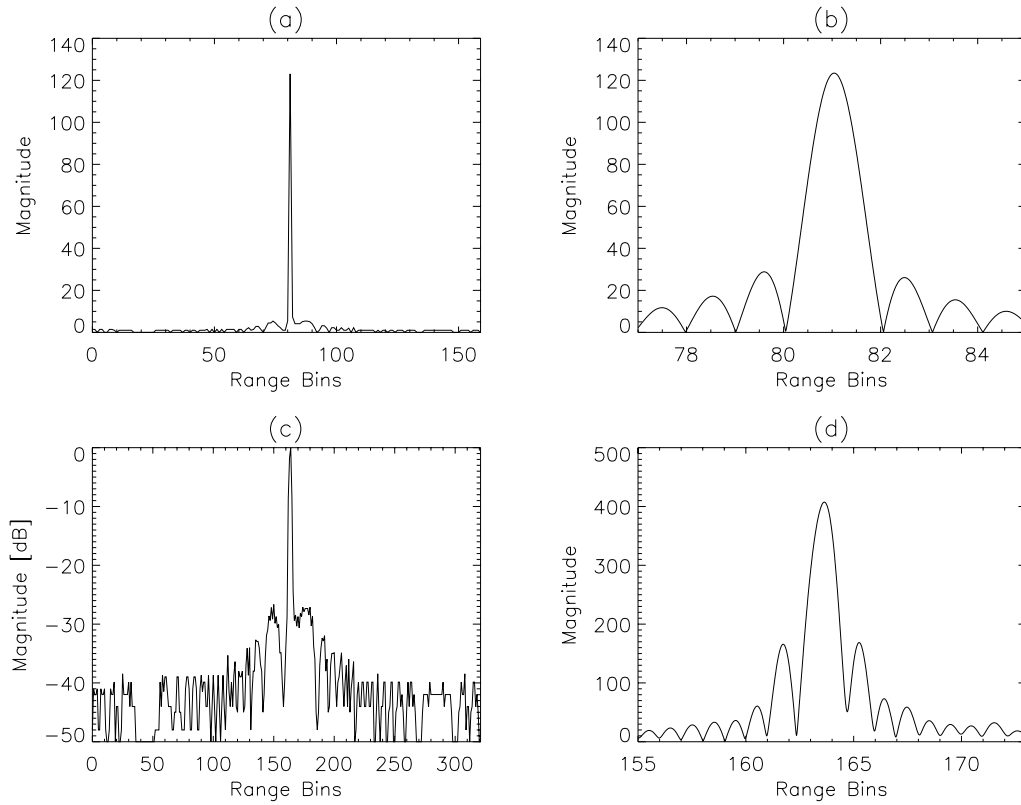
**Figure A.4:** *Simulation result of IFFT method, where the frequency step size $\Delta f$ is equal to half the transmitted bandwidth $B_{tx}$. See beginning of appendix for details.*

Figure A.4 shows a simulation where $\Delta f = \frac{1}{2}B_{tx}$, and therefore the synthetic range length is doubled, which means that successive range profiles associated with the coarse range bins overlap by 50 %. Note that the synthetic range resolution has halved, and therefore the mainlobe width measured in Figure A.4 (d) is twice as wide as that measured in Figure A.1 (d).

118
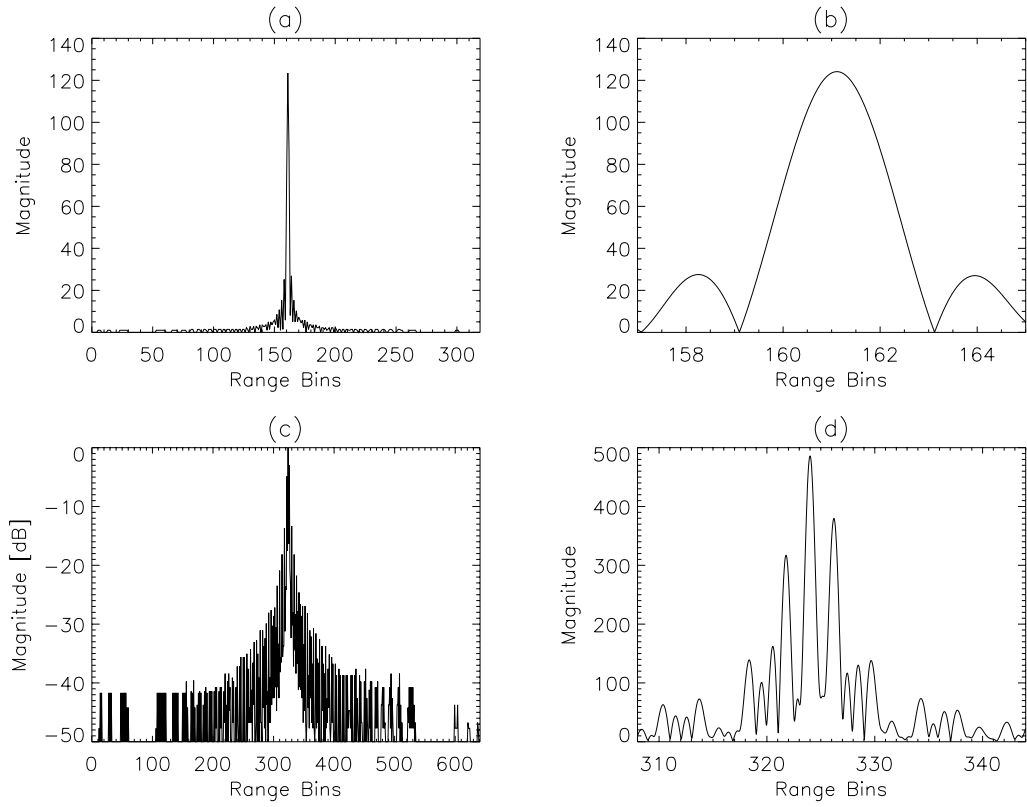
***Figure A.5:*** *Simulation result of IFFT method, where the sample frequency $f_{ad}$ is equal to twice the transmitted bandwidth $B_{tx}$. See beginning of appendix for details.*

Figure A.5 shows a simulation where $f_{ad} = 2B_{tx}$. The synthetic range length is still the same. However, the coarse range bins are sampled at twice the rate, causing successive range profiles to overlap by 50 %. Since the target energy is now spread over more than one coarse range bin, there are repeated artefacts of the target in the combined range profile.
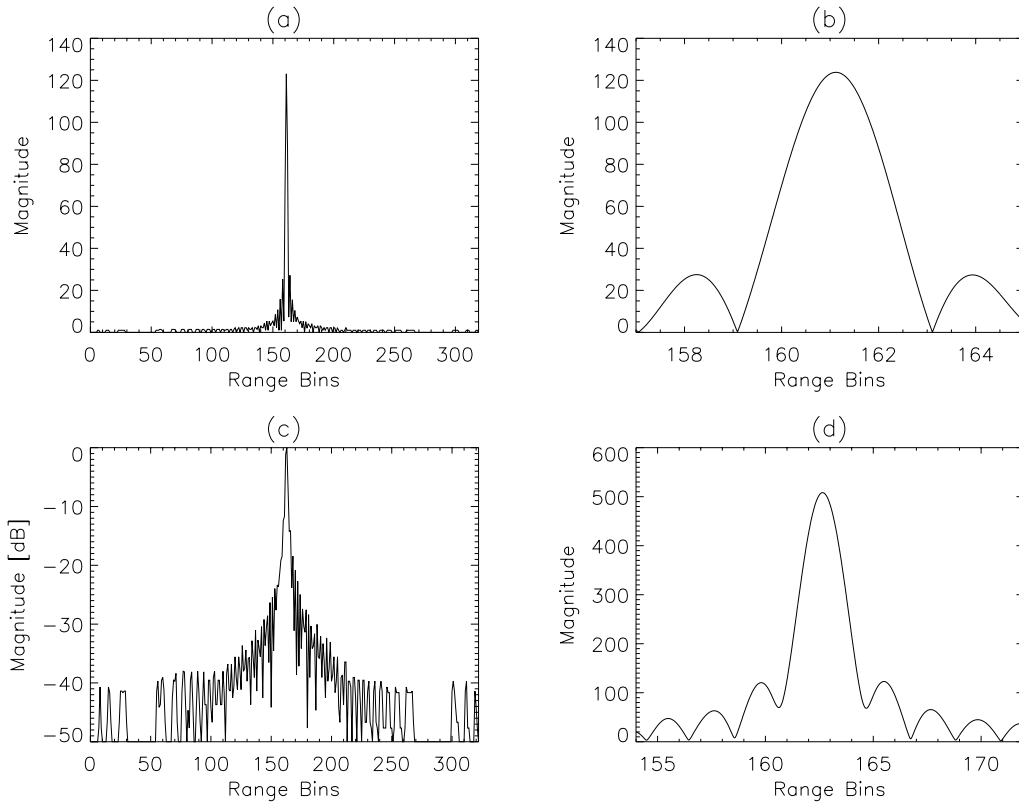
**Figure A.6:** *Simulation result of IFFT method, where the frequency step size $\Delta f$ is equal to half the transmitted bandwidth $B_{tx}$, and the sample frequency $f_{ad}$ is equal to twice the transmitted bandwidth $B_{tx}$. See beginning of appendix for details.*

Figure A.6 shows a simulation where $\Delta f = \frac{1}{2}B_{tx}$ and $f_{ad} = 2B_{tx}$, causing successive range profiles to overlap by 75 %. No repeated target artefacts can be seen as in the previous simulation. However, it has been observed that performing this simulation with two point targets in neighbouring range bins, as in Figure A.3, also produces range profiles displaying three point targets.

# Appendix B

# Synthetic Range Profiles of Aircraft

This appendix shows high-resolution synthetic range profiles of aircraft, which have been obtained using the IFFT method and the spectrum reconstruction method. All profiles have been upsampled by a factor of 20, in order to facilitate better comparison between the profiles obtained from the two methods.

The two graphs in the top row (refer to Figures B.1–B.4) show a zoomed-in portion of the entire high-resolution synthetic range profile. For the IFFT method, this is the synthetic range profile (SRP) obtained when taking an inverse FFT across all frequency steps in the range bin containing the peak value. For all examples shown in this appendix, the profiles obtained from the two methods look very similar.

The two graphs in the bottom row (refer to Figures B.1–B.4) show a larger portion of the entire high-resolution synthetic range profile, in order to expose "ghost targets" adjacent to the main target. For the IFFT method, this portion represents three consecutive SRPs, which have been obtained by taking an inverse FFT across all frequency steps in the range bin containing the peak value, and in the range bins adjacent to the bin containing the peak value. For all examples shown in this appendix, the "ghost targets" of the IFFT method are much more significant than those of the spectrum reconstruction method.

Further discussions concerning these graphs are given in Section 3.7 of Chapter 3.
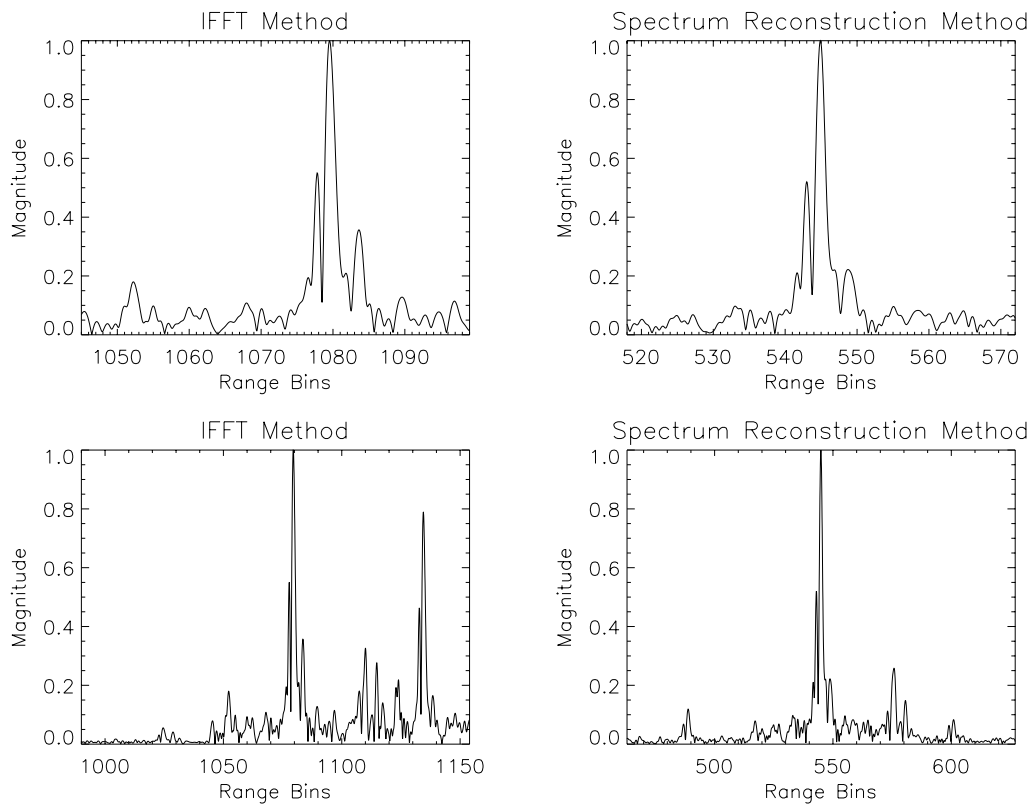
**Figure B.1:** *High-resolution range profile of a 747 aircraft, processed with the IFFT method and the spectrum reconstruction method.*
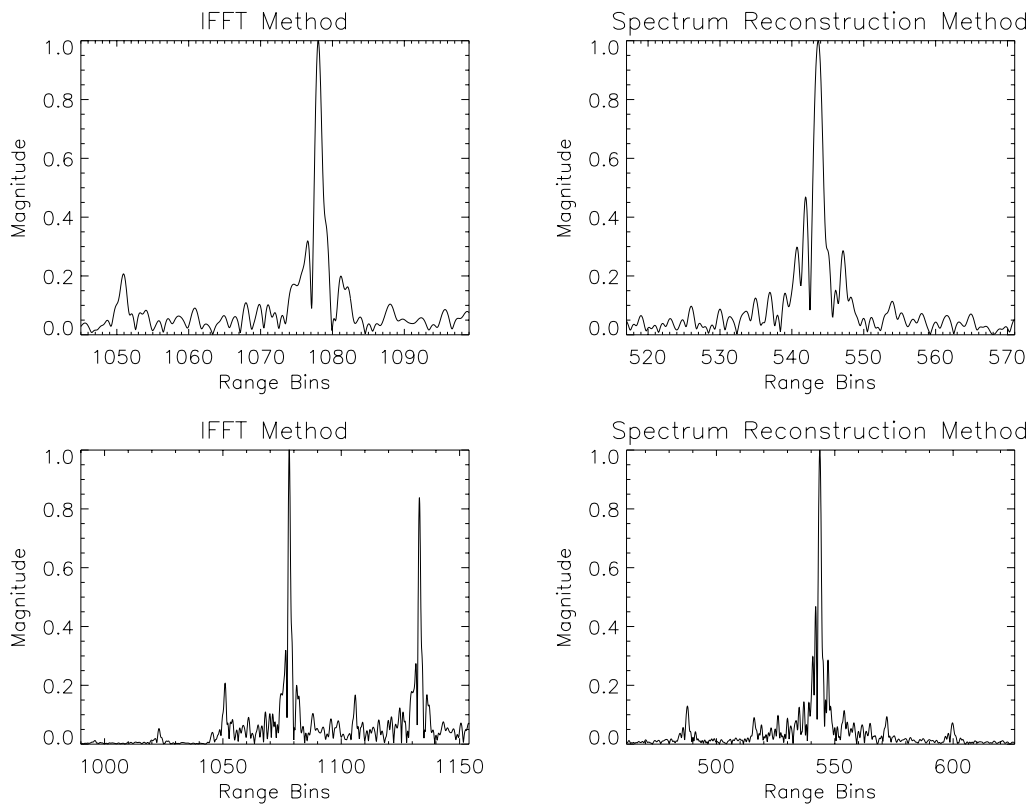
***Figure B.2:*** *High-resolution range profile of an N326 aircraft, processed with the IFFT method and the spectrum reconstruction method.*
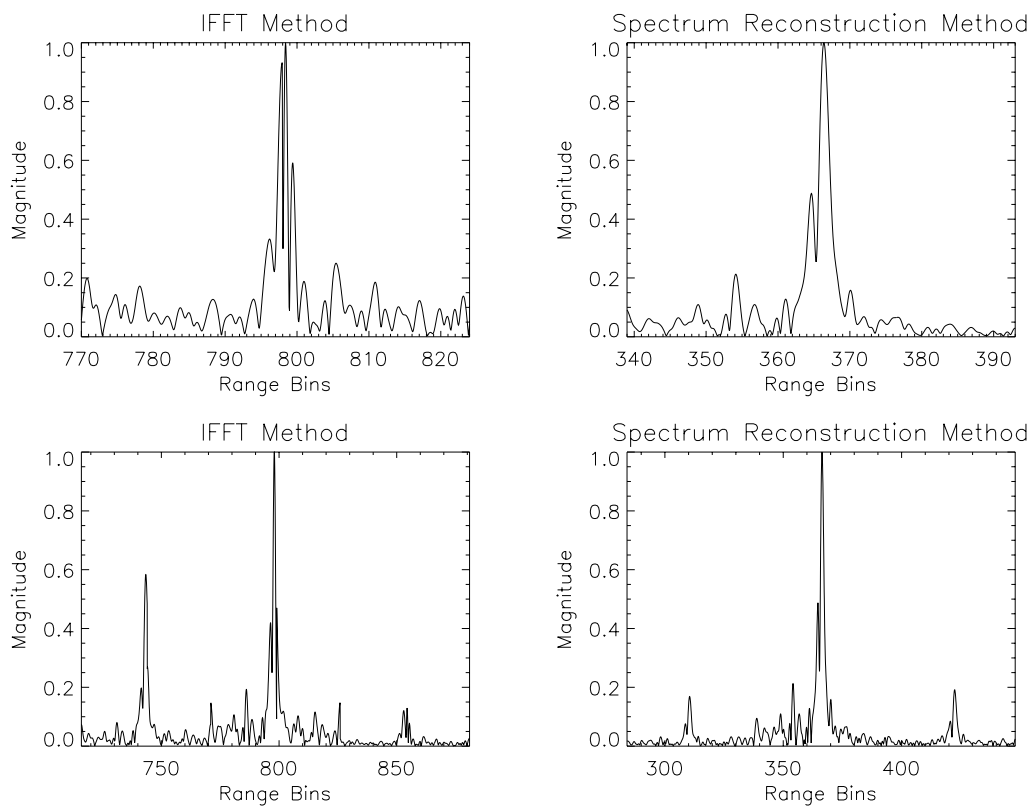
***Figure B.3:*** *High-resolution range profile of a King Air B200 aircraft, processed with the IFFT method and the spectrum reconstruction method.*

124
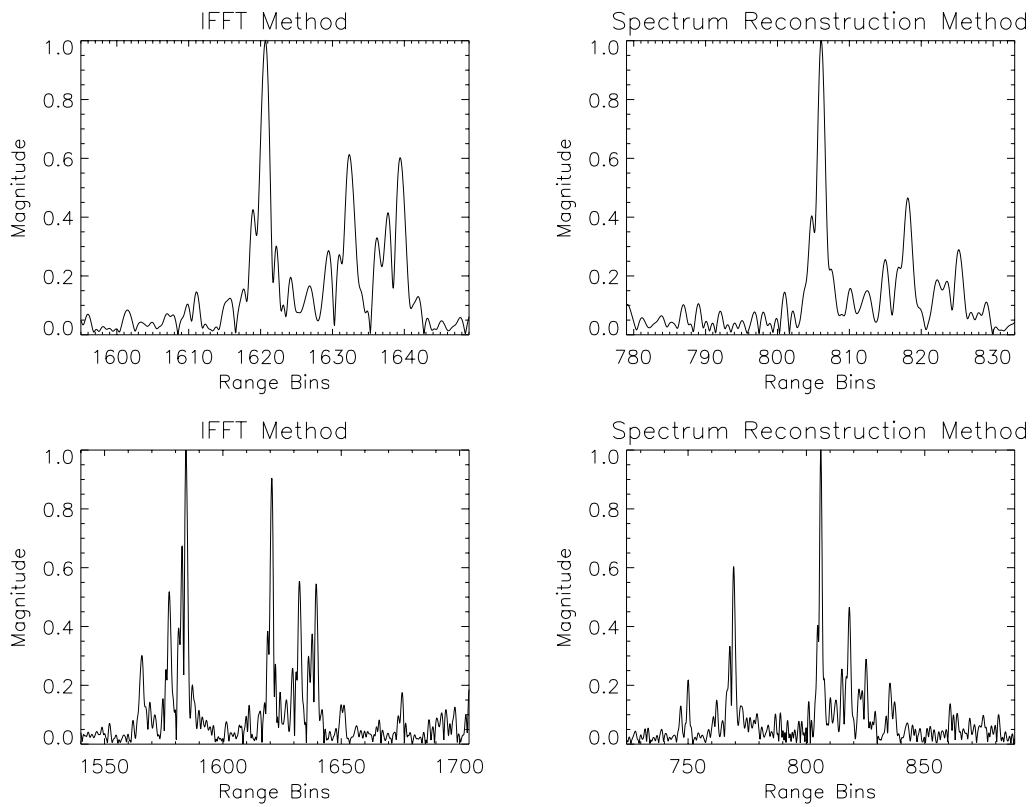
***Figure B.4:*** *High-resolution range profile of a Messer Bolkow aircraft, processed with the IFFT method and the spectrum reconstruction method.*

# Appendix C

# First SASAR Interferometry Results

This appendix shows the first interferometry results that were obtained from the SASAR system. The raw images were processed by Jasper Horrell (RRSG, UCT) with the G2 range-Doppler processor, and the interferometric processing was done by Andrew Wilkinson (RRSG, UCT). These results are included in this thesis in order to demonstrate the importance of suppressing RFI for interferometric processing.

The relevant parameters of the two images used to produce the interferogram are listed in Table C.1. A vertical baseline was flown, with a spacing of about 100 m. The results shown in this appendix are very preliminary. Improvements to the image registration algorithm should improve the results. In addition, most of the Upington scene is not well suited to VHF interferometry due to the extremely low backscatter from the flat, unvegetated desert surrounds.

|  | Image 1 | Image 2 |
|---|---|---|
| Centre frequency | 141 MHz | 141 MHz |
| Bandwidth | 12 MHz | 12 MHz |
| Range resolution | 12.5 m | 12.5 m |
| Azimuth resolution | 5.0 m | 5.0 m |
| Approximate height above ground | 2850 m | 2740 m |

***Table C.1:*** *Parameters of SASAR interferometric data.*

Figure C.3 shows the correlation image that was formed from the two images shown in Figures C.1 and C.2. These images were first cleaned with a notch filter. The correlation image shows a high degree of coherence (about 0.90) in the top left-hand corner. Generally the town areas and fences provide the regions of highest coherence. Fringes are clearly visible in the top left-hand area in the interferogram shown in Figure C.5, which is a zoomed-in portion of the interferogram shown in Figure C.4. The fringes are not parallel to the flight path, which runs along the bottom of the image, because the flight paths were not parallel to each other and this effect has not been corrected here. Figure C.6 shows the flattened interferogram obtained after removing the flat earth component. Interesting phase fringes can now be observed, which are hopefully related to the region's topography. More work needs to be done to interpret these fringes correctly.

The RFI contaminated images are shown in Figures C.7 and C.8, and the resulting correlation image is shown in Figure C.9. It contains bright lines in the range direction, which correspond to the RF interference, which is many dB stronger than the signal. However, there is no apparent signal correlation between the two images. No fringes are detectable in the interferogram shown in Figure C.10, nor in the enlarged interferogram of Figure C.11, or in the flattened interferogram shown in Figure C.12. This verifies the importance of suppressing RFI when doing interferometric processing.

More recent interferometric results from the SASAR system are shown in Figures C.13 to C.16. Figure C.13 shows two cleaned magnitude images of the Hermanus area near the Southern Cape in South Africa, separated by a vertical baseline of about $100\,\mathrm{m}$. Figure C.14 shows the relevant correlation image. A high degree of coherence is visible, corresponding to the bright regions of the magnitude images. Figures C.15 and C.16 show the interferogram and flattened interferogram respectively. When comparing the flattened interferogram with the magnitude images, a correlation between the fringe pattern and the region's topography is already apparent. However, more work needs to be conducted with the generation and interpretation of these interferograms.
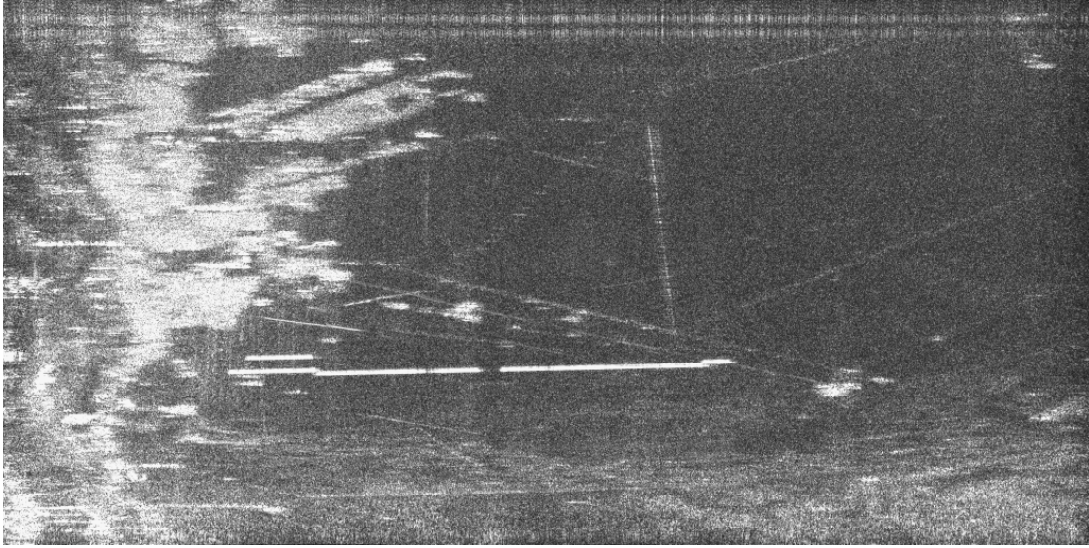
**Figure C.1:** *Cleaned image 1 of Upington area.*
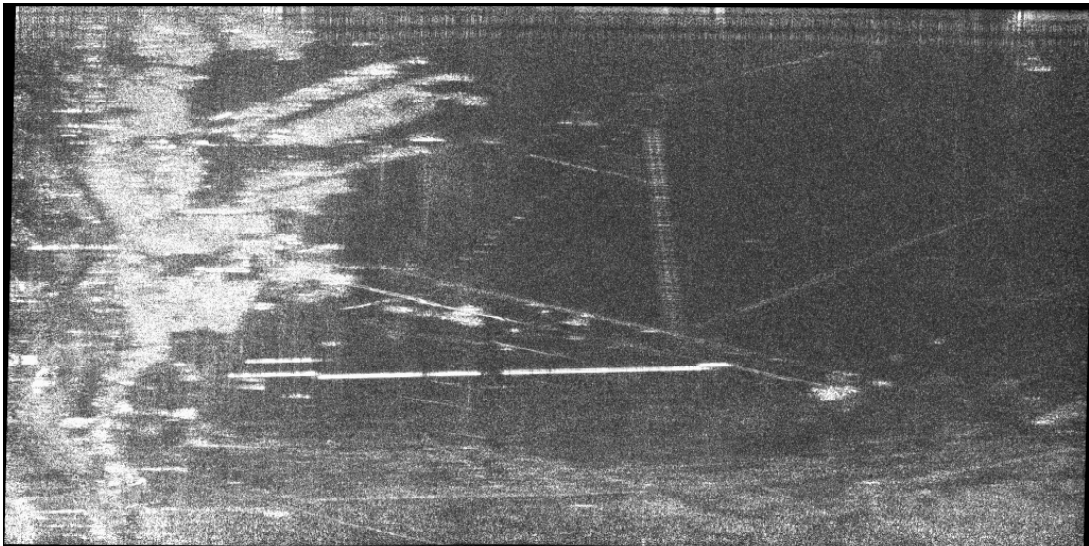


**Figure C.2:** *Cleaned image 2 of Upington area.*
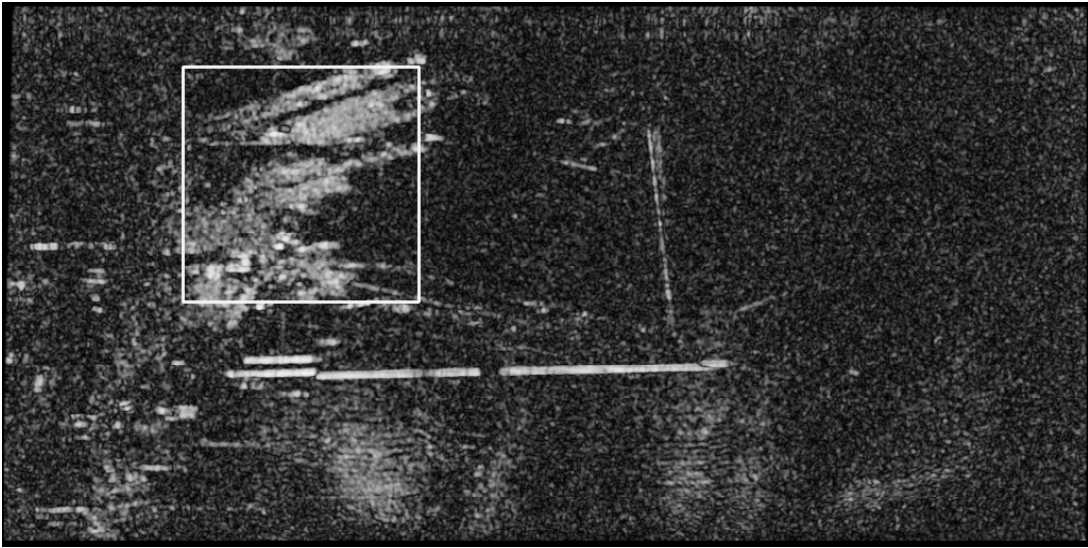
**Figure C.3:** *Correlation image of cleaned datasets.*



**Figure C.4:** *Interferogram of cleaned datasets.*
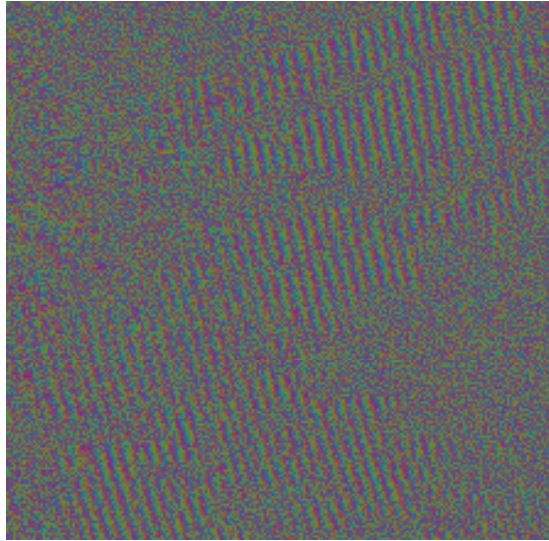
**_Figure C.5:_** _Zoomed-in portion of interferogram, clearly showing fringes._
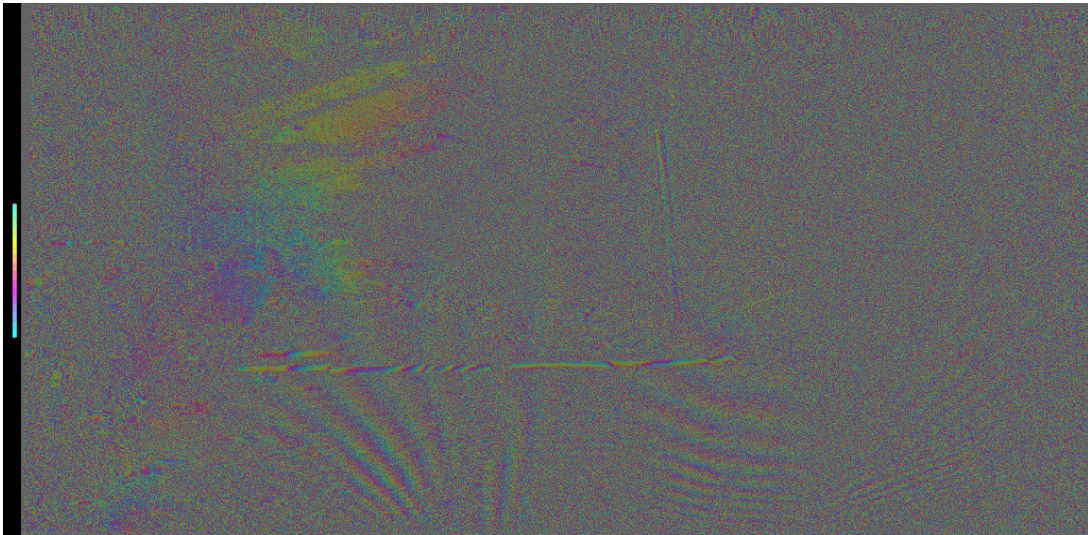


**_Figure C.6:_** _Flattened interferogram of cleaned datasets._

**Figure C.7:** *Noisy image 1 of Upington area.*
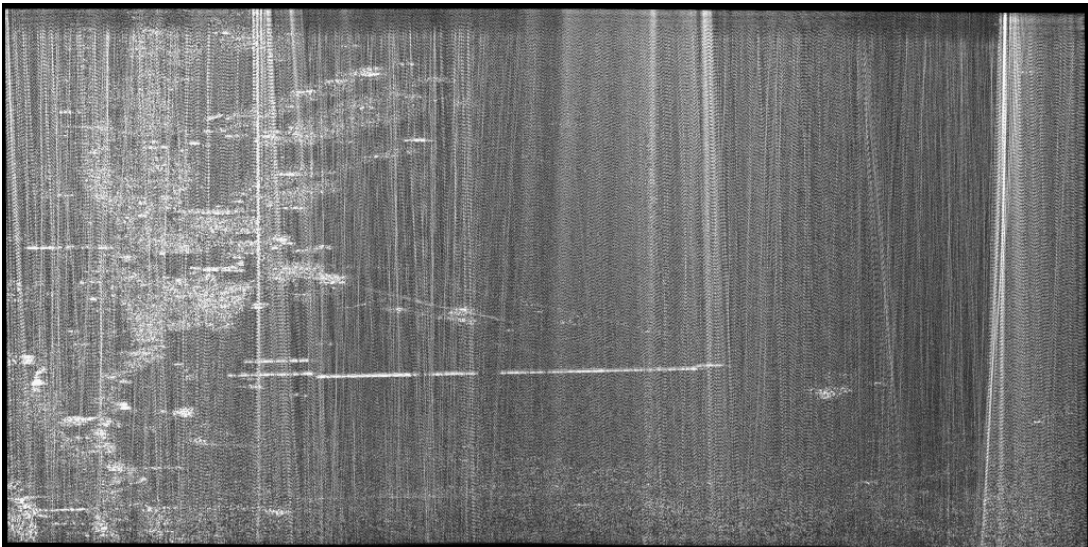


**Figure C.8:** *Noisy image 2 of Upington area.*
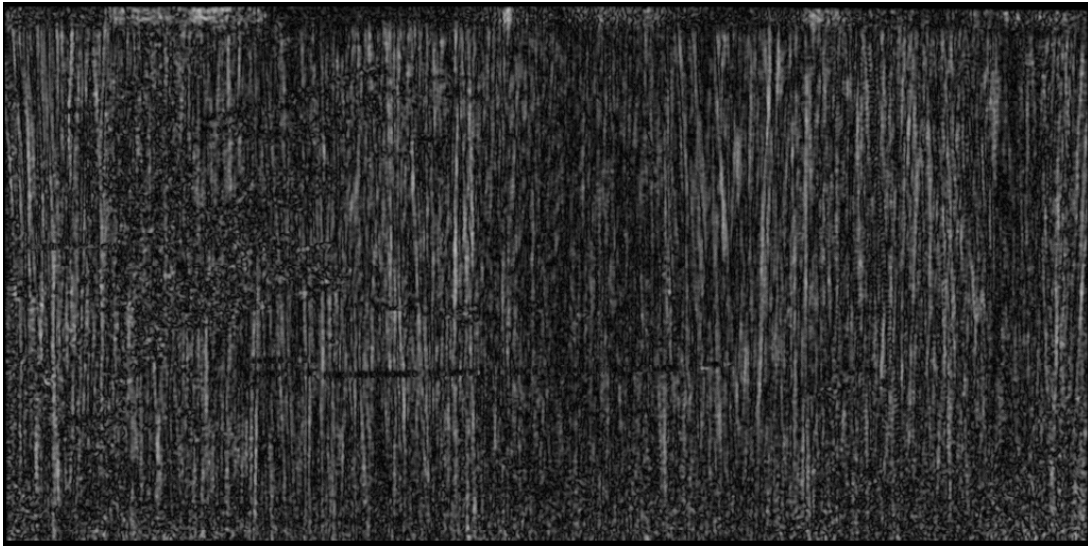
**Figure C.9:** *Correlation image of noisy datasets.*
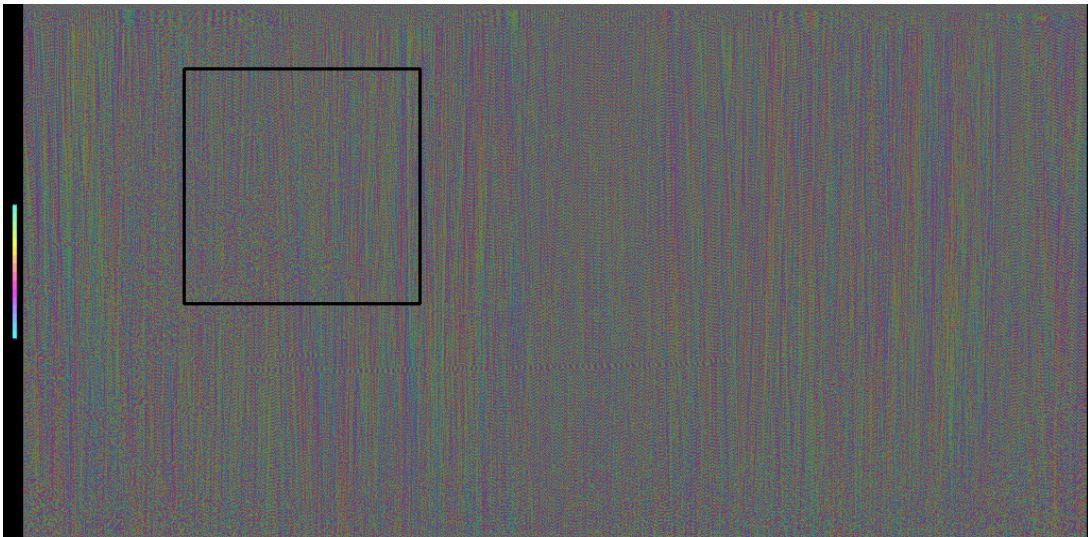


**Figure C.10:** *Interferogram of noisy datasets.*
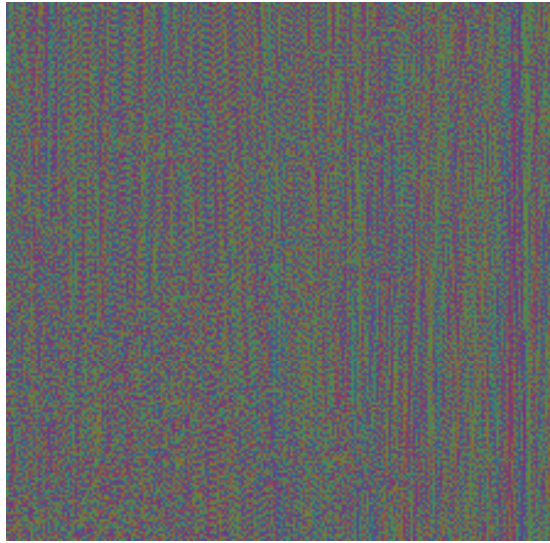
**Figure C.11:** *Zoomed-in portion of interferogram obtained from noisy images. No fringes are visible.*
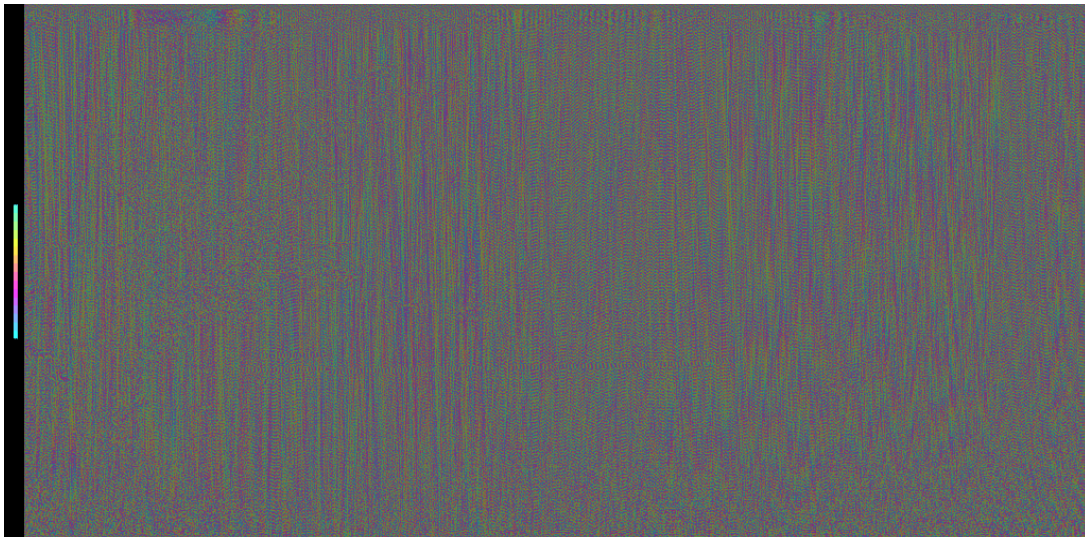


**Figure C.12:** *Flattened interferogram of noisy datasets.*
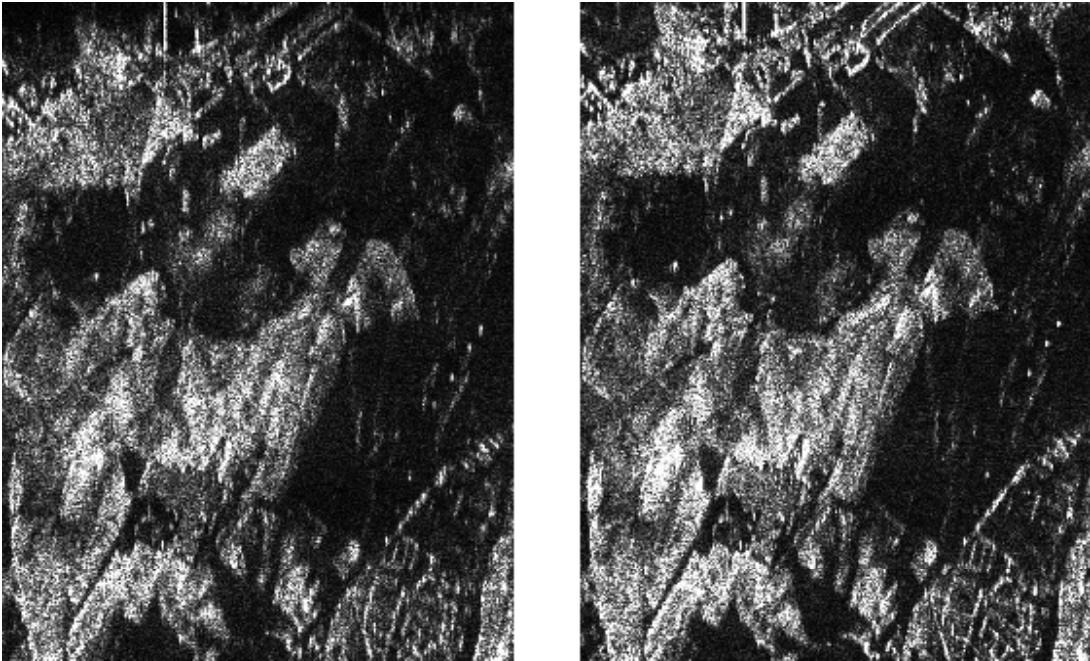
**Figure C.13:** *Cleaned magnitude images of Hermanus area, separated by a vertical baseline of 100 m.*



**Figure C.14:** *Correlation image formed from the two processed images of the Hermanus area.*
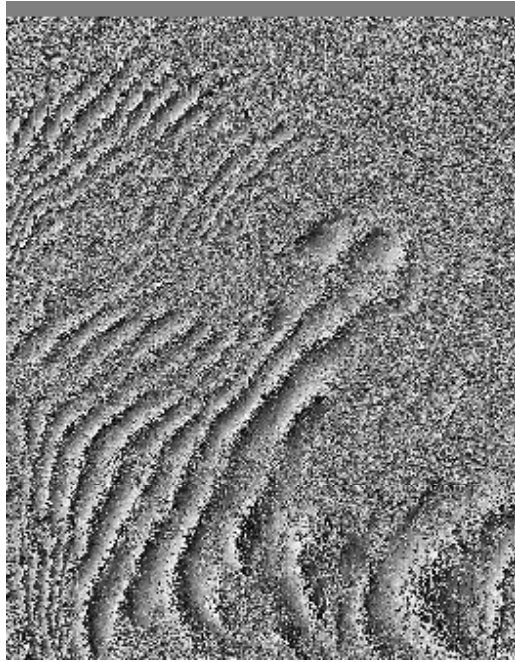
**Figure C.15:** *Interferogram of Hermanus area, with fringes clearly visible.*
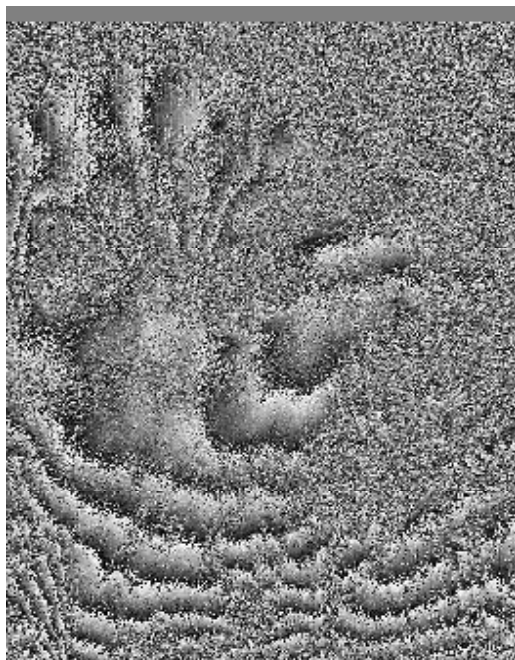


**Figure C.16:** *Flattened interferogram of Hermanus area.*

# Appendix D

# Effect of Varying Weight Vector Update Rate

This appendix shows the following images:

- VHF-band image of Upington, contaminated with RFI (Figure D.1),

- Cleaned image, using the LMS adaptive filter, with filter weights updated every 100 range lines (Figure D.2),

- Cleaned image, using the LMS adaptive filter, with filter weights updated every 500 range lines (Figure D.3), and

- Cleaned image, using the LMS adaptive filter, with filter weights updated every 1000 range lines (Figure D.4).

The averaged range spectra of these images are shown in Figure 4.20 in Section 4.8.4.
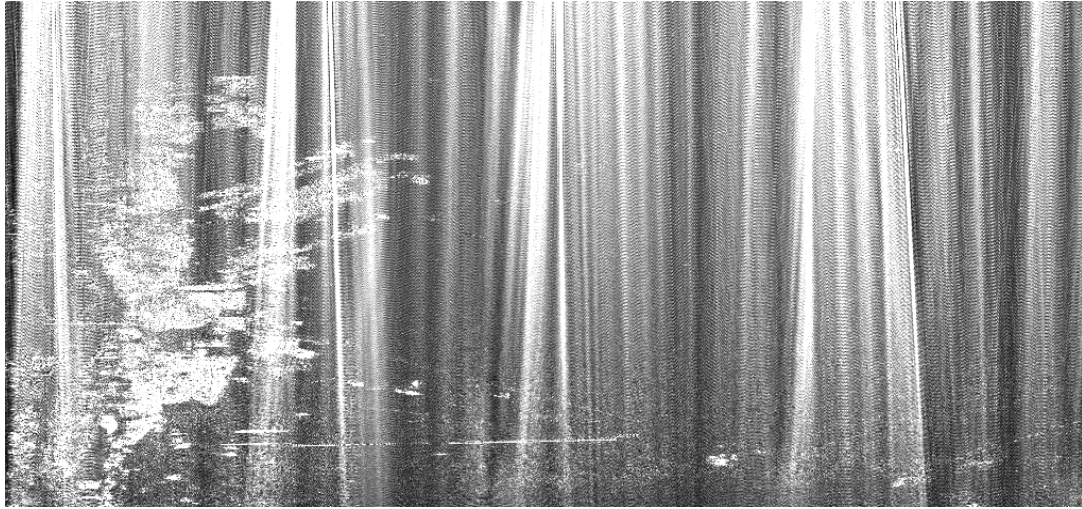
**Figure D.1:** *VHF-band image with RFI.*
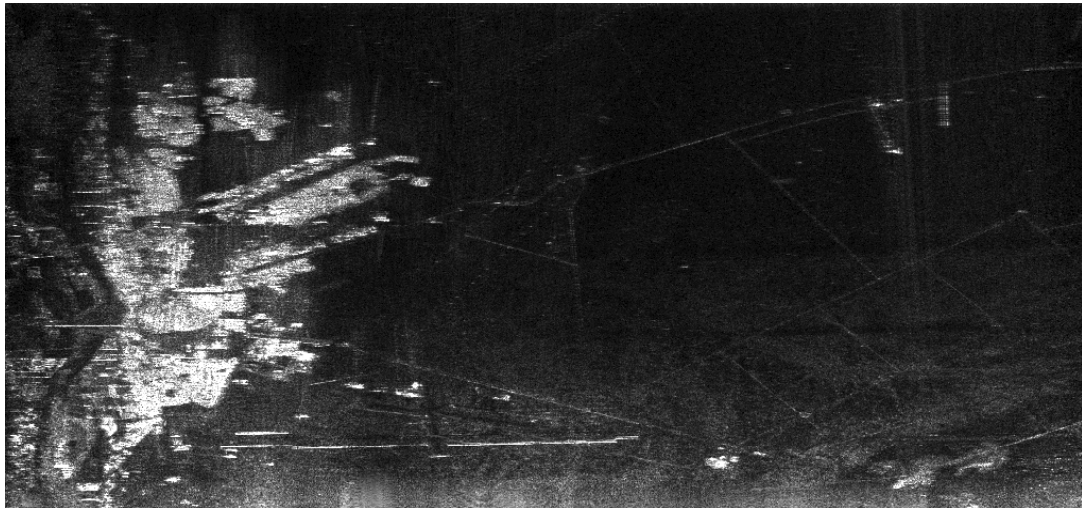


**Figure D.2:** *Cleaned image with weights updated every 100 range lines.*
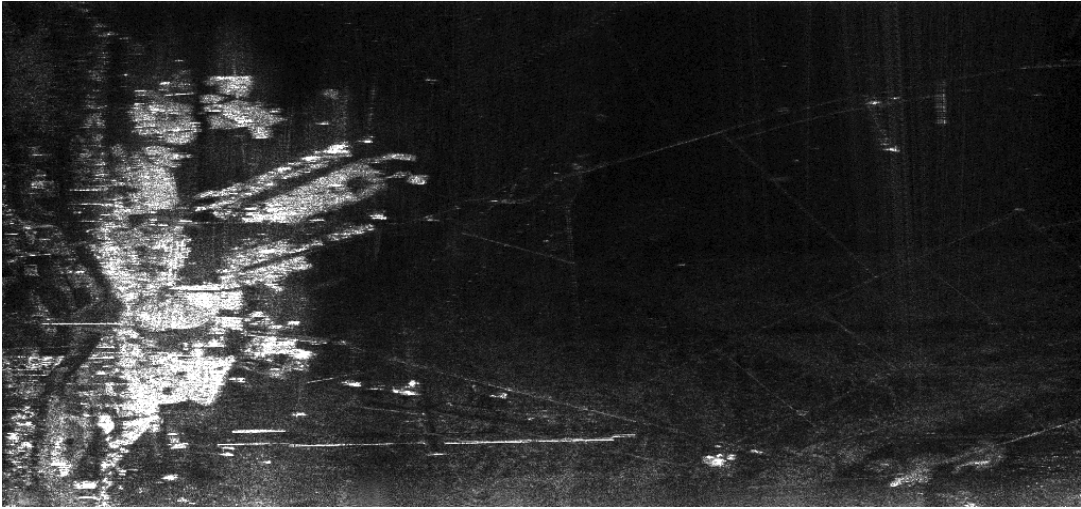
**Figure D.3:** *Cleaned image with weights updated every 500 range lines.*
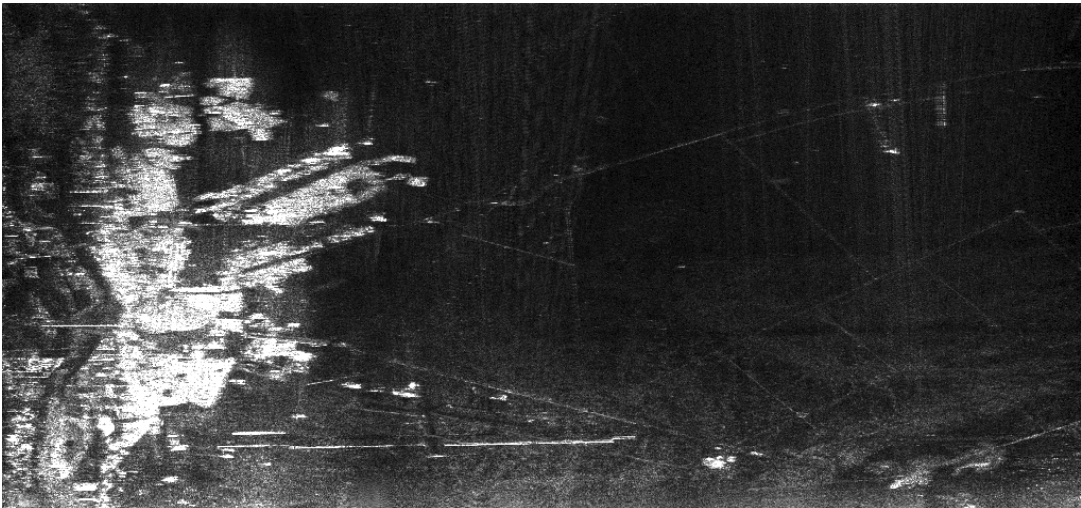


**Figure D.4:** *Cleaned image with weights updated every 1000 range lines.*

# Appendix E

# Sidelobe Reduction Transfer Function

This appendix shows the derivations of the sidelobe reduction transfer functions mentioned in Section 4.9. Although all of the signals and transfer functions mentioned in this appendix are functions of $\omega$, the $(\omega)$ symbol has been omitted in Equations E.1, E.3 and E.5 for reasons of neatness and readability. The following variables apply in this appendix:

- $D(\omega)$ is the RFI contaminated signal;

- $E(\omega)$ is the cleaned output of the sidelobe reduction filter;

- $H(\omega)$ is the equivalent transfer function of the cleaning filter;

- $H_{1st}(\omega)$, $H_{2nd}(\omega)$ and $H_{3rd}(\omega)$ are the derived transfer functions of the first-, second- and third-order sidelobe reduction filters respectively;

- $A$, $B$ and $C$ are internal signals in the transfer function diagrams.

## E.1   First-Order Sidelobe Reduction

Figure E.1 shows the block diagram of the first-order sidelobe reduction transfer function. Signal $B$ contains the (negative) sidelobe embedded in RFI (refer to Figure 4.21 (b)), and it is assumed that this sidelobe is sufficiently small, so that
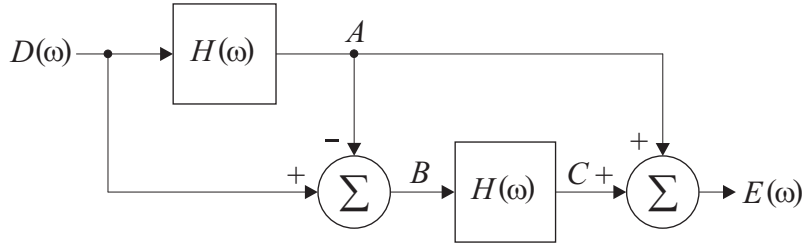
**Figure E.1:** *First-order sidelobe reduction transfer function.*

signal $C$ does not contain any "sidelobes of the sidelobe", after signal $B$ has passed through the cleaning filter $H(\omega)$.

From Figure E.1,

$$
\begin{aligned}
E &= A + C \\
&= A + BH \\
&= DH + (D - DH)\,H \\
&= D\left(2H - H^2\right) \qquad\qquad\qquad\qquad \text{(E.1)}
\end{aligned}
$$

Therefore the first-order transfer function is given by:

$$
\begin{aligned}
H_{1st}(\omega) &= \frac{E(\omega)}{D(\omega)} \\
&= H(\omega)\,[2 - H(\omega)] \qquad\qquad\qquad \text{(E.2)}
\end{aligned}
$$
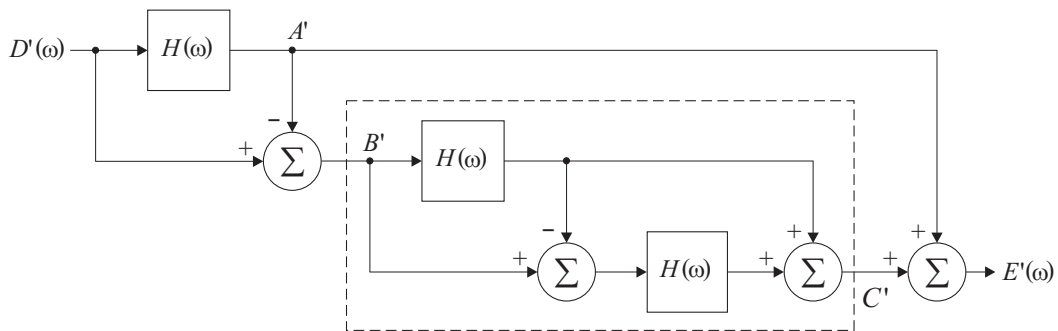


**Figure E.2:** *Second-order sidelobe reduction transfer function.*

142

## E.2  Second-Order Sidelobe Reduction

Figure E.2 shows the block diagram of the second-order sidelobe reduction transfer function. With the first-order filter the assumption was made that the sidelobe contained in signal $B$ was sufficiently small, so that signal $C$ did not contain any "sidelobes of the sidelobe." If this assumption is not valid, then instead of passing signal $B$ through the cleaning filter $H(\omega)$, it can be passed through the first-order sidelobe reduction filter $H_{1st}(\omega)$. The dashed box in Figure E.2 is therefore identical to the first-order transfer function shown in Figure E.1.

From Figure E.2,

$$
\begin{aligned}
E' & = A' + C' \\
& = A' + B' H_{1st} \\
& = A' + (D' - D'H) H_{1st} \\
& = A' + (D' - D'H) \left(2H - H^2\right) \\
& = D'H + 2D'H - 2D'H^2 - D'H^2 + D'H^3 \\
& = D'H \left(3 - 3H + H^2\right)
\end{aligned}
\tag{E.3}
$$

Therefore the second-order transfer function is given by:

$$
\begin{aligned}
H_{2nd}(\omega) & = \frac{E'(\omega)}{D'(\omega)} \\
& = H(\omega) \left[3 - 3H(\omega) + H(\omega)^2\right]
\end{aligned}
\tag{E.4}
$$

## E.3  Third-Order Sidelobe Reduction

Figure E.3 shows the block diagram of the third-order sidelobe reduction transfer function. If the result obtained from the second-order transfer function is still not satisfactory, then the dashed box shown in Figure E.3 may be replaced with the second-order sidelobe reduction filter $H_{2nd}(\omega)$. This procedure may, in theory, be continued indefinitely. However, as has been noted in Section 4.9, the interference suppression capability of the filter is compromised by applying this sidelobe reduction procedure.
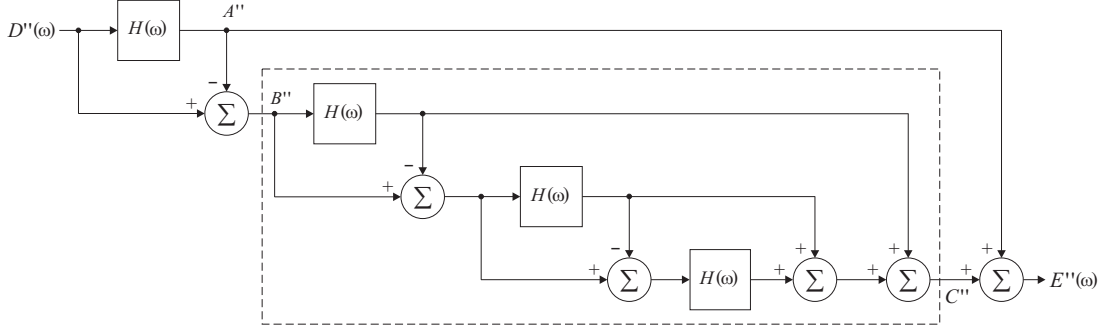
**Figure E.3:** *Third-order sidelobe reduction transfer function.*

From Figure E.3,

$$
\begin{aligned}
E'' &= A'' + C'' \\
&= A'' + B'' H_{2nd} \\
&= A'' + (D'' - D''H)\, H_{2nd} \\
&= A'' + (D'' - D''H)\, \left(3H - 3H^2 + H^3\right) \\
&= D''H + 3D''H - 3D''H^2 + D''H^3 - 3D''H^2 + 3D''H^3 - D''H^4 \\
&= D''H \left(4 - 6H + 4H^2 - H^3\right) \qquad\qquad (E.5)
\end{aligned}
$$

Therefore the third-order transfer function is given by:

$$
\begin{aligned}
H_{3rd}\left(\omega\right) &= \frac{E''(\omega)}{D''(\omega)} \\
&= H\left(\omega\right) \left[4 - 6H\left(\omega\right) + 4H\left(\omega\right)^2 - H\left(\omega\right)^3\right] \qquad (E.6)
\end{aligned}
$$

# E.4    K th-Order Sidelobe Reduction

It has been brought to the candidate's attention by George Tattersfield (UCT) that the overall transfer function of the "$k$ th-order" sidelobe reduction procedure is given by

$$
H_{kth}\left(\omega\right) = H(\omega) \sum_{n=0}^{k} \left[(-1)^{n\ k+1} c_{n+1} \, H(\omega)^n\right] \qquad (E.7)
$$

where

$$
{}^{a}c_{b} = \frac{a!}{(a - b)!\, b!} \qquad (E.8)
$$

# Bibliography

Abend, K. and McCorkle, J. (1995). Radio and TV Interference Extraction for Ultra-Wideband Radar, *Algorithms for Synthetic Aperture Radar Imagery II (D. A. Giglio, ed.), SPIE*, Vol. 2487, Orlando, FL, pp. 119–129.

Axelsson, S. R. J. (1995). Frequency and Azimuthal Variations of Radar Cross Section and their Influence upon Low-Frequency SAR Imaging, *IEEE Transactions on Geoscience and Remote Sensing* **33**(5): 1258–1265.

Bamler, R. (1992). A Comparison of Range-Doppler and Wavenumber Domain SAR Focusing Algorithms, *IEEE Transactions on Geoscience and Remote Sensing* **30**(4): 706–713.

Berlin, G. L., Tarabzouni, M. A., Al-Naser, A. H., Sheikho, K. M. and Larson, R. W. (1986). SIR-B Subsurface Imaging of a Sand-Buried Landscape: Al Labbah Plateau, Saudi Arabia, *IEEE Transactions on Geoscience and Remote Sensing* **24**(4): 595–602.

Braunstein, M., Ralston, J. and Sparrow, D. (1994). Signal Processing Approaches to Radio Frequency Interference (RFI) Suppression, *Algorithms for Synthetic Aperture Radar Imagery (D. A. Giglio, ed.), SPIE*, Vol. 2230, Orlando, FL, pp. 190–208.

Buckreuss, S. (1997). Development of an Interference Filter for P-Band SAR Data, *Third International Airborne Remote Sensing Conference and Exhibition*, Vol. II, Copenhagen, Denmark, pp. 116–121.

Buckreuss, S. (1998). Filtering Interferences from P-Band SAR Data, *Proc. European Conference on Synthetic Aperture Radar, EUSAR'98*, VDE-Verlag GMBH, Berlin and Offenbach, Friedrichshafen, Germany, pp. 279–282.

Cafforio, C., Prati, C. and Rocca, E. (1991). SAR Data Focusing Using Seismic Migration Techniques, *IEEE Transactions on Aerospace and Electronic Systems* **27**(2): 194–207.

Carrara, W. G., Goodman, R. S. and Majewski, R. M. (1995a). *Spotlight Synthetic Aperture Radar Signal Processing Algorithms*, Artech House, Norwood, MA.

Carrara, W., Tummala, S. and Goodman, R. (1995b). Motion Compensation Algorithm for Widebeam Stripmap SAR, *Algorithms for Synthetic Aperture Radar Imagery II (D. A. Giglio, ed.), SPIE*, Vol. 2487, Orlando, FL, pp. 13–23.

Cazzaniga, G. and Guarnieri, A. M. (1996). Removing RF Interferences from P-Band Airplane SAR Data, *Proc. IEEE Geosci. Remote Sensing Symp., IGARSS'96*, Vol. 3, Lincoln, Nebraska, pp. 1845–1847.

Chen, X. (1988). Adaptive Linear-Phase Complex Filtering Algorithms, *IEE Proceedings-F*, Vol. 135, pp. 481–486.

Clarke, R. H. and Brown, J. (1980). *Diffraction Theory and Antennas*, Ellis Horwood Limited, Chichester.

Crespo, J. C. (1996). The Extended Chirp Scaling Processor for the Experimental SAR System of DLR, E-SAR, *Proc. European Conference on Synthetic Aperture Radar, EUSAR'96*, VDE-Verlag GMBH, Berlin and Offenbach, Königswinter, Germany, pp. 353–356.

Cumming, I., Wong, F. and Raney, K. (1992). A SAR Processing Algorithm with No Interpolation, *Proc. IEEE Geosci. Remote Sensing Symp., IGARSS'92*, Clear Lake, TX, pp. 376–379.

Curlander, J. C. and McDonough, R. N. (1991). *Synthetic Aperture Radar Systems and Signal Processing*, John Wiley and Sons, New York.

Currie, N. C. and Brown, C. E. (1987). *Principles and Applications of Millimeter-Wave Radar*, Artech House, Norwood, MA.

Davidson, G. W., Wong, F. and Cumming, I. (1996). The Effect of Pulse Phase Errors on the Chirp Scaling SAR Processing Algorithm, *IEEE Transactions on Geoscience and Remote Sensing* **34**(2): 471–478.

146

DPT (1996). Project SABRE (South African Band Re-planning Exercise) - Band Plan for the Frequencies 20 MHz to 3 GHz, *Technical report*, Department of Posts and Telecommunications.

Drinkwater, M. R., Kwok, R. and Rignot, E. (1990). Synthetic Aperture Radar Polarimetry of Sea Ice, *Proc. IEEE Geosci. Remote Sensing Symp., IGARSS'90*, Washington D.C., USA, pp. 1525–1528.

Elachi, C. (1988). *Spaceborne Radar Remote Sensing: Applications and Techniques*, IEEE Press, New York.

Elachi, C., Roth, L. E. and Schaber, G. G. (1984). Spaceborne Radar Subsurface Imaging in Hyperarid Regions, *IEEE Transactions on Geoscience and Remote Sensing* **22**(4): 383–387.

Ferrell, B. H. (1995). Interference Suppression in UHF Synthetic-Aperture Radar, *Algorithms for Synthetic Aperture Radar Imagery II (D. A. Giglio, ed.), SPIE*, Vol. 2487, Orlando, FL, pp. 96–106.

Fitch, J. P. (1988). *Synthetic Aperture Radar*, Springer-Verlag, New York.

Franceschetti, G. and Schirinzi, G. (1990). A SAR Processor Based on Two-Dimensional FFT Codes, *IEEE Transactions on Aerospace and Electronic Systems* **26**(2): 356–365.

Gill, G. S. (1995). Step Frequency Waveform Design and Processing for Detection of Moving Targets in Clutter, *Proceedings of the IEEE 1995 International Radar Conference, RADAR'95*, Alexandria, Virginia, pp. 573–578.

Glover, J. R. Jr. (1977). Adaptive Noise Cancelling Applied to Sinusoidal Interferences, *IEEE Transactions on Acoustics, Speech, and Signal Processing* **ASSP-25**(6): 484–491.

Golden, A. Jr., Werness, S. A., Stuff, M., DeGraaf, S. and Sullivan, R. (1995). Radio Frequency Interference Removal in a VHF/UHF Deramp SAR, *Algorithms for Synthetic Aperture Radar Imagery II (D. A. Giglio, ed.), SPIE*, Vol. 2487, Orlando, FL, pp. 84–95.

Goriachkin, O. V. and Klowsky, D. D. (1997). New Method for Wideband Low Frequency SAR Data Processing, *Third International Airborne Remote Sensing Conference and Exhibition*, Vol. II, Copenhagen, Denmark, pp. 147–154.

147

Goris, M., Joseph, A., Hampson, G. and Smits, F. (1999). Adaptive Beamforming System for Radio-Frequency Interference Rejection, *IEE Proceedings-Radar, Sonar Navig.* **146**(2): 73–77.

Griffiths, L. J. (1975). Rapid Measurement of Digital Instantaneous Frequency, *IEEE Transactions on Acoustics, Speech, and Signal Processing* **ASSP-23**(2): 207–222.

Gustavsson, A., Flood, B., Frölind, P.-O., Hellsten, H., Jonsson, T., Larsson, B., Stenström, G. and Ulander, L. M. H. (1998a). Design and Verification of a New Airborne 20–90 MHz SAR Sensor, *Proc. European Conference on Synthetic Aperture Radar, EUSAR'98*, VDE-Verlag GMBH, Berlin and Offenbach, Friedrichshafen, Germany, pp. 21–25.

Gustavsson, A., Frölind, P.-O., Hellsten, H., Jonsson, T., Larsson, B. and Stenström, G. (1993). The Airborne VHF SAR System CARABAS, *Proc. IEEE Geosci. Remote Sensing Symp., IGARSS'93*, Vol. 2, Tokyo, Japan, pp. 558–562.

Gustavsson, A., Ulander, L. M. H., Flood, B., Frölind, P.-O., Hellsten, H., Jonsson, T., Larsson, B. and Stenström, G. (1998b). Development and Operation of an Airborne VHF SAR System - Lessons Learned, *Proc. IEEE Geosci. Remote Sensing Symp., IGARSS'98*.

Harris, F. J. (1978). On the Use of Windows for Harmonic Analysis with the Discrete Fourier Transform, *Proceedings of the IEEE*, Vol. 66, pp. 51–83.

Haykin, S. S. (1991). *Adaptive Filter Theory*, 2nd edn, Prentice-Hall, Englewood Cliffs, NJ.

Horrell, J. M. (1999). *Range-Doppler Synthetic Aperture Radar Processing at VHF Frequencies*, PhD thesis, University of Cape Town.

Hovanessian, S. A. (1984). *Radar System Design and Analysis*, Artech House, Norwood, MA.

Hovland, H. A., Johannessen, J. A. and Digranes, G. (1994). Slick Detection in SAR Images, *Proc. IEEE Geosci. Remote Sensing Symp., IGARSS'94*, Pasadena, USA, pp. 2038–2040.

Huang, Y., Ma, Z. and Mao, S. (1996). Stepped-frequency SAR System Design and Signal Processing, *Proc. European Conference on Synthetic Aperture Radar, EUSAR'96*, VDE-Verlag GMBH, Berlin and Offenbach, Königswinter, Germany, pp. 565–568.

Hughes, W., Gault, K. and Princz, G. J. (1996). A Comparison of the Range-Doppler and Chirp Scaling Algorithms with reference to RADARSAT, *Proc. IEEE Geosci. Remote Sensing Symp., IGARSS'96*, Vol. 2, Lincoln, Nebraska, pp. 1221–1223.

Inggs, M. R. (1996). The SASAR VHF Sensor, *Proc. European Conference on Synthetic Aperture Radar, EUSAR'96*, VDE-Verlag GMBH, Berlin and Offenbach, Königswinter, Germany, pp. 317–320.

Inggs, M. R. and Lord, R. T. (1996). SRP Phase VI Status Report, *Technical report*, University of Cape Town, Radar Remote Sensing Group, Cape Town.

Inggs, M. R., Hurwitz, J. and Langman, A. (1993). Synthetic Range Profile Measurements of Aircraft, *IEEE Proceedings of the 1993 South African Communications and Signal Processing Symposium, COMSIG'93*, pp. 204–209.

Inggs, M. R., Knight, A. and Smit, P. (1992a). Synthetic Range Profile Measurements with a Pulse Compression Radar, *IEEE Proceedings of the 1992 South African Communications and Signal Processing Symposium, COMSIG'92*, Cape Town, South Africa, pp. 7–10.

Inggs, M. R., van Zyl, M. W. and Knight, A. (1992b). A Simulation of Synthetic Range Profile Radar, *IEEE Proceedings of the 1992 South African Communications and Signal Processing Symposium, COMSIG'92*, Cape Town, South Africa, pp. 1–6.

Kingsley, S. and Quegan, S. (1999). *Understanding Radar Systems*, SciTech Publishing, Mendham.

Kirk, J. C. (1975). A Discussion of Digital Processing in Synthetic Aperture Radar, *IEEE Transactions on Aerospace and Electronic Systems* **11**(3): 326–337.

Koutsoudis, T. and Lovas, L. (1995). RF Interference Suppression in Ultra Wideband Radar Receivers, *Algorithms for Synthetic Aperture Radar Imagery II (D. A. Giglio, ed.), SPIE*, Vol. 2487, Orlando, FL, pp. 107–118.

Larsson, B., Frölind, P.-O., Gustavsson, A., Hellsten, H., Jonsson, T., Stenström, G. and Ulander, L. M. H. (1997). Some Results from the New CARABAS II VHF SAR System, *Third International Airborne Remote Sensing Conference and Exhibition*, Vol. I, Copenhagen, Denmark, pp. 25–32.

Le, C. T. C., Hensley, S. and Chapin, E. (1997). Adaptive Filtering of RFI in Wideband SAR Signals, *7th Annual JPL AirSAR Workshop*, Pasadena, California.

Lengenfelder, R. (1998a). NCTR Phase VIII: Aircraft Data Capture and Analysis Report, *Technical report*, University of Cape Town, Radar Remote Sensing Group, Cape Town.

Lengenfelder, R. (1998b). The Design and Implementation of a Radar Simulator, *Technical report*, MSc thesis, University of Cape Town, Faculty of Engineering, Cape Town.

Li, J. and Stoica, P. (1995). Adaptive Filtering Approach to Spectral Estimation and SAR Imaging, *Algorithms for Synthetic Aperture Radar Imagery II (D. A. Giglio, ed.), SPIE*, Vol. 2487, Orlando, FL, pp. 153–164.

Lord, R. T. and Inggs, M. R. (1996). High Resolution VHF SAR Processing Using Synthetic Range Profiling, *Proc. IEEE Geosci. Remote Sensing Symp., IGARSS'96*, Vol. 1, Lincoln, Nebraska, pp. 454–456.

Lord, R. T. and Inggs, M. R. (1997a). High Range Resolution Radar Using Narrowband Linear Chirps Offset in Frequency, *IEEE Proc. of the South African Symp. on Communications and Signal Processing, COMSIG'97*, Grahamstown, South Africa, pp. 9–12.

Lord, R. T. and Inggs, M. R. (1997b). High Resolution SAR Processing Using Stepped-Frequencies, *Proc. IEEE Geosci. Remote Sensing Symp., IGARSS'97*, Vol. 1, Singapore, pp. 490–492.

Lord, R. T. and Inggs, M. R. (1998). Approaches to RF Interference Suppression for VHF/UHF Synthetic Aperture Radar, *IEEE Proc. of the South African Symp. on Communications and Signal Processing, COMSIG'98*, Cape Town, South Africa, pp. 95–100.

Lord, R. T. and Inggs, M. R. (1999a). Efficient RFI Suppression in SAR Using a LMS Adaptive Filter with Sidelobe Suppression Integrated with

the Range-Doppler Algorithm, *Proc. IEEE Geosci. Remote Sensing Symp., IGARSS'99*, Vol. 1, Hamburg, Germany.

Lord, R. T. and Inggs, M. R. (1999b). Efficient RFI Suppression in SAR Using LMS Adaptive Filter Integrated with Range/Doppler Algorithm, *Electronics Letters* **35**(8): 629–630.

Lord, R. T. and Inggs, M. R. (2000). Measurements and Characteristics of RFI for a Low-Bandwidth VHF SAR System, *Proc. European Conference on Synthetic Aperture Radar, EUSAR 2000*, VDE Verlag, Munich, Germany, pp. 845–848.

Lynne, G. J. and Taylor, G. R. (1986). Geological Assessment of SIR-B Imagery of the Amadeus Basin, N.T., Australia, *IEEE Transactions on Geoscience and Remote Sensing* **24**(4): 575–581.

Madhukar, C. and Hounam, D. (1998). Feasibility of a Spaceborne P-Band SAR for Land Surface Imaging, *Proc. European Conference on Synthetic Aperture Radar, EUSAR'98*, VDE-Verlag GMBH, Berlin and Offenbach, Friedrichshafen, Germany, pp. 395–398.

Marple, S. L. Jr. (1987). *Digital Spectral Analysis*, Prentice-Hall, Englewood Cliffs, NJ.

Miller, T., McCorkle, J. and Potter, L. (1995). Near-Least-Squares Radio Frequency Interference Suppression, *Algorithms for Synthetic Aperture Radar Imagery II (D. A. Giglio, ed.), SPIE*, Vol. 2487, Orlando, FL, pp. 72–83.

Milstein, L. B. (1988). Interference Rejection Techniques in Spread Spectrum Communications, *Proceedings of the IEEE*, Vol. 76, pp. 657–671.

Mittermayer, J., Scheiber, R. and Moreira, A. (1996). The Extended Chirp Scaling Algorithm for ScanSAR Data Processing, *Proc. European Conference on Synthetic Aperture Radar, EUSAR'96*, VDE-Verlag GMBH, Berlin and Offenbach, Königswinter, Germany, pp. 517–520.

Mobley, S. and Maier, M. (1996). Synthetic Aperture Radar-Systems Processing with a Non-Uniform Pulse Repetition Interval, *Proc. European Conference on Synthetic Aperture Radar, EUSAR'96*, VDE-Verlag GMBH, Berlin and Offenbach, Königswinter, Germany, pp. 407–410.

Moreira, A., Mittermayer, J. and Scheiber, R. (1996). Extended Chirp Scaling Algorithm for Air- and Spaceborne SAR Data Processing in Stripmap and ScanSAR Imaging Modes, *IEEE Transactions on Geoscience and Remote Sensing* **34**(5): 1123–1136.

Moreira, A., Mittermayer, J. and Scheiber, R. (1998). Processing of SAR and ScanSAR Imaging Modes using the Extended Chirp Scaling Algorithm, *Proc. European Conference on Synthetic Aperture Radar, EUSAR'98*, VDE-Verlag GMBH, Berlin and Offenbach, Friedrichshafen, Germany, pp. 557–560.

Munson, D. C. and Visentin, R. L. (1989). A Signal Processing View of Strip-Mapping Synthetic Aperture Radar, *IEEE Transactions on Acoustics, Speech, and Signal Processing* **ASSP-37**(12): 2131–2147.

Oliver, C. and Quegan, S. (1998). *Understanding Synthetic Aperture Radar Images*, Artech House, Boston.

Oppenheim, A. V. (1978). *Applications of Digital Signal Processing*, Prentice-Hall, Englewood Cliffs, NJ.

Potsis, A., Reigber, A., Sutor, T. and Papathanassiou, K. P. (1999). A Phase Preserving Method for RF Interference Suppression in P-Band Synthetic Aperture Radar Interferometric Data, *Proc. IEEE Geosci. Remote Sensing Symp., IGARSS'99*, Vol. 5, Hamburg, Germany.

Prati, C. and Rocca, F. (1992). Range Resolution Enhancement with Multiple SAR Surveys Combination, *Proc. IEEE Geosci. Remote Sensing Symp., IGARSS'92*, Houston, TX, pp. 1576–1578.

Ralston, J. M. (1998). Ultra-Wide SAR System Analysis, *Proc. European Conference on Synthetic Aperture Radar, EUSAR'98*, VDE-Verlag GMBH, Berlin and Offenbach, Friedrichshafen, Germany, pp. 485–488.

Ralston, J. M., Heagy, J. F. and Sullivan, R. J. (1998). Environmental Noise Effects on VHF/UHF UWB SAR, *Proc. European Conference on Synthetic Aperture Radar, EUSAR'98*, VDE-Verlag GMBH, Berlin and Offenbach, Friedrichshafen, Germany, pp. 141–144.

Raney, R. K. (1998). *Principles and Applications of Imaging Radar - Manual of Remote Sensing*, Vol. 2, 3rd edn, John Wiley and Sons, New York.

Raney, R. K., Runge, H., Bamler, R., Cumming, I. G. and Wong, F. H. (1994). Precision SAR Processing Using Chirp Scaling, *IEEE Transactions on Geoscience and Remote Sensing* **32**(4): 786–799.

Riegler, R. L. and Compton, R. T. Jr. (1973). An Adaptive Array for Interference Rejection, *Proceedings of the IEEE*, Vol. 61, pp. 748–758.

Rihaczek, A. W. (1996). *Principles of High-Resolution Radar*, Artech House, Norwood, MA.

Robinson, A. D. and Inggs, M. R. (1994). Correlation Filters Applied to Synthetic Range Profiles of Aircraft Targets, *IEEE Proc. of the South African Symp. on Communications and Signal Processing, COMSIG'94*.

Runge, H. and Bamler, R. (1992). A Novel High Precision SAR Focussing Algorithm Based on Chirp Scaling, *Proc. IEEE Geosci. Remote Sensing Symp., IGARSS'92*, Clear Lake, TX, pp. 372–375.

Sack, M., Ito, M. R. and Cumming, I. G. (1985). Application of Efficient Linear FM Matched Filtering Algorithms to Synthetic Aperture Radar Processing, *IEE Proceedings*, Vol. 132, pp. 45–57.

Schaber, G. G., McCauley, J. F., Breed, C. S. and Olhoeft, G. R. (1986). Shuttle Imaging Radar: Physical Controls on Signal Penetration and Subsurface Scattering in the Eastern Sahara, *IEEE Transactions on Geoscience and Remote Sensing* **24**(4): 603–623.

Schaber, G. G., Olhoeft, G. R. and McCauley, J. F. (1990). The "Radar Rivers" of the Eastern Sahara: Signal Penetration and Subsurface Scattering Observed by the Shuttle Imaging Radar, *Proceedings of 3rd International Conference on GPR*, p. 61.

Scheer, J. A. and Kurtz, J. L. (1993). *Coherent Radar Performance Estimation*, Artech House, Norwood, MA.

Seger, O., Herberthson, M. and Hellsten, H. (1998). Real Time SAR Processing of Low Frequency Ultra Wide Band Radar Data, *Proc. European Conference on Synthetic Aperture Radar, EUSAR'98*, VDE-Verlag GMBH, Berlin and Offenbach, Friedrichshafen, Germany, pp. 489–492.

Shteinshleiger, V., Dzenkevich, A., Misezhnikov, G. and Mel'nikov, L. (1996). On the Possibility of Designing a High-Resolution Space-Borne VHF-Band SAR for Remote Sensing of the Earth, *Proc. European Conference on Synthetic Aperture Radar, EUSAR'96*, VDE-Verlag GMBH, Berlin and Offenbach, Königswinter, Germany, pp. 321–324.

Skolnik, M. I. (1990). *Radar Handbook*, 2nd edn, McGraw-Hill, New York.

Stimson, G. W. (1983). *Introduction to Airborne Radar*, Hughes Aircraft Company, El Segundo, California.

Suess, M., Völker, M., Wilson, J. J. W. and Buck, C. H. (1998). Superresolution: Range Resolution Improvement by Coherent Combination of Repeat Pass SAR Images, *Proc. European Conference on Synthetic Aperture Radar, EUSAR'98*, VDE-Verlag GMBH, Berlin and Offenbach, Friedrichshafen, Germany, pp. 565–569.

Taylor, J. D. (ed.) (1995). *Introduction to Ultra-Wideband Radar Systems*, CRC Press, Boca Raton, Florida.

Trizna, D. and Sletten, M. (1997). NUWSAR - NRL Ultra Wideband Synthetic Aperture Radar an Experimental Tool for Remote Sensing Studies, *Third International Airborne Remote Sensing Conference and Exhibition*, Vol. II, Copenhagen, Denmark, pp. 68–73.

Ulander, L. M. H. (1998). Performance of Stepped-Frequency Waveform for Ultra-Wideband VHF SAR, *Proc. European Conference on Synthetic Aperture Radar, EUSAR'98*, VDE-Verlag GMBH, Berlin and Offenbach, Friedrichshafen, Germany, pp. 323–326.

Ulander, L. M. H. and Frölind, P.-O. (1999). Precision Processing of CARABAS HF/VHF-band SAR Data, *Proc. IEEE Geosci. Remote Sensing Symp., IGARSS'99*, Vol. 1, Hamburg, Germany.

Ulander, L. M. H. and Hellsten, H. (1997). System Analysis of Ultra-Wideband VHF SAR, *Proceedings of the IEEE 1997 International Radar Conference, RADAR'97*, Edinburgh, UK, pp. 104–108.

Vant, M. R. (1989). Synthetic Aperture Radar Signal Processing, *Proceedings of the 1989 International Conference on Radar*.

Wahl, T. and Skoelv, A. (1994). ERS-1 SAR Imaging of Ocean Features in the Vestfjorden Area, *Proc. IEEE Geosci. Remote Sensing Symp., IGARSS'94*, Pasadena, USA, pp. 2035–2037.

Walter, F., Fransson, J. E. S. and Frölind, P.-O. (1999). Fully Automatic Geocoding of CARABAS-II VHF SAR Images, *Proc. IEEE Geosci. Remote Sensing Symp., IGARSS'99*, Vol. 1, Hamburg, Germany.

Wehner, D. R. (1995). *High-Resolution Radar*, 2nd edn, Artech House, Norwood, MA.

Widrow, B. and Stearns, S. D. (1985). *Adaptive Signal Processing*, Prentice-Hall, Englewood Cliffs, NJ.

Widrow, B., Glover, J. R. Jr., McCool, J. M., Kaunitz, J., Williams, C. S., Hearn, R. H., Zeidler, J. R., Dong, E. Jr. and Goodlin, R. C. (1975a). Adaptive Noise Cancelling: Principles and Applications, *Proceedings of the IEEE*, Vol. 63, pp. 1692–1716.

Widrow, B., McCool, J. and Ball, M. (1975b). The Complex LMS Algorithm, *Proceedings Letters of the IEEE*, pp. 719–720.

Wilkinson, A. J. (1996). Notes on Synthetic Range Profiling, *Technical report*, University of Cape Town, Department of Electrical Engineering, Cape Town, April 1996.

Wilkinson, A. J., Lord, R. T. and Inggs, M. R. (1998). Stepped-Frequency Processing by Reconstruction of Target Reflectivity Spectrum, *IEEE Proc. of the South African Symp. on Communications and Signal Processing, COMSIG'98*, Cape Town, South Africa, pp. 101–104.

Zeidler, J. R., Satorius, E. H., Chabries, D. M. and Wexler, H. T. (1978). Adaptive Enhancement of Multiple Sinusoids in Uncorrelated Noise, *IEEE Transactions on Acoustics, Speech, and Signal Processing* **ASSP-26**(3): 240–254.